The Dynamics and Stability of Flows Around Rolling Bluff Bodies

by

Bronwyn E. Stewart

B.Sc/B.Eng(Hons)

A Thesis submitted to Monash University
for the degree of
Doctor of Philosophy (Cotutelle)

MONASH UNIVERSITY
Department of Mechanical Engineering
and
UNIVERSITÉ DE PROVENCE AIX-MARSEILLE I
Instut de Recherche sur les Phénomènes Hors Équilibre (IRPHE)

August 2008

Stabilité et dynamique d'écoulement autour de corps roulant non profilé

par

Bronwyn E. STEWART

Thèse présentée pour obtenir le grade de
Docteur de l'Université de Provence

Discipline: Mécanique et Physique des Fluides
Ecole Doctorale: Physique, Modélisation et Sciences pour l'Ingénieur

---

Université de Provence Aix-Marseille I
Instut de Recherche sur les Phénomènes Hors Équilibre (IRPHE)

et

Monash University, Melbourne, Australie
Department of Mechanical Engineering

Directeurs de thése:
M. Thomas LEWEKE
M. Mark C. THOMPSON
M. Kerry HOURIGAN

août 2008

Contents

Introduction **1**

Problem overview 2

Scope and structure of this thesis 3

1 A Review of the Literature **5**

1.1 Flow past a cylinder 5

1.1.1 Flow past a cylinder in a free stream 5

Two-dimensional steady flow 5

Two-dimensional unsteady flow 7

Three-dimensional flow 8

1.1.2 Flow around a rotating cylinder 12

Magnus effect and potential flow 12

Steady flow 13

Unsteady flow behind the rotating cylinder 14

Suppression of unsteady flow 15

Lift and drag forces due to rotation 16

Three-dimensional effects 17

1.1.3 Flow past a cylinder near a wall 17

Steady flow and the suppression of vortex shedding . . 18

Unsteady flow 20

Lift and drag forces induced by the wall 22

1.2 Flow past a sphere 23

1.2.1 Flow past a sphere in a freestream 23

Axisymmetric steady flow 23

Non-axisymmetric steady flow 24

Unsteady flow 25

1.2.2 Flow past a rotating sphere 29

Effect of rotation on the flow 29

Rotation effects on the lift and drag forces 30

1.2.3 Flow past a sphere near a wall 31

Wall-induced motion 32

Effect on the flow structures 34
1.3 Lubrication effects and cavitation 35
1.4 Review summary and points of interest for the present study 36

2 Numerical method and resolution studies **39**
2.1 Numerical simulations 39
2.1.1 Governing equations 39
2.1.2 Numerical scheme 40
Temporal Discretisation 40
2.1.3 Linear stability analysis 43
2.1.4 Resolution studies for the cylinder 46
Boundary resolution 47
Mesh resolution 49
Gap resolution 50
2.1.5 Resolution studies for the sphere 53
Boundary resolution 55
Mesh resolution 56
Gap resolution 57
2.2 Chapter summary 58

3 Experimental method **59**
3.1 Experimental setup 59
3.1.1 Calibration and convergence tests 67
3.2 Chapter summary 69

4 Two-dimensional flow around the cylinder **71**
4.1 Flow in the contact region 71
4.2 Steady flow 74
4.2.1 Flow structure 74
4.2.2 Recirculation lengths 78
4.2.3 Lift and drag trends 80
4.3 Unsteady flow 86
4.3.1 Critical *Re* of transition 86
4.3.2 Flow structures 87
4.3.3 St-Re relationship 89
4.3.4 Lift and drag trends 90
4.4 Chapter summary 91

5 Three-dimensional flow around the cylinder **93**
5.1 Linear stability analysis 93
5.1.1 Critical *Re* and growth of the mode 93

5.1.2 Neutral stability curves 96
5.1.3 Perturbation modes 96
5.2 Three-dimensional simulations 102
5.3 The transition mechanism 104
5.4 Experimental results for the cylinder 106
5.5 Chapter summary 110

6 The rolling sphere 113

6.1 Flow regimes and transitions 114
6.2 Steady flow 115
6.3 Unsteady wake modes 120
6.3.1 The symmetric mode 122
6.3.2 The antisymmetric mode 125
6.3.3 The transition between modes 131
6.3.4 The wake frequency 133
6.4 Chapter summary 140

7 Conclusions 143

7.1 Further work 146

Abstract

A numerical and experimental study of the flow around rolling and sliding bodies is presented. The body geometry is fixed as being either spherical or cylindrical and the Reynolds number of the flow is restricted to $Re \leq 500$. This range is sufficient to capture the primary two- and three-dimensional transitions in the flow. The primary aim of this study is to understand the effects of body rotation and a nearby wall on the flow transitions when these effects are acting in tandem. In the case of the cylinder moving along the wall, both two- and three-dimensional flows are investigated and the results of a linear stability analysis are reported. The flow around a rolling and sliding sphere is investigated using both experiments and three-dimensional simulations.

The parameter space under consideration is defined in terms of the Reynolds number, based on the body diameter, and the rotation rate of the body, α. For a body moving along a wall in a quiescent fluid, the rotation rate corresponds to the ratio of tangential velocity on the surface of the body to the translational velocity. Five discrete values of the rotation rate have been selected, $\alpha = 1$, 0.5, 0, -0.5 and -1. These range from 'normal' rolling, where there is no slip between the body and the wall, to reversed rolling, where the body rotates in the opposite sense. This range is selected to correspond with the range of rotation rates observed in experiments of freely rolling bodies with and without lubrication effects.

A spectral-element method is applied to compute the flow fields in both two and three dimensions. Studies show that the reported flow variables are converged to within 1% with respect to the domain size, spatial and temporal resolution. In order to model the body moving along a wall, the numerical code requires that a small distance is imposed between the body and the wall. This distance is set equal to 0.5% of the diameter and the sensitivity of the flow to small variations in this parameter is reported.

Experiments are carried out on a closed circuit water channel equipped with a moving floor and boundary layer suction. The cylinder or sphere is mounted across the stream and the flow is then analysed in the frame of reference attached to the body. Laser Doppler Anemometry is used to calibrate the equipment and investigate the velocity profiles in the empty test section with both the moving floor and boundary layer suction in operation. Dye visualisation is used to capture the structures in the wake of the cylinder and sphere.

Two dimensional simulations and experiments are undertaken of the unsteady flow structures that form around the rolling cylinder. This wake displays vortex shedding and the pairing of opposite sign vorticity. Reversed rolling ($\alpha = -1$) is the most stable configuration of those studied, with the onset of unsteady flow delayed until $Re \approx 425$ in the numerical simulations. The drag and lift forces on the cylinder are presented, as is the Strouhal number associated with the unsteady flows.

Linear stability analysis of the cylinder flow predicts the wake to become three dimensional prior to the onset of unsteady flow. The dominant instability is a steady mode, the critical Reynolds number of which varies from 35 to 180, depending on the rotation rate. The form of this perturbation mode is investigated further with the use of three-dimensional simulations.

Analysis of the flow around the rolling sphere indicates the presence of steady and unsteady modes, the structure of which varies with rotation rate. At low Reynolds numbers, a steady mode occurs for all values of α studied. As Re increases, this mode undergoes a transition to one of two unsteady modes. A third unsteady mode is detected in numerical simulations and found to be unstable to small perturbations in the flow.

Of the two unsteady modes observed in experiments, one is a new, unreported wake state that occurs when the sphere is undergoing reversed rolling. This unsteady wake has an antisymmetric structure, comprising two streamwise vortices that display a helical motion. Both experiments and numerical simulations are used to observe and analyse this wake mode. When the sphere is undergoing forward rolling, the wake is similar to that observed behind a sphere in an unbounded flow and the shedding of hairpin vortices takes place. Unlike the cylinder, the sliding sphere with $\alpha = 0$ provides the most stable solution and the onset of unsteady flow is delayed until $Re > 300$.

Statement of Originality

I, Bronwyn Stewart, declare that this thesis is my own work and contains no material that has been accepted for the award of a degree or diploma in this or any other university. To the best of my knowledge and belief, this thesis contains no material previously published or written by another person except where due reference is made in the text of this thesis.

August 2008

Acknowledgments

I would like to firstly thank my three supervisors, Prof. Mark Thompson, Prof. Kerry Hourigan and Dr. Thomas Leweke. The guidance and direction they offered throughout this project was invaluable. Furthermore, their support during my time studying in France under the cotutelle scheme is gratefully acknowledged. The French language support that was arranged prior to my departure, and the warm welcome offered by Dr. Thomas Leweke upon my arrival in France, aided the transition enormously.

Financial support for this research has been gratefully received through an Australian Postgraduate Award, and a Mobility Grant from the French Ministry of Higher Education and Research. Travel grants have also been provided by the French Embassy in Australia and the Monash Research Graduate School. Other resources have been provided by the Department of Mechanical Engineering at Monash, the Australian Partnership for Advanced Computing, who have provided computing time on their high performance machines, and from IRPHE in Marseille, who have developed the experimental equipment necessary to complete this work.

During my candidature there have been several people who have always made themselves available to discuss ideas and offer moral support. For their personal and professional assistance during this time I would like to acknowledge Miss Naomi Brammer, Mr Joe Berry, Mr Owen Gould, Mr Hyeok Lee and Dr. Martin Griffith. A special thank you must also be given Dr. Justin Leontini for the insight he has offered into this research, both in Australia and during his time spent in France.

To my family, I would like to thank my mother, Elaine, and my parents-in-law, Heather and Laurie, for the love and support that they have offered throughout this time. Finally, to my husband Terence, you have encouraged and strengthened me during the ups and downs of the last few years. Even when we were apart your support never wavered. Thank you.

Publications

Stewart, B. Leweke, T., Thompson, M. & Hourigan K. 2008 Wake Structures Behind a Rolling Sphere on a Wall. *In Proceedings of the 22nd International Congress of Theoretical and Applied Mechanics*, Adelaide, Australia, August 2008. (Accepted)

Stewart, B. E., Leweke, T., Hourigan, K. & Thompson M. C. 2008 Wake Formation Behind a Rolling Sphere. *Physics of Fluids* **20**, 071704-1–4.

Stewart, B., Leweke, T., Thompson M. & Hourigan, K. 2007 The Wake Behind a Rolling Sphere. *Bulletin of the American Physical Society:60th Annual Meeting of the Division of Fluid Dynamics*, 52(12):GR4, American Physical Society, Salt Lake City, USA, November 2007.

Stewart, B. E., Hourigan K., Thompson, M. C. & Leweke, T. 2007 Flow Control via Imposed Rotation of a Cylinder Moving Along a Wall *In Proceedings of the IUTAM Symposium on Unsteady Separated Flows and Their Control*, Corfu, Greece, June 2007.

Stewart, B. E., Hourigan, K., Thompson M. C. & Leweke, T. 2006 Flow Dynamics and Forces Associated with a Cylinder Rolling Along a Wall. *Physics of Fluids* **18**, 111701-1–4.

Stewart, B., Leontini, J., Hourigan K. & Thompson, M. C. 2005 Vortex Wake and Energy Transitions of an Oscillating Cylinder at Low Reynolds Number Flow. *Journal of the Australian and New Zealand Industrial and Applied Mathematics Society* **46(E)**, C181-195.

Stewart, B., Leontini, J., Hourigan K. & Thompson, M. C. 2005 A numerical survey of wake modes and energy transfers for an oscillating cylinder at Re=200 *In Proceedings of the 4th Symposium on Bluff Body Wakes and Vortex-Induced Vibrations*, Santorini, Greece, June 2005.

Stewart, B., Leontini, J. S., Hourigan K. & Thompson, M. C. 2004 Vortex wake and energy transitions of an oscillating cylinder at low Reynolds number *In Proceedings of the The 14th Australasian Fluid Mechanics Conference*, University of Sydney, Australia, December 2004.

Leontini, J. S., Stewart, B. E., Thompson M. C. & Hourigan, K. 2006 Wake State and Energy Transitions of an Oscillating Cylinder at Low Reynolds Number *Physics of Fluids* **18**, 067101-1–9.

Leontini, J. S., Stewart, B. E., Thompson M. C. & Hourigan, K. 2006 Predicting Vortex-Induced Vibration from Driven Oscillation Results *Applied Mathematical Modelling* **30**, 1096–1102.

Nomenclature

List nomenclature here.

Symbol	**Description**
α	Rotation parameter, $D\omega/2U$
α_c	Rotation rate at which vortex shedding is suppressed
Γ	Circulation
λ	Wavelength
λ_c	Critical wavelength at which the flow becomes three-dimensional
μ	Dynamic viscosity, Floquet multiplier
ν	Kinematic viscosity, μ/ρ
σ	Instability growth rate
τ	Non-dimensional time, tU/D
C_D	Coefficient of drag, $2F_D/(\rho U^2 A)$
$\bar{C_D}$	Mean drag coefficient
C_{Dp}	Pressure component of the drag coefficient
C_{Dv}	Viscous component of the drag coefficient
C_L	Coefficient of lift, $2F_L/(\rho U^2 A)$
$\bar{C_L}$	Mean lift coefficient
C_{Lp}	Pressure component of the lift coefficient
C_{Lv}	Viscous component of the lift coefficient
C_P	Coefficient of pressure
D	Diameter
$E(x)$	Estimate of error present in x
f_s	Frequency of vortex shedding
f_ω	Frequency of body rotation

Continued on the next page.

Continued from previous page.

Symbol	Description
F	Number of Fourier planes
H	Step height
M	Number of macro elements in the mesh
N	Number of nodes per macro element of the mesh
n	Index for current iteration
$\mathbf{n}$	Vector normal to the boundary
P	Scalar pressure field
p	Dynamic pressure, P/ρ
p'	Perturbation dynamic pressure
$R1$	Upper recirculation zone behind the cylinder
$R2$	Lower recirculation zone behind the cylinder
Re	Reynolds Number, UD/ν
$Re1_{cyl}$	Critical Reynolds number of Hopf bifurcation for the cylinder
$Re2_{cyl}$	Critical Reynolds number of mode A transition
$Re2'_{cyl}$	Critical Reynolds number of mode B transition
Re_c	Critical Reynolds number at which the flow becomes three-dimensional
$\hat{r}$	Generic symbol indicating one of $\hat{u}$,$\hat{v}$,$\hat{w}$ or $\hat{p}$
St	Strouhal number, f_sD/U
T	Period
T_K	Temperature in Kelvin
t	Time
Δt	Timestep
U	Free-stream velocity, Cylinder translation speed
$\bar{U}$	Mean velocity measured at a point
U_{RMS}	Root mean square velocity
$\mathbf{u}$	Velocity vector
$\mathbf{u}^*$	Velocity at first sub-step
$\mathbf{u}^{**}$	Velocity at second sub-step
$\mathbf{u}'$	Perturbation velocity

Continued on the next page.

Continued from previous page.

Symbol	Description
$\mathbf{u}_t$	Tangential velocity on the surface of the cylinder/sphere
u	Velocity component in the x-direction
u'	Perturbation velocity in the x-direction as a function of x,y,z and t
$\hat{u}$	Complex perturbation velocity in the x-direction as a function of x,y and t
v	Velocity component in the y-direction
v'	Perturbation velocity in the x-direction as a function of x,y,z and t
$\hat{v}$	Complex perturbation velocity in the x-direction as a function of x,y and t
w	Velocity component in the z-direction
w'	Perturbation velocity in the x-direction as a function of x,y,z and t
$\hat{w}$	Complex perturbation velocity in the x-direction as a function of x,y and t
x	Cartesian streamwise coordinate
x^*	Non-dimensional streamwise distance, x/D, measured from the body centre
$x1, x2$	Position of the upstream and downstream mesh boundaries
y	Cartesian coordinate perpendicular to the wall
$y1$	Position of the transverse mesh boundary
z	Cartesian spanwise coordinate, Azimuthal cylindrical polar coordinate

Introduction

The flow around bluff bodies has been a major area of fluid dynamics research over the past several decades. Many studies have considered the flow past basic geometries such as the cylinder and sphere. A few studies have considered the effect of rotation or nearby walls on the flow but only a very limited number of investigations have considered the result of these two effects acting in tandem.

The combination of body motion and the presence of a solid wall are seen in a range of everyday applications. The translation or rotation of cylinders and spheres near a solid boundary is encountered in the flow inside mixing vessels and many engineering fields consider the transport of particle-laden flows. From sedimenting particles in a slurry mixture, to rolling wheels, and the migration of white blood cells along the vessel wall, a huge range of physical situations may be modeled as the movement of a bluff body along a wall.

The present investigation aims to understand better these types of flows, especially with regards to the steady and unsteady structures that develop in the wake. Particular attention has been given to the two- and three-dimensional transitions that occur in the flow around cylinders and spheres and how these flows are altered by the combined effects of translation and rotation when the body is in near-contact with a wall. From this, it is hoped that a clearer understanding may be gained as to the fundamental mechanisms that govern the flow.

What follows here is a brief overview of the problem under consideration, including a description of the geometry and key parameters that are used to characterise the flow. Also included here is a summary of the techniques used during the investigation and a short outline of the structure of this thesis.

Problem overview

The present study considers the flow around a cylinder or sphere moving along a plane wall through a quiescent fluid. The movement of the body may be rolling or sliding, or a combination of the two, and both positive and negative rotation rates are considered. A basic illustration of the problem under consideration is shown in figure I. In this representation, D is the diameter of the cylinder or sphere and U is its translational velocity. The angular velocity is denoted ω, and G represents a small displacement between the body and the wall.

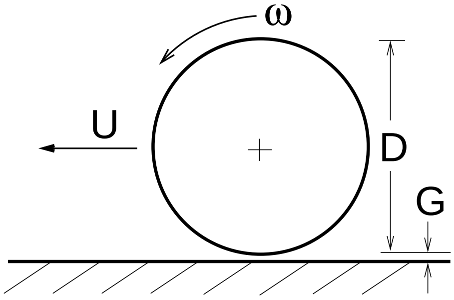

FIGURE I: Simple schematic of the problem under consideration.

Figure I shows the body moving through a still fluid near a stationary wall. In practice this requires the use of very large experimental apparatus and some additional complications to the numerical code. Instead, the problem may be simplified by considering a change of reference frame. For this reason, results presented in this thesis show the centre of the cylinder or sphere as being fixed in space, with the solid wall and a uniform freestream flow moving past the sphere at the same velocity, U. All results are presented with the flow and the solid boundary moving from left to right.

The relative motion of the body and the fluid have allowed this problem to be characterised quite simply by a few dimensionless parameters. One frequently used parameter for classifying bluff body flows is the Reynolds number,

$$Re = \frac{\rho U D}{\mu},$$

where μ is the coefficient of viscosity and ρ is the fluid density. This number represents a ratio of the inertial to viscous effects present in the flow and a range of $20 < Re < 500$ will be considered in this study.

When the cylinder or sphere is moving through a quiescent fluid, as shown in figure I, the body motion can be defined by the ratio of the rotational to translational velocity.

This is given by

$$\alpha = \frac{D\omega}{2U},$$

where positive α has the anticlockwise sense of rotation indicated in figure I. When $\alpha = 1$, the body moves in the intuitive sense of forward rolling. With the reference frame fixed to the centre of the body, this corresponds to the case of the body and the plane wall moving at the same relative velocity, at their nearest points, without slipping. The term 'reversed rolling' will be used to describe the case when $\alpha < 0$, and $\alpha = -1$ corresponds to the case when the nearest points of the body surface and the wall are moving at equal magnitudes but in opposite directions. During this investigation, five discrete values of α are studied, these are 1, 0.5, 0, -0.5 and -1.

Several other dimensionless parameters will be frequently quoted throughout this investigation. Two of these are the gap ratio, defined as G/D, and the Strouhal number, $St = f_s D/U$. The former of these specifies the separation between the body and the wall and the latter is used to characterise unsteady wake flows, where f_s is the shedding or wake frequency. For the numerical part of this thesis, the gap ratio is set equal to 0.005 to approximate the body moving on the wall.

Scope and structure of this thesis

This investigation was carried out using numerical and experimental facilities at two universities. Numerical simulations were run whilst at Monash University in Melbourne using high performance computing clusters located on campus and in Canberra. Time was also spent at Université de Provence in Marseille, where experiments were conducted in a water tunnel that was modified to model this problem and was equipped with a moving floor.

In order to identify the effect of combined wall and body motions on the flow, two- and three-dimensional simulations were used to model the movement of fluid around a cylinder and sphere on a wall. The focus of the experimental setup was to model the flow around the sphere, which was far more computationally expensive than the case of the cylinder as it could not be modeled in two-dimensions. However, a limited number of experiments were carried out with the cylinder in the water channel, to provide qualitative data in support of the numerical predictions.

In chapter 1 of this thesis, a comprehensive overview of the published literature is presented, relating to the flow around cylinders and spheres both in an unbounded flow and with wall effects and body motion. This is followed in chapters 2 and 3 by a detailed description of the numerical and experimental methodologies, respectively. A description of the numerical convergence studies and the experimental calibration techniques are also presented in these chapters.

The results for flow around the cylinder are presented in chapters 4 and 5. Chapter 4 reports the results of the two-dimensional simulations during the steady and unsteady flow regimes. Following this, a linear stability analysis is carried out to predict the three-dimensional transitions in the flow. These results are presented in chapter 5, along with the three-dimensional simulations and a comparison with the experiments.

Results for the flow around a rolling and sliding sphere are presented in chapter 6. The parameter space defined by Re and α was explored using both experiments and three-dimensional simulations. The different wake modes are classified and the dominant flow structures identified using dye visualisation and numerical vorticity contours. These findings are summarised in chapter 7, along with some suggested areas of future research relating to this thesis.

Chapter 1

A Review of the Literature

What follows is a review of the literature to date, relating to the flow around cylinders and spheres. The influence of rotation and nearby walls on the flow has also been discussed with reference to (1) the major transitions in the wake (such as steady to unsteady or two- to three-dimensional) and (2) to the lift and drag forces experienced by the body.

1.1 Flow past a cylinder

1.1.1 Flow past a cylinder in a free stream

The flow past a stationary cylinder, placed transverse to a free-stream has been the subject of research for decades past. This is largely due to the wide-ranging applications of such a geometry in building construction, off-shore engineering, aerodynamics and vortex-induced vibration, to name just a few. The flow around the basic structure is now fairly well understood and this will be summarised in the following sections.

Two-dimensional steady flow

When a cylinder is placed in a flow at low Reynolds numbers, the fluid passes smoothly and symmetrically around the body without separating from the surface. For $Re < 1$, the flow is dominated by viscous effects and behaves in a manner first described by Stokes (1851).

One of the earliest experimental works to consider the attached flow around a cylinder was undertaken by Taneda (1956b), who used flakes of aluminium dust to visualise the streamlines of the flow. The streamlines thus created appear symmetric about the cylinder cross-section and this type of low Re flow, often referred to as 'creeping flow', has the property of being fully reversible as $Re \rightarrow 0$. That is, after the flow has undergone a series of perturbations, it is possible to reverse the process and have the system restored exactly to its initial state.

As the Re of the flow is increased, the fluid initially remains attached to the surface of the cylinder while the symmetry of the flow is lost. This remains true until the fluid separates from the downstream side of the cylinder. This is described by Noack *et al.* (1993) as the process during which the separation point at the rear of the cylinder bifurcates into a vortex pair. This process results in the formation of two closed, symmetric recirculation zones, an example of which is shown in figure 1.1.

The critical value of Re at which the flow separates is difficult to determine exactly. This is particularly true for experimental investigations in which the initial, small-scale structures are difficult to observe. In general, investigations find the onset of separated flow to occur for $5 < Re < 7$ (Taneda 1956b; Dennis & Chang 1970; Tamaki & Keller 1969; Collins & Dennis 1973).

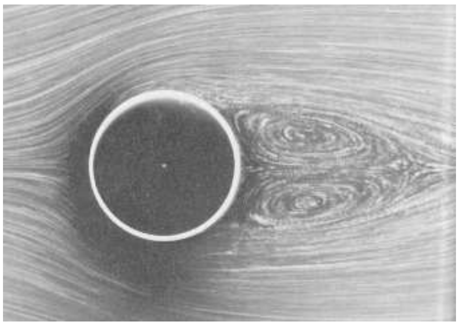

FIGURE 1.1: Aluminium flake visualisation of the streamlines around a cylinder at $Re = 26$, showing steady, separated flow (taken from Van Dyke (1982) with photograph by S. Taneda).

Due to the technological restraints placed on early computational studies, many of those to study the flows in this low Re range did so by solving the steady form of the Navier-Stokes equations (Tamaki & Keller 1969; Thom 1933; Dennis & Chang 1970). Although this method provides no information about the transition to time-dependent flow, the results in the steady-flow range of Re showed good agreement with their experimental counterparts. These results indicate that the downstream length of the recirculation region grows approximately linearly with Re. As these steady recirculation zones grow in length, small oscillations of the flow have been observed in the downstream wake for $30 < Re < 45$ (Taneda 1956b). These oscillations precede the onset of unsteady flow in the near wake, at which point fully formed vortices are shed from the shear layers on either side of the cylinder.

Two-dimensional unsteady flow

A range of studies have found the value for the critical Reynolds number for transition to unsteady flow to lie in the range $45 < Re < 47$ (Jackson 1987; Henderson 1997; Taneda 1956b; Provansal *et al.* 1987; Roshko 1954). For simplicity, in the present study the value of $Re = 46$ will be used for comparison.

The cylinder wake undergoes this transition from steady to two-dimensional, time-varying flow (often termed the 'primary instability') due an area of absolute instability that grows in the near wake (Henderson 1997). This instability causes the shear layers passing over either side of the cylinder to interact in the near wake. Furthermore, it has been shown that this transition is a super-critical Hopf bifurcation that takes place without hysteresis (Jackson 1987; Provansal *et al.* 1987; Noack & Eckelmann 1994).

The vortex shedding behind the cylinder takes the form of the Bénard-von Kármán vortex street (as shown in figure 1.2), named in honour of Henri Bénard and Theodore von Kármán who, individually, were among the first to identify and analyse this phenomenon. The vortex street is composed of a double row of vortices of opposite sign that shed from the rolled up shear layers and have an associated periodicity.

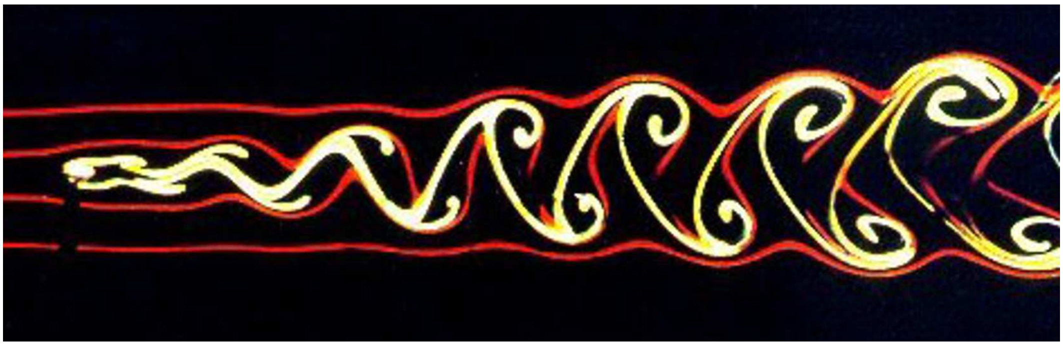

FIGURE 1.2: The Bénard-von Kármán vortex street behind a circular cylinder at $Re = 65$ (taken from Provansal *et al.* (2004)).

One of the more extensive studies of the vortex street behind a cylinder was undertaken by Roshko (1954), who found vortex shedding for $Re > 40$ for experiments in a wind tunnel. The Strouhal number, St, for these and the earlier experiments by Kovasznay (1949) was found to be approximately 0.12 at the onset of vortex shedding. As Re was further increased, the value of St increased, until $Re = 300$, where the values appeared to asymptote to $St = 0.21$. This trend was confirmed in the later experimental works of Williamson (1989) and Hammache & Gharib (1991). The frequency of vortex shedding has also been found to be sensitive to perturbations in the cylinder motion. For cylinders undergoing an oscillation with a frequency close to the natural frequency of the unsteady wake, the shedding is observed to 'lock-on' to the cylinder motion, a phenomenon termed synchronisation (Williamson & Roshko 1988).

During experimental investigations, Williamson (1989) made a study of the 'oblique' modes of vortex shedding in which the vortex shedding commenced at one end, or both ends, of the cylinder and traveled along the span. It was determined that this oblique shedding was primarily due to end effects and that shedding parallel to the cylinder axis could be enforced with the use of angled end-plates. It was noted in the original paper by Roshko (1954) that there exists significant scatter of the experimental St values in the range $150 < Re < 300$. A later study by Williamson (1996a) attributes the scatter present at this range of Re to the presence of discontinuities and oblique shedding in the flow.

Three-dimensional flow

As Reynolds number is increased within the laminar shedding regime, the wake undergoes a transition to three-dimensional flow. One of the earliest studies to identify this phenomenon was that by Williamson (1988b), who found that two successive transitions take place, each leading to the development of a distinct, three-dimensional wake. Each of these wake transitions has an associated discontinuity in the Strouhal-Reynolds number curve and these modes have come to be called mode A and B, after the manner in which Williamson (1988a) first referred to them.

Mode A is the first three-dimensional mode to develop at $Re \approx 190$, with a wavelength of $\lambda \approx 4D$ (Williamson 1996a; Henderson 1997; Barkley *et al.* 2000). In their numerical analyses, Henderson (1997) and Barkley & Henderson (1996) found that the onset of the mode A wake results in a drop in shedding frequency that is caused by a sub-critical bifurcation, indicating the presence of a possible hysteresis. A lower limit of $Re = 180$ is predicted for the hysteresis effects, which is in good agreement with the earlier work of Williamson (1996a), who had observed the hysteresis experimentally for $180 < Re < 194$.

The mode A instability manifests itself in the formation of pairs of counter-rotating streamwise vortices, and the deformation of the spanwise structure is shown in the dye visualisation of figure 1.3(a). This mode is self-inducing and the streamwise vortices in the previous half-cycle act to generate new streamwise vortices at the same span-wise location in the present half-cycle. A detailed description of this is given in Leweke & Williamson (1998b) and Williamson (1996a), with the mode of generation leading to an out-of-phase streamwise pattern. This signifies that from one half-cycle to the next, the orientation of the streamwise vortices at a given span-wise location switches from positive to negative and vice versa.

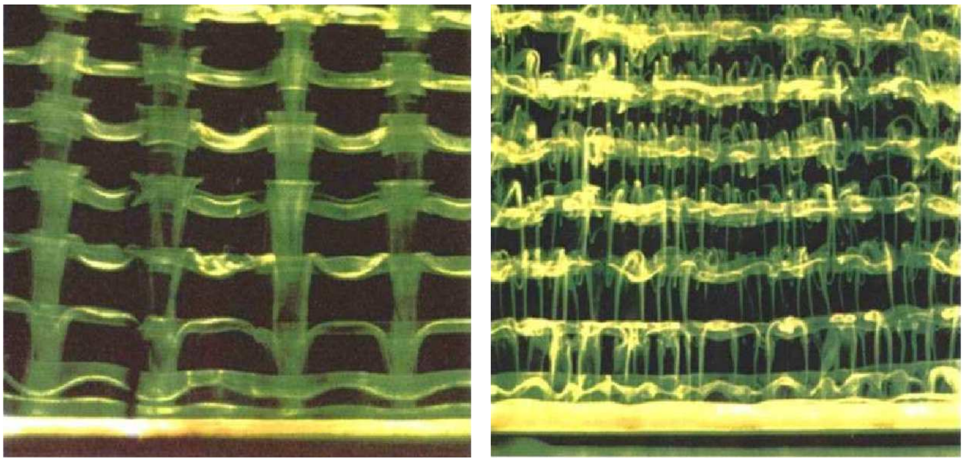

(a) Mode A at $Re = 200$ (b) Mode B at $Re = 270$

FIGURE 1.3: Dye visualisations from Williamson (1996b) showing the three-dimensional modes from above.

Early numerical simulations by Zhang *et al.* (1995) and Mittal & Balachandar (1995) were able to re-create certain aspects of the three-dimensional, experimental flow but did not offer an explanation for the mechanisms that triggered the instabilities. Again, Williamson (1996a) was the first to report his findings for the suspected source of this instability. He conjectured that the mode A instability scales on the core of the vortex and is due to an elliptic instability. Later support for this argument has been offered by Leweke & Williamson (1998b) and in the numerical and Floquet analysis of Thompson *et al.* (2001b).

The second transition in the three-dimensional wake is to the 'mode B' form of vortex shedding. This mode is observed for $230 < R < 260$, during which range of Reynolds numbers the A and B modes both exist (Williamson 1996a). At $Re = 260$, the mode B form of shedding is fully developed and possesses a critical span-wise wavelength of $\lambda \approx 0.8D$ (Henderson 1997; Barkley *et al.* 2000; Williamson 1996a). The comparative wavelengths of the two modes are clearly visible in figures 1.3(a) and 1.3(b).

In a numerical study, Henderson (1997) investigated the non-linear response of the cylinder wake and found that the transition to the mode B wake occurred via a supercritical bifurcation. Furthermore, other studies have determined that the A and B modes of shedding are two clearly distinct shedding forms that scale on different aspects of the two-dimensional base flow. In contrast to mode A, mode B shedding has an in-phase symmetry and from one half-cycle to the next, the orientation of the streamwise vortices at a given point remains the same (Williamson 1996a; Leweke & Williamson 1998b). It was conjectured by Williamson (1996a) that the mode B instability scales on the braid shear layer, which is an area of strong hyperbolic flow, and mode B is therefore due to a hyperbolic instability.

As was mentioned previously, there is a range of Re where both the A and B modes of shedding may be observed. The numerical study by Thompson *et al.* (1996) found that both the A and B modes occur at $Re = 250$, which was in agreement with the experimental findings of Williamson (1996a). Barkley *et al.* (2000) refer to this scenario as a 'mixed-mode state' and explain the presence of both modes by investigating the coupling between the two. From this, they determined that mode A acts to destabilise mode B, while mode B act to stabilise mode A. Furthermore, the discontinuity originally detected by Williamson (1996a) in the $St - Re$ curve for the mode B transition may be explained by the presence of the two separate frequencies in the energy spectrum when both A and B modes are present.

The full $St - Re$ curve, taken from Williamson (1996a), is given in figure 1.4 and shows the discontinuities detected in St with both the hysteretic transition to mode A and the 'mixed mode state' when both modes A and B are observed. Also shown here is the smooth increase in St during the laminar regime when either parallel or oblique shedding is taking place behind the cylinder.

While there exists a range of Re when both three-dimensional instabilities may occur, studies indicate the modes A and B do not actually co-exist. Rather, the two modes swap intermittently during the energy transfer phase (Williamson 1996a). As Re is increased, the gradual transfer of energy takes place from mode A to mode B, until $Re \approx 260$, when mode B has reached saturation.

Investigation of flows around bluff bodies of various geometries have found the A and B modes of shedding to be quite robust. Although the critical Reynolds number of transition may vary slightly, wake modes with the same spatio-temporal symmetry

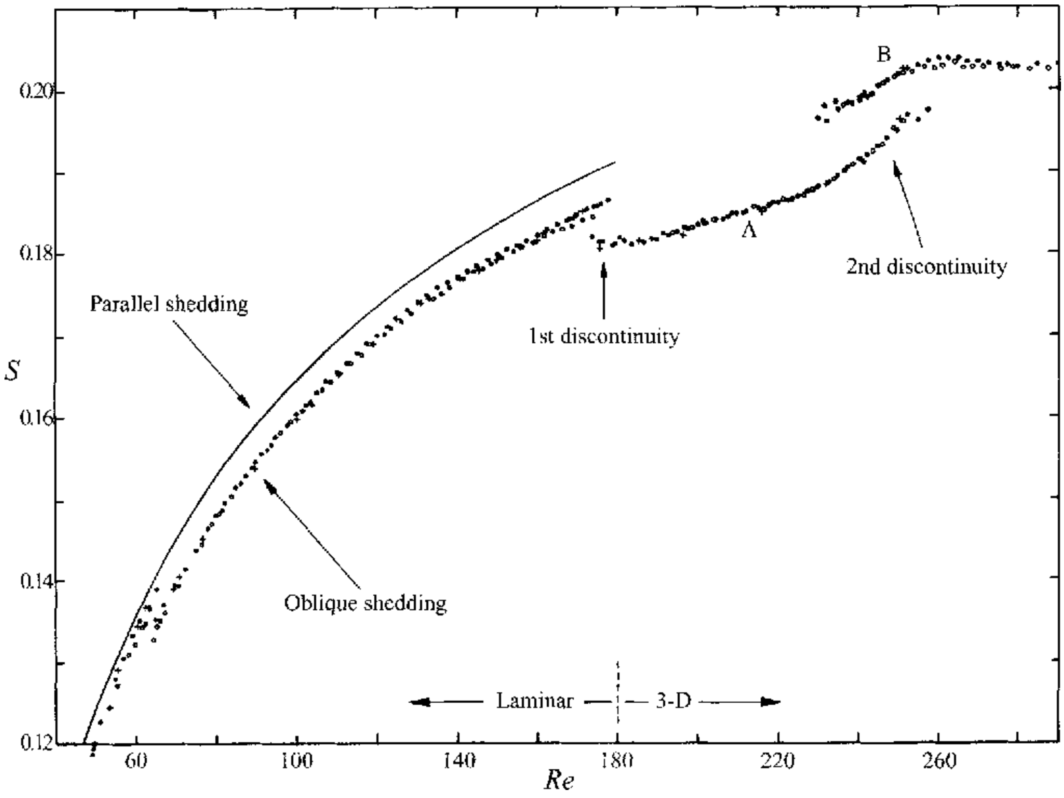

FIGURE 1.4: Variation in St throughout the different flow regimes. Taken from Williamson (1996a).

have been found to occur around both square and 'bluff elongated' cylinders (Robichaux *et al.* 1999; Ryan *et al.* 2005). Moreover, the dominant mode of instability has been found to switch, depending on the aspect ratio of the body, and thus mode B may appear before mode A (Ryan *et al.* 2005).

Although the two main three-dimensional transitions in the cylinder wake have been outlined above, stability analyses have indicated that a third, quasi-periodic mode is possible with a critical Reynolds number greater than that for mode A or B. In the numerical simulations of Blackburn & Lopez (2003), a third mode is predicted, which has complex Floquet multipliers, indicating that the period of the instability is not equal to the period of the two-dimensional base flow. This quasi-periodic mode has a wavelength intermediate to those of A and B, with similar modes predicted by Barkley & Henderson (1996) in the wake of the circular cylinder and by Robichaux *et al.* (1999) in the wake of a square cylinder.

1.1.2 Flow around a rotating cylinder

When a cylinder in a free stream is subjected to an imposed rotation, several effects become apparent. This rotation creates an asymmetry in the wake that becomes more pronounced as the rotation rate increases (Tang & Ingham 1991). The non-dimensional rotation rate, α, is the ratio of tangential velocity on the surface of the cylinder divided by the free-stream velocity. This imposed rotation also has a strong influence on the lift and drag forces experienced by the cylinder, as well as having the ability to suppress the unsteady flow.

Magnus effect and potential flow

One of the first to investigate this rotational effect was Prandtl & Tietjens (1934), whose experiments are still widely referenced today as one of the seminal works on the topic. When the cylinder is rotating, the acceleration of fluid over one side of the body creates a low pressure region that results in a net lift force on the cylinder. This is referred to as the Magnus effect. Prandtl (1926) argued that for a cylinder rotating in a free-stream, there exists a maximum value of the lift coefficient, C_L, that may be obtained in such a case. This maximum C_L would correspond to the instant when the cylinder is rotating sufficiently fast that the boundary layer on the surface is accelerated at all locations. Prandtl theorised that no further eddies could be detached from the cylinder once this critical circulation was reached. The inviscid theory uses a potential vortex to model the solid body cylinder rotation, and in this way, Prandtl found the maximum value of C_L to be equal to 4π at the instant when the two stagnation points just coincide in the flow. Furthermore, this is predicted to occur when the rotational velocity of the vortex equates to a solid body cylinder rotation of $\alpha = 2$ (Prandtl 1926; White 1999).

For the potential flow solution, theory states that closed streamlines around the cylinder will not exist for small values of α. Instead, stagnation points will be present on the cylinder surface but displaced from their position at the front and rear of the cylinder, as is the case for $\alpha = 0$. This scenario is shown in figure 1.5(a), along with the $\alpha = 2$ solution when the stagnation points merge (figure 1.5(b)), and the case of higher rotation, when closed streamlines form around the body (figure 1.5(c)). It must be noted, however, that in the case of *viscous* flow, closed streamlines will occur for all $\alpha > 0$, although they may be very close to the cylinder surface.

During unsteady, viscous flow, two separation points are present on either side of the cylinder that are displaced away from the body and in the direction of rotation. This is in contrast to the steady flow case, when the front stagnation point moves opposite the direction of rotation, similar to figure 1.5(a) (Chew *et al.* 1995; Kang *et al.* 1999). The entrained fluid layer contained within the closed streamlines for $\alpha > 2$ increases in thickness with α and the stagnation or separation points are displaced further from the cylinder surface (Ingham 1983; Coutanceau & Ménard 1985; Chew *et al.* 1995; Mittal & Kumar 2003).

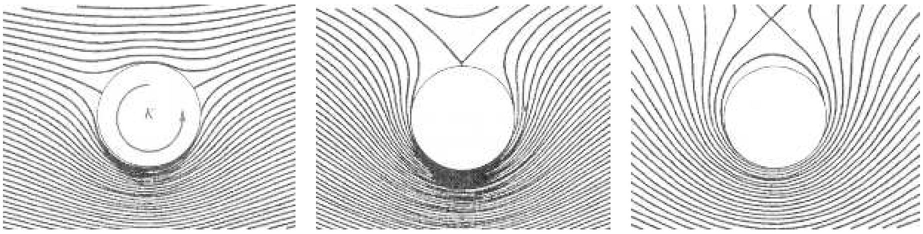

(a) $\alpha < 2$ (b) $\alpha = 2$ (c) $\alpha > 2$

FIGURE 1.5: Images from White (1999) showing the potential flow solutions for various cylinder rotation rates.

Steady flow

At Reynolds numbers $Re \leq 60$, investigations have shown that imposing a cylinder rotation results in a steady flow which differs significantly to that behind a non-rotating cylinder. Numerical simulations show that the body rotation is able to eliminate one or both of the recirculation zones behind the body (Ingham 1983; Tang & Ingham 1991). Ingham (1983) found at $Re = 20$ that the recirculation zones were suppressed when even very small rotation rates ($\alpha = 0.1$) were employed. However, it is expected that the recirculation zone(s) would make an appearance as $\alpha \rightarrow 0$, as the flow conditions approach those for the non-rotating cylinder. At larger values of Re, when unsteady flow is observed for the non-rotating case, the body rotation is able to suppress the onset of unsteady flow. Tang & Ingham (1991) have observed the formation of steady recirculation zones behind the rotating cylinder at $Re = 60$. Moreover, they find that as the rotation rate increases beyond $\alpha = 0.5$, the smaller of the two recirculation bubbles shrinks and disappears entirely, indicating a mechanism whereby the onset of unsteady flow may be suppressed.

Unsteady flow behind the rotating cylinder

As for the case of the non-rotating cylinder, increasing the Reynolds number of the flow results in a transition to unsteady flow behind the rotating cylinder. This transition may be strongly affected by any perturbations in the motion of the body. Jaminet & Van Atta (1969) found that for $Re < 48$, when vortex shedding would normally not exist, that a vortex street could be generated by the rotation of the cylinder. This shedding frequency was generally equal to the frequency of cylinder rotation and as such Jaminet & Van Atta (1969) attributes this unsteady flow to a 'whipping' motion of the body as it rotates. This result highlights the difficulties present in experimental investigations when small perturbations in the flow can trigger the onset of an instability.

When unsteady flow is observed behind the cylinder at small rates of rotation, the shedding takes the form of the Bénard-von Kármán vortex street (Jaminet & Van Atta 1969; Díaz *et al.* 1983; Mittal & Kumar 2003). The asymmetry of the rotational effects means that the shedding and boundary layer separation tends to favour the side of the cylinder with motion opposing the free-stream (i.e. with an imposed flow reversal) (Díaz *et al.* 1983). This asymmetry in the wake was also observed by Coutanceau & Ménard (1985) and Badr & Dennis (1985), who commented upon the inequality of strength in the vortices shed from either side of the rotating cylinder. As α is increased, the unsteady wake narrows and is displaced further to one side of the cylinder (Díaz *et al.* 1983; Mittal & Kumar 2003). Jaminet & Van Atta (1969) observed that both sides of the vortex street were displaced in the direction of motion of the cylinder surface, although not equally, so that the distance between the two was reduced. This narrowing of the wake has been linked to changes observed in the shedding frequency, although the exact relationship is still not well understood.

Conflicting reports have been given as to the relationship between shedding frequency and Reynolds number when the cylinder is rotating. Several authors have found St to increase with Re, with the strength of the shed vortices gradually decreasing until, at a critical value of rotation, the shedding is suppressed (Jaminet & Van Atta 1969; Díaz *et al.* 1983; Chew *et al.* 1995). However, the relationship between Strouhal number and rotation rate is less clearly defined.

The experimental studies of Van Atta (1997), Jaminet & Van Atta (1969) and Barnes (2000) at $Re < 150$ found St to increase steadily with the rotation rate and Van Atta (1997) explains this phenomenon as follows: Studies have observed that rotation of the cylinder causes the two separation points (located symmetrically near the top and bottom cylinder surfaces for $\alpha = 0$) to displace toward the rear of the cylinder surface and move closer together when the cylinder is rotating. This narrowing of distance between the separation points causes a reduction in the width of the wake. As the characteristic shedding frequency is defined as the free-stream velocity divided by the characteristic length (the wake width), this would in turn result in an increase in the frequency of shedding. Therefore, St should be expected to increase with α.

In contrast to the above-mentioned results, the two-dimensional numerical investigation of Mittal & Kumar (2003) at $Re = 200$ found a very slight decrease in St with increasing α, while the results of Kang *et al.* (1999) for $Re = 60, 100$ and 160 showed negligible change. Mittal & Kumar (2003) speculate that, in general, the computations show a decrease of St with α, while the experiments show an increase. They postulate that this effect may be due to the occurrence of three-dimensional centrifugal instabilities in the experiments, which interact with the vortex shedding process, thereby increasing the observed values of St.

Suppression of unsteady flow

As the rotation rate of the cylinder is increased in the unsteady regime, it is observed that, for large enough rotation rates, the unsteady flow may be suppressed. The critical rotation rate, α_c, at which this happens has been reported in several studies to occur at $\alpha_c \approx 2$ (Mittal & Kumar 2003; Díaz *et al.* 1983; Chew *et al.* 1995) and this rotation rate is in surprisingly good agreement with that first derived by Prandtl from the inviscid theory. However, at Re less that about 200, the value of α_c is slightly lower, with $1.3 < \alpha_c < 2$ reported by Kang *et al.* (1999) and Jaminet & Van Atta (1969). Kang *et al.* (1999) found that the value of α_c increases logarithmically with Re. This dependence led them to conclude that increasing Re acts to destabilise the fluid passing around the cylinder, while increasing α acts to stabilise it.

Jaminet & Van Atta (1969) explained the mechanism for suppression of unsteady flow as the merging on both sides of the vortex street as one side is displaced into the other via the cylinder rotation. This results in suppression of shedding from both sides of the cylinder simultaneously. Beyond this value of α, only random and infrequent shedding is detected. The suppression of vortex shedding for $\alpha_c > 2$ appears to hold at much higher Re as the same thing was observed by Díaz *et al.* (1983) at $Re = 9000$ and by Chew *et al.* (1995) and $Re = 1000$. For $\alpha > 2$, the unsteady wake is prevented from forming due to the closed streamlines and the thickening fluid layer surrounding the rotating cylinder (Mittal 2001; Labraga *et al.* 2002; Díaz *et al.* 1983). For rotation rates beyond $\alpha = 2$ in the extensive investigation by Mittal & Kumar (2003), the authors claim to have detected an unstable regime for $4.34 < \alpha < 4.7$ in which one-sided vortex shedding takes place. The existence of this unsteady region has yet to be confirmed experimentally.

In summary, the rotation of the cylinder acts on the flow in several ways. When the cylinder is rotating in a viscous fluid, the stagnation and separation points are displaced away from the cylinder surface and into the fluid stream. During the unsteady regime, the wake is displaced in the direction of the body rotation and increasing α causes the wake to narrow. As the rotation rate is increased beyond a critical value of $\alpha_c \approx 2$, the vortex shedding in the wake is suppressed and the cylinder is surrounded by an entrained fluid layer that thickens with increasing α.

Lift and drag forces due to rotation

For the Reynolds numbers considered in the present study, the greatest contribution to the lift for the rotating cylinder (for $\alpha \leq 1$) is given by the pressure, rather than the frictional (viscous) forces (Tang & Ingham 1991; Chen *et al.* 1993; Kang *et al.* 1999; Mittal & Kumar 2003). However, for the drag force, the frictional drag is of the same order of magnitude as the pressure drag (Tang & Ingham (1991) and Kang *et al.* (1999) cite values of the coefficient of lift due to the pressure components as being greater than 90%). The percentage of this contribution appears to increase with Re. For $0 < \alpha < 2.5$, the pressure and frictional components of the drag change dominance (Kang *et al.* 1999). At lower magnitudes of rotation, the pressure drag dominates. However, as the rotation increases, this contribution decreases and at $\alpha \approx 1.5$, the frictional drag provides the greatest contribution to the total drag on the cylinder.

Several studies have focused on the magnitude of the lift and drag forces experienced by a rotating cylinder. The lower Re study of Kang *et al.* (1999) finds that the total lift is nearly independent of Reynolds number (for $Re < 200$), while the drag is not and C_D decreases with Re. During the unsteady regime, the fluctuation amplitudes of the lift and drag increase with Re. However, only the amplitude of the fluctuating drag shows an increase with α, while the amplitude of the lift stays fairly constant. This is until $\alpha \approx \alpha_c$, when the amplitudes decay as the shedding is suppressed (Kang *et al.* 1999).

Concerning the variation in the lift and drag forces with α, it has been observed that the magnitude of the lift on the cylinder increases with α, while the drag shows a slight decrease (Badr *et al.* 1989; Ingham & Tang 1990; Kano & Yagita 2002). At higher rotation rates ($3.2 < \alpha < 4.3$) and $Re = 200$, the motion of the cylinder is able to generate a net thrust (Mittal & Kumar 2003). However, the potential benefits of this are offset by the large power needed to rotate the cylinder at such speeds.

Chew *et al.* (1995) found that, at $Re = 1000$, the magnitudes of the mean lift and drag increase almost linearly with α for small rotation rates and then taper off to approach asymptotic values. These findings supported Prandtl's hypothesis of a limiting value for the lift. However, several other studies have achieved values of the lift coefficient well in excess of the 4π value put forward by Prandtl. The reason for this is attributed by Mittal (2004) to the three-dimensional and end effects of the experimental flows limiting the achievable lift.

Three-dimensional effects

As yet, only a limited amount of research is available on the three-dimensional instabilities occurring behind a rotating cylinder. Three-dimensional simulations by Mittal (2004) found that the steady flow at high rotation rates exhibited a span-wise flow that is attributed to a centrifugal instability. This could not be detected in the two-dimensional simulations. Several other papers make reference to similar types of centrifugal instabilities, such as that leading to the formation of Taylor-Görtler vortices, which may occur behind the rotating cylinder (Chew *et al.* 1995; Mittal & Kumar 2003).

1.1.3 Flow past a cylinder near a wall

Early studies by Taneda (1965) showed that the presence of a wall near the cylinder acts to stabilise the flow. When the stationary cylinder is placed adjacent to a plane wall, the developed boundary layer upstream of the cylinder acts to dramatically affect the flow. In the current study, the plane wall has been given an imposed velocity, which serves to eliminate boundary layer effects. However, in order to clearly understand the effects of this imposed wall velocity, it is useful to consider first the case of the cylinder position fixed near the wall, and then with the cylinder translating along the wall. This comparison can help to pinpoint effects that are purely due to the developing wall boundary layer. In addition to the effects brought about by the relative wall velocity, the current study also includes the rotation effect of the cylinder near the wall. Only a few studies have considered this effect, acting either with the stationary or moving adjacent wall. These results, and the difference that a body rotation introduces, shall also be discussed in the following sections.

Steady flow and the suppression of vortex shedding

Bearman & Zdravkovich (1978) refer to the wall as a solid boundary that prevents velocities normal to the surface. In this way, it would be expected that the wall could exert some control over the wake. In fact, this appears to be the case, and the stabilising effect of the wall has been discussed by Arnal *et al.* (1991), who investigated the flow around a wall-mounted square cylinder. They found that the presence of the wall delayed the onset of unsteady flow, from $Re \approx 50$ for the body in a free-stream, to $Re \approx 100$ when the wall was present.

The steady flow around a wall-mounted obstacle is typified by a single recirculation zone, which has a separation point on the body and a reattachment point on the downstream wall, such as that over a backward-facing step (Armaly *et al.* 1983). Many variables can act to modify this flow, including the motion of the wall relative to the cylinder, cylinder rotation and, perhaps the most-studied of these, the distance between the cylinder and the wall, G. When even small amounts of fluid are able to pass between the cylinder and the wall, the recirculation zone can no longer attach to the wall and the separation and reattachment points must instead exist on the cylinder surface. When the cylinder is positioned near (but not in contact with) the moving wall, the fluid passing through the gap is accelerated (Nishino *et al.* 2007; Huang & Sung 2007; Kano & Yagita 2002). In a flow such as this, Nishino *et al.* (2007) found that the length of the recirculation zone behind the cylinder increases dramatically as $G/D \rightarrow 0$. Additionally, Arnal *et al.* (1991) found that the introduction of a relative wall velocity can create a second recirculation zone, positioned behind the body, between the primary recirculation zone and the wall.

One of the first studies of the flows around a cylinder in contact with, and rolling along, a wall was undertaken by Bhattacharyya *et al.* (2004). In that study, the relative motion of the wall was equal to both the free-steam velocity and the tangential velocity on the cylinder surface. That study was carried out with the use of steady, two-dimensional simulations. In this way, they were able to investigate, in some detail, the flows near the contact point. They found that flow in this region is characterised by the presence of two jets of fluid. On the upstream side of the cylinder, fluid is being carried into the contact region by both the cylinder surface and the wall. This fluid, being unable to pass between the cylinder and the wall, then leaves the region as an outflow jet. Similarly, on the downstream side of the cylinder, fluid is being carried away from the contact point by both the cylinder surface and the wall, thereby resulting in a jet of fluid into the contact region. In their study, Bhattacharyya *et al.* (2004) also make the important comment that the local flow near the contact point is, in reality, a lubrication flow.

One significant way in which the wall proximity is able to alter the flow is via the suppression of vortex shedding when the gap ratio is below some critical value, $(G/D)_c$. It has been noted by Lei *et al.* (1999) that, at higher Re, the wall effects begin to alter the vortex shedding when the gap ratio is less than ≈ 2. For gap ratios greater than this value, the flow is comparable to that around a cylinder in a free-stream.

For Reynolds numbers greater than about 300, the critical gap ratio for a stationary cylinder near a wall lies in the range $0.2 < (G/D)_c < 0.3$ and remains nearly constant as Re is increased (Bearman & Zdravkovich 1978; Lei *et al.* 1999, 2000; Huang & Sung 2007). For $Re < 300$, the relationship appears to be somewhat different. Lei *et al.* (2000) state that $(G/D)_c$ goes to infinity as $Re \rightarrow 0$, in accordance with the fact that there is no vortex shedding for $Re < 40$, even if the body is infinitely far from the wall. Likewise, they find that $(G/D)_c \approx 1$ at $Re = 100$ and they explain the increase of $(G/D)_c$ at low Re through the fact that thickening of the shear layers occurs as Re is reduced. This means that the vorticity in cylinder and wall shear layers will interact to cancel each other, even at quite large gap ratios. This inverse relationship of $(G/D)_c$ and Re also appears to hold true when the wall is moving (Huang & Sung 2007).

As mentioned above, Lei *et al.* (2000) offered the explanation for the suppression of vortex shedding as the interaction of opposite signed vorticity in the shear layers on the bottom of the cylinder and the wall. When G/D is sufficiently small, these regions of opposite signed vorticity cancel each other and the resulting vorticity in the lower shed shear layer is very weak. Hence, this lower shear layer will not interact with the shear layer on the top of the cylinder and no vortex shedding will result. An alternative explanation is offered by Nishino *et al.* (2007), who state that for the cylinder near a moving ground, the nearby wall can have an effect similar to that of a splitter plate in the wake. They propose that the ground restricts the appearance and growth of disturbances in the wake that can lead to an absolute instability and the onset of Bénard-von Kármán vortex shedding. Rather than the presence of an absolute instability, they observe that the wake displays only convective instabilities as the cylinder nears the wall.

Imposing a rotation on the cylinder near the stationary wall does not appear to have a strong destabilising effect on the flow. For the rotating cylinder at a Reynolds number of 200, Cheng & Luo (2007) found that for $-1 < \alpha < 1$, the flow was always steady. Forward rotation (in which the free-stream side of the cylinder is opposing the fluid motion) simply acted to displace the recirculation zone away from the wall.

Unsteady flow

When vortex shedding is present for the cylinder near the wall, the strength of the vortex shedding decreases as the gap ratio is decreased (Lei *et al.* 1999). Studies have detected several different shedding regimes as the cylinder approaches the wall. Experiments by Price *et al.* (2002) at higher Re detected periodic flow for all values of G/D. However, in the case of small gap ratios, this was associated with periodicity in the upper shear layer that may not be present in low Re flows.

One of the earliest studies of flow around a cylinder near a wall was by Taneda (1965), who found that when the cylinder is moved parallel to the plane wall, and the distance between the two is small enough, the vortex street can be altered to a single row, which appeared to be shed from one side of the body only. Much later, this type of flow was detected in the simulations of Huang & Sung (2007), who found that vorticity from both sides of the body rolled up and shed in a single vortex when the gap ratio was small enough. A similar trend of one-sided shedding may be observed at small G/D when the wall acts as a free surface (Reichl *et al.* 2005).

Another form of shedding that appears is that of intermittent shedding. This form has been detected in several investigations of the cylinder near a stationary wall (Nishino *et al.* 2007; Zdravkovich 1985b). Furthermore, studies of the flow around the rotating cylinder near a wall (Cheng & Luo 2007), and of the flow around a non-rotating cylinder near a moving wall (Nishino *et al.* 2007) have found similar regimes and tend to support these results. However, as the results for the cylinder near a wall are limited and the different possible configurations, including changes in distance from the wall, rotation rate and relative wall velocity are numerous, it is difficult to say which, if any, of these regimes may be purely an effect of *Re*.

When the cylinder is moving relative to the wall, the flow through the gap region is much greater than in the stationary wall case, which may aid the onset of unsteady flow. However, even when the gap ratio is reduced to zero and no flow may pass through, Arnal *et al.* (1991) found that the moving wall encouraged the onset of unsteady flow, compared to the stationary wall case. This was explained by the generation of vorticity on the downstream side of the body in the corner near the wall. This vorticity was of opposite sign to that generated over the top of the body, allowing wall vorticity to destabilise and 'lift-off' from the wall.

Dipankar & Sengupta (2005) state that the instability that arises between the cylinder wake and the wall is due to the interaction of the convecting vortex core shed from the cylinder. This was first proposed by Sengupta *et al.* (2003), who tested this theory by using a rotating cylinder positioned above the wall to act as a captive vortex. The movement of this 'vortex' was found to create a weak streamwise pressure gradient, which in turn destabilises the wall-shear layer. Furthermore, experiments by Lim *et al.* (2004) found that the direction of rotation of this captive vortex impacts strongly on the type and degree of instability that is observed. Only when a convecting vortex is moving significantly slower than the free-stream will unsteady flow occur. Furthermore, the instability effects will be significantly greater when the vorticity in the wall shear layer and the convecting vortex are of opposite sign. In such cases, the adverse pressure gradient imposed by the convecting vortex will be much larger and will destabilise the wall shear layer downstream of the flow. When the vorticity of the two are of the same sign, the disturbance in the flow is much less and, depending on the distance between the vortex and the wall, the shear layer may appear unaffected.

The vortex shedding frequency behind the wall mounted cylinder remains fairly constant with changes in *Re*, and instead seems to be far more sensitive to small changes in the gap ratio when the cylinder is close to the wall (Huang & Sung 2007; Lei *et al.* 1999, 2000; Arnal *et al.* 1991). The low *Re* investigations, undertaken by Taneda (1965), showed that as the distance between the cylinder and the moving wall is reduced, the wavelength of the vortex street increases. This was supported by the later work of Lei *et al.* (2000) and Huang & Sung (2007), who found that, although

St is only weakly dependent on the gap ratio for $G/D > 0.5$, once the cylinder is very close to the wall, the frequency of shedding decreases steadily.

Lift and drag forces induced by the wall

The lift and drag forces on the stationary cylinder near the wall are strongly affected by the position of any stagnation points on the surface of the cylinder. As the cylinder approaches very close to the wall, a stagnation point will appear in the fluid in the contact region. Small changes in the distance to the wall can result in more fluid being accelerated through the gap and a movement of the stagnation point, such as that observed by Bearman & Zdravkovich (1978). As a result, it is to be expected that the lift force will be strongly dependent on the exact value of G/D when the cylinder is very near the wall.

As the cylinder moves nearer to the stationary wall, the coefficient of lift is seen to increase slowly until $(G/D)_c$ is reached, at which point the lift undergoes a rapid increase, until a maximum is reached at $G/D = 0$ (Zdravkovich 1985a; Huang & Sung 2007). Consistent with the phenomenon of vortex suppression described above, the amplitude of the fluctuating lift reduces as $G/D \to 0$ and the shedding dies out (Lei *et al.* 2000). This result does not appear to change significantly when the moving wall is present. Nishino *et al.* (2007) find a similar trend, with the lift coefficient rapidly increasing as G/D decreases to less than about 0.5. This indicates that the thickness (or existence) of the wall boundary layer has little effect on the lift force experienced by the cylinder when the body is very close to the wall.

The drag force for the cylinder near the stationary wall shows a different relationship with G/D. Once the cylinder is very near the wall, the coefficient of drag rapidly decreases to a minimum at $G/D = 0$, corresponding to the case when the cylinder is as fully submerged in the wall boundary layer as is possible (Zdravkovich 1985a). In the case of the moving wall, studies by Huang & Sung (2007) and Nishino *et al.* (2007) have observed a similar trend. For $G/D < 0.5$, the cylinder next to a stationary wall experiences a rapid drop in drag. However, for the moving wall, the drag does not reach a minimum at $G/D = 0$, but rather, remains fairly constant for $G/D < (G/D)_c$. This is taken by Nishino *et al.* (2007) as an indicator that once the vortex shedding has ceased, the drag force will not decrease further due to wall effects if the wall boundary layer is sufficiently small. This leads to a value of C_D that is slightly larger than for the cylinder near a stationary wall.

Some results have been obtained by Cheng & Luo (2007) for the effect of rotation on the lift and drag of the near-wall cylinder. The wall was stationary relative to the cylinder centre, and α was varied between -1 and 1. When the cylinder rotates so that the surface velocity furthest from the wall is opposing the free-stream flow, the cylinder experiences a net pressure force pushing it toward the wall. This was true at the smallest gap ratio studied by Cheng & Luo (2007) ($G/D = 0.2$). When the free-stream side of the cylinder is moving in the same direction as the flow, the fluid over the top of the body is accelerated, creating a low pressure and resulting in a lift force directed away from the wall. The drag is found to increase steadily as the rotation varies from $\alpha = -1$ (assisting the free-stream flow over the body), to $\alpha = 1$ (opposing it).

1.2 Flow past a sphere

1.2.1 Flow past a sphere in a freestream

The flow past a sphere has historically played a large part in the analysis of particle-laden flows and heat transfer. In recent times, the applications to biological flows and cell interactions have received an increasing amount of attention. Furthermore, the axisymmetry of the sphere provides a simplified geometry that has allowed it to be studied analytically, experimentally and numerically for over 150 years. The following sections summarise the findings for fluid flow around a sphere

Axisymmetric steady flow

As for the flow around a circular cylinder, the flow around a sphere remains steady and attached at low Reynolds numbers. For $Re < 0.1$, the inertia forces of the fluid may be neglected, and the early approximations of Stokes and Oseen to the Navier-Stokes equations may be used to describe the flow. As Re is increased, the flow around a sphere remains steady but these approximations break down and a more complete form of the Navier-Stokes equations must be used to take into account the inertial effects of the flow.

Studies have shown that the flow around a sphere remains attached to the surface until $Re \approx 20$ is reached (Pruppacher *et al.* 1970; Masliyah & Epstein 1970; Dennis & Walker 1971; Johnson & Patel 1999). When the flow first separates, the recirculation zone behind the body remains symmetric with respect to the streamwise centreline of the sphere and the flow has a fixed line of separation encircling the sphere. This recirculation zone takes the form of ‘vortex ring’, as described by Taneda (1956a), who observed it in early experiments at low *Re*. In this symmetric regime, the drag coefficient decreases at close to Re^{-1}, with increasing *Re* up to 100 (Kawaguti 1955; Masliyah & Epstein 1970).

The downstream length of the symmetric recirculation region grows at a rate close to the logarithm of the Reynolds number (Taneda 1956a; Johnson & Patel 1999; Tomboulides & Orszag 2000). This is unlike the recirculation zone behind the circular cylinder, which grows approximately linearly with *Re*, as described in section 1.1.1. The same recirculating structures have been detected in the wake behind falling droplets in a liquid-liquid system by Magarvey & Bishop (1961b). In this case, the wake flows appears largely unaffected by the change of boundary condition on the surface of the sphere, which is no longer a no-slip condition in the case of liquid drops.

Non-axisymmetric steady flow

As the Reynolds number increases, the flow behind the sphere undergoes a transition from steady axis-symmetric to steady asymmetric flow. Studies have found that this transition occurs at $Re \approx 210$ (Magarvey & Bishop 1961a; Magarvey & MacLatchy 1965; Natarajan & Acrivos 1993; Johnson & Patel 1999; Ghidersa & Dušek 2000; Thompson *et al.* 2001a). This change in the flow is referred to as ‘regular’ transition, due to fact that the flow remains steady, and was predicted to occur in the stability analyses of Natarajan & Acrivos (1993). The Landau modeling undertaken by Thompson *et al.* (2001a) found this transition to be supercritical.

The regular transition leads to the development of a two-tailed wake, some of the first experimental observations of which were by Magarvey & Bishop (1961a) and Magarvey & MacLatchy (1965). They found that the asymmetric wake pattern results in a net sideways force on the falling sphere. Later studies by Johnson & Patel (1999) and Thompson *et al.* (2001a) describe the double tail as being composed of a counter-rotating vortex pair, with the two vortices imposing a velocity on each other, causing them to be convected away from the streamwise centre-line of the sphere. Johnson & Patel (1999) speculate that the transition to non-axisymmetric flow is due to the low pressure core of the axisymmetric toroidal vortex becoming unstable. This results in an azimuthal pressure gradient that opens up the separation region behind the sphere and allows the flow of fluid to pass through.

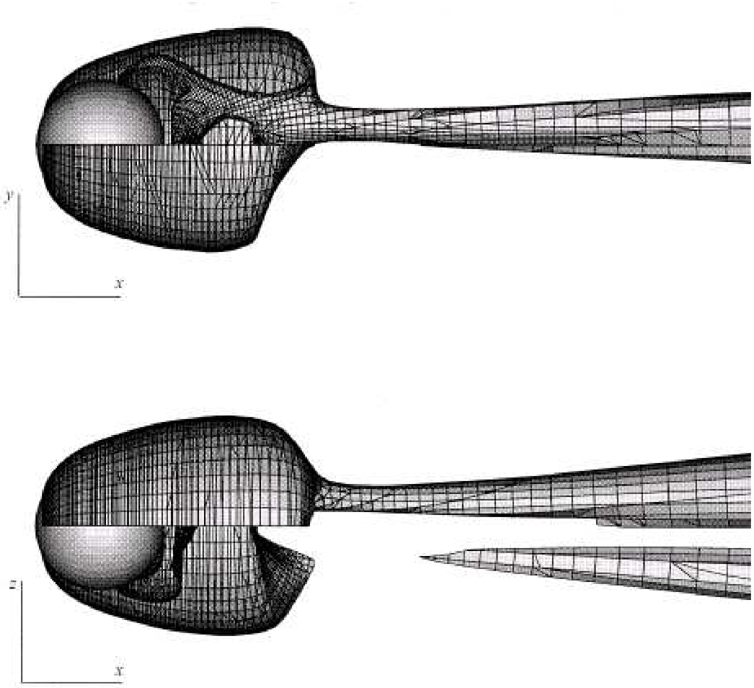

Figure 1.6: Structures observed in the of numerical simulations of Johnson & Patel (1999), showing the steady two-tailed sphere wake at $Re = 250$. One quadrant is cut away to show the internal structure.

A surface contour showing the structure of this two-tailed wake is given in figure 1.6 from the numerical simulations of Johnson & Patel (1999). The figure shows two views of the asymmetric mode, and the internal structure can be viewed via the cutaway quadrant in each image. The orientation of this flow is arbitrary and depends only on the initial conditions of the flow. Findings of Natarajan & Acrivos (1993) for the steady flow regime indicate that although small variations are present between the freely-falling and fixed sphere cases, the effects of dynamic sphere-flow interactions are minimal for these types of flows. Both the flow transitions and the wake structures are largely unaffected by any sideways movement of the sphere. The same may not be the true for the unsteady flow regime, as shall be discussed below.

Unsteady flow

It was noted in the simulations of Thompson *et al.* (2001a) that during the steady flow regime, the two tails described above kink together several diameters down-stream of the body. This kinking is more pronounced as Re increases and is possibly linked to the unsteady transition. Experiments have observed a similar type of periodic undulation in the wake just prior to the onset of vortex shedding (Taneda 1956a; Magarvey & Bishop 1961a; Sakamoto & Haniu 1995; Ormières & Provansal 1999). This waviness marks the onset of unsteady flow and it was noted by Schouveiler & Provansal (2002) that a kinking observed in this wake bore strong similarities to the long wavelength (or Crow-type) instability, which could be related to the onset of vortex shedding. As yet, this has not been determined definitively and requires further study.

Various numerical and experimental works have observed the transition to unsteady flow to occur at $270 < Re < 280$ (Ormières & Provansal 1999; Johnson & Patel 1999; Schouveiler & Provansal 2002; Magarvey & Bishop 1961a; Magarvey & MacLatchy 1965), as did the stability analysis of Natarajan & Acrivos (1993), which was applied to the axi-symmetric base flow. In the latter study, a value of $Re \approx 277$ was obtained for the transition. This transition range of Re is supported by the Landau-type modeling of Ghidersa & Dušek (2000) and Thompson *et al.* (2001a) who predict a value of approximately 272 for the unsteady transition. The stability analyses also indicate that the unsteady flow emerges via a supercritical Hopf bifurcation (Natarajan & Acrivos 1993; Schouveiler & Provansal 2002; Thompson *et al.* 2001a), a finding that is supported by the lack of hysteresis detected experimentally (Ormières & Provansal 1999).

Following the unsteady wavy mode described above, further increase in Re leads to fully formed vortex shedding. Certain distinct differences have appeared in the literature regarding the shedding of vortices from either one or both sides of the body. In all cases, the shedding takes the form of vortex 'loops' or 'hairpins' and the mode displays a planar symmetry. For a sphere that is held rigidly fixed in a freestream, many experimental and numerical investigations have observed an asymmetric shedding of vortices over only one side of the body (Achenbach 1975; Sakamoto & Haniu 1995; Ormières & Provansal 1999; Leweke *et al.* 1999), and an example of this is shown in figure 1.7(a). This wake configuration is quite different to the wake behind a freely-falling spherical drop, described by Magarvey & Bishop (1961a) and Magarvey & MacLatchy (1965), who found the loops were shed from opposite sides of the sphere. This is likely to be due to the sideways motion permitted to the spherical droplet as it descends.

Figure 1.7(b) shows the schematic of the vortical structures observed by Achenbach (1975), with the direction of vortex rotation indicated by arrows. Mittal (1999) found that the symmetry plane of this flow remained fixed for $Re < 350$, with the orientation of the symmetry being arbitrary, as was the case for the asymmetric steady mode. He also found that when the sphere is held fixed, the shedding induces a transverse force on the sphere that is approximately an order of magnitude smaller than the drag. While this force is smaller, it is possible that the motion induced on the free sphere may in turn trigger shedding from opposite sides of the sphere.

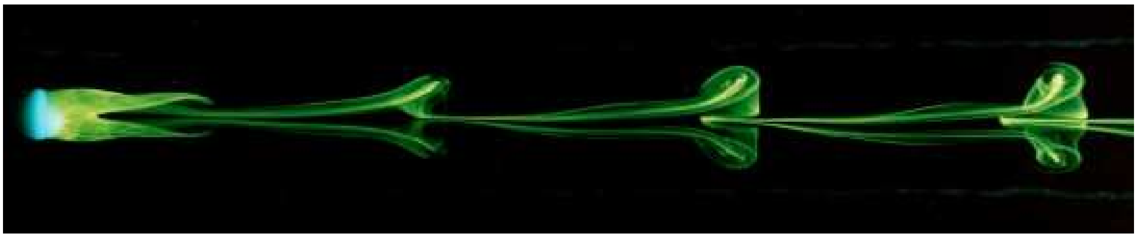

(a) Dye visualisation of the unsteady wake behind a sphere from Leweke *et al.* (1999) at $Re = 320$.

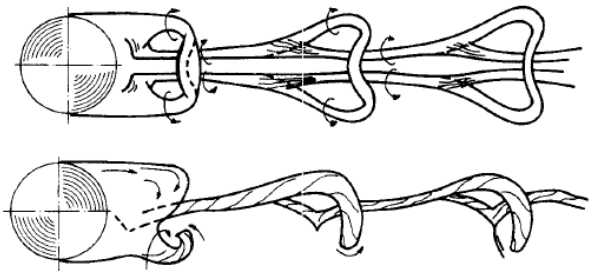

(b) Schematic of the flow structures observed by Achenbach (1975).

Figure 1.7: The unsteady wake behind a sphere.

Johnson & Patel (1999) explain the double-sided shedding as follows: While experimentally the shedding is generally observed to take place over one side of the body, resulting in a row of vortices with the same orientation, this flow pattern leads to difficulties in resolving the topology and circulation. Rather, numerical simulations indicate that the shedding taking place on one side of the sphere actually induces a weak hairpin vortex in the near wake on the opposite side of the body. These structures are remarkably similar to those detected in simulations by Mittal (1999), who observed vortex loops on both sides of the body in the near wake, one of which then rapidly dissipated as it moved downstream. As a result, there appears a single row of vortex loops of the same orientation, which then separate to form upright rings in the far wake. These simulations of Mittal (1999), given in figure 1.8, show perhaps more clearly than in other cases how the confusion between one and two-sided shedding may occur.

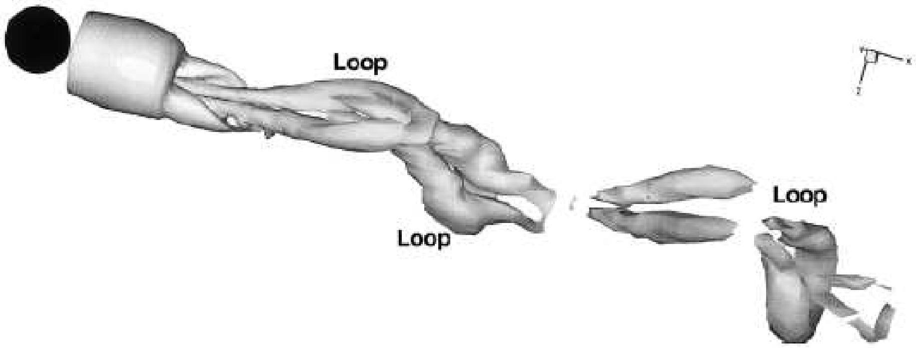

Figure 1.8: Results from Mittal (1999) showing the formation of vortex loops on opposite sides of the sphere wake at $Re = 350$.

According to Sakamoto & Haniu (1990), the regular, laminar shedding described above is present until $Re \approx 420$, at which point the shedding becomes more irregular and starts to oscillate from left to right. Mittal (1999) found that the separation points initially begin to shift at Re between 350 and 375. The change in the separation angle around the body is only small until $Re = 425$, at which point the variation increases dramatically. Hence, small scale variations may not be visible at lower Reynolds numbers in experimental flows. The shedding bias in this irregular regime was studied by Mittal *et al.* (2002), who found that the shedding was not completely random and a preferred orientation does exist but with significant variations each cycle. This irregularity increases with Re. They also found that the irregular shedding is possibly the result of two incommensurate frequencies in the wake. When $Re > 800$, the wake is no longer laminar and the orientation of the shed vortices shifts irregularly around the body (Sakamoto & Haniu 1990, 1995).

During regular laminar shedding, Magarvey & Bishop (1961a) observe a nearly linear increase of St with Re up to 400. These results were for the freely-falling sphere, as mentioned above, and may yield slightly different values for St and the forces on the body due to the sphere's dynamic response to the fluid forces. This dynamic response is not possible for the rigidly fixed sphere placed in a wind or water tunnel. In addition, Johnson & Patel (1999) found that the experimentally determined values of St tend to be slightly higher than the numerical values.

1.2.2 Flow past a rotating sphere

The first study of the motion of a spinning sphere was that undertaken by Robins in 1742, whose studies of ballistics were the first to report the deflection of muscat balls in air after they had been fired. In honour of this work, the Magnus effect, described previously, is also sometimes referred to as the Magnus-Robins effect. The present section deals specifically with the limited number of papers focusing on this type of motion, in which the axis of rotation is transverse to the freestream flow and the sphere is positioned far from any walls. The rotational motion which is induced via wall effects shall be considered later.

Effect of rotation on the flow

When a rotation is introduced to the sphere in a freestream, there exist several similarities to the flow around a rotating cylinder. As for the case of the rotating cylinder, Salem & Oesterle (1998) found that when the sphere was rotating with $-2 < \alpha < 2$, in a flow of Re up to 10, there existed only a single stagnation point in the symmetry plane, which was displaced from the sphere surface by a thin rotating fluid layer. In addition, the recirculation eddy that is observed by streamlines in the mid-plane of the rotation axis at low Re may be suppressed by the body rotation if the rotation rate is large enough (Salem & Oesterle 1998; Niazmand & Renksizbulut 2003). This is shown in the results of Niazmand & Renksizbulut (2003) below (figure 1.9). It must be noted that, although the eddy has been suppressed in the plane transverse to the axis of rotation, the plane in-line with the rotation axis clearly shows the formation of two recirculation zones.

Nakagawa *et al.* (2006) describe qualitatively the wake structures that form around the sphere surface at either end of the rotational axis. They find that the sphere rotation creates a low pressure region where the rotational velocity is in the same direction as the freestream. In contrast, the opposite half of the sphere develops a high pressure region where the rotation opposes the freestream. This pressure difference induces a ‘climbing’ flow from the high pressure to low pressure zones, on either side of the sphere at the cross-stream spin axis. When combined with the sphere rotation, these climbing flows form a counter-rotating, streamwise vortex pair, originating at the sides of the sphere, similar to the two-tailed wake that originates behind the non-rotating sphere.

At $Re = 200$, when the non-rotating sphere shows steady axi-symmetric flow, sim-

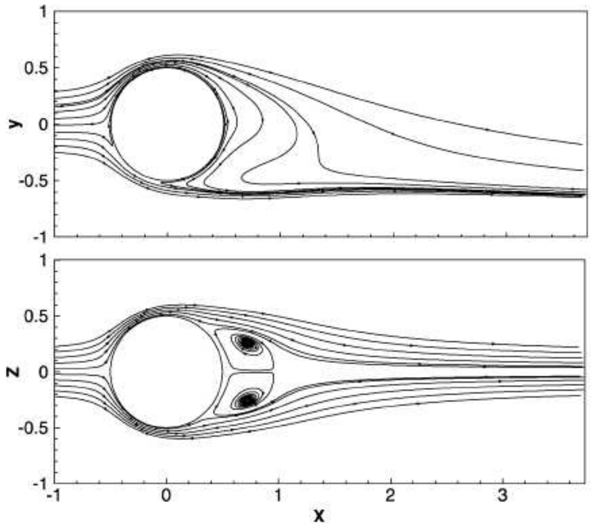

FIGURE 1.9: Streamlines showing loss of axi-symmetry in the wake when the sphere is rotating with $\alpha = 0.25$ at $Re = 100$ (from Niazmand & Renksizbulut (2003)).

ulations by Niazmand & Renksizbulut (2003) have detected unsteady flow behind the rotating sphere for $\alpha > 0.5$. This implies that the rotation, if of sufficiently large magnitude, can bring about the transition to unsteady flow at a lower critical Re. Furthermore, they find that the frequency of shedding increases with increasing α for a given Re in the moderate Reynolds number range. The amplitudes of the fluctuating lift and drag forces also show a significant increase with increasing α, as do the mean values (Niazmand & Renksizbulut 2003).

Rotation effects on the lift and drag forces

Based on the Stokes and Oseen approximations, Rubinow & Keller (1961) have derived expressions for the forces experienced by the sphere at very low Reynolds number ($Re \ll 1$). They found that at these Reynolds numbers, the lift followed the relation $C_L = 2\alpha(1 + O(Re))$. In comparison, Oesterlé & Dinh (1998) carried out experiments for $1 < \alpha < 6$ and $10 < Re < 140$ and obtained the fit $C_L \approx 0.45 + (2\alpha - 0.45)\exp(-0.075\alpha^{0.4}Re^{0.7})$ for the coefficient of lift in this range of Re. Their experiments were conducted using an indirect method to measure the deflection of a moving particle with known rotation. In their conclusion, they stated that they could offer no detailed explanation for the behaviour of C_L, given in terms of α and Re, as they lacked a knowledge of the flow structures around the sphere. For this reason, they proposed the use of numerical simulations to provide further insight into the problem

For a given $0 < \alpha < 0.25$, Kurose & Komori (1999) find that the lift coefficient tends to approach a constant value for $Re > 200$. The asymptotic value of the lift increases with α (Kurose & Komori 1999; Niazmand & Renksizbulut 2003). St also shows an increasing trend with Re but the values are shifted up for increasing α (Kurose & Komori 1999). Niazmand & Renksizbulut (2003) have studied the effect of sphere rotation in a uniform flow for Re up to 300 and $0 < \alpha < 1$. They find the relationship $C_L = 0.11(1 + \alpha)^{3.6}$ applies for the lift coefficient and that as the rotation rate increases, the ratio of lift to drag forces increases accordingly. This results in the lift force becoming comparable to the drag force.

The work by Rubinow & Keller (1961) for $Re < 1$ determined that the drag is independent of α at very low Reynolds numbers. At moderate Re, Kurose & Komori (1999) found that the drag force on a rotating sphere increases slightly when the rotation rate is increased and this effect is more noticeable at $Re > 200$. This was similar to the findings of Niazmand & Renksizbulut (2003), who observed a continuous increase in C_D with $\alpha \to 1$ at moderate Re. The increase in drag observed for increasing values of α is a reflection of the fact that the pressure component of the drag has increased, unlike the friction drag, which maintains a lower value and remains largely unchanged (Niazmand & Renksizbulut 2003).

1.2.3 Flow past a sphere near a wall

It is arguably the case that the most substantial work on the rotating/near-wall sphere has been undertaken in the creeping flow regime, where it is possible to derive a set of analytic equations (Goldman *et al.* 1967b; Malysa & van der Ven 1986). Such creeping flow solutions neglect the inertial effects of the flow, which make it impossible (due to the reversibility constraints of creeping flow) to obtain information relating to the transverse movement of the sphere, which is an inertial effect (Goldman *et al.* 1967a).

Even when these models have been modified to take into account the effect of fluid inertia, the values of Re under consideration have tended to remain small (Vasseur & Cox 1977; Cox & Hsu 1977; Ambari *et al.* 1984; Cherukat & McLaughlin 1990; Cherukat & McLaughlin 1994). Such modifications to existing models are typically carried out using the Oseen approximation to add an inertial correction, or by using the method of matched asymptotic expansions. The latter method defines two separate regions, an inner one near the sphere, where viscous forces dominate and a second one away from the body in which both inertial and viscous effects are considered. However, these types of models may still only be accurately applied at low Re. The only investigation to examine the free-rotation of a wall-mounted sphere at higher Re was that by Zeng *et al.* (2005). They carried out simulations for the flow around a translating and rotating sphere for Re up to 300. The sphere was positioned at different distances to the wall. The smallest of these distances was equal to a gap ratio of 0.25.

Wall-induced motion

In several studies, the sphere has been permitted a free rotation due to the flow-induced torque (Cox & Hsu 1977; Malysa & van der Ven 1986; Cherukat & McLaughlin 1994; Zeng *et al.* 2005). In general, for the sphere moving adjacent to a plane wall, any observed rotation has been in the positive (normal) direction and of relatively low magnitude. Experiments by Cherukat & McLaughlin (1990) detected no rotation of the sphere for gaps down to $0.5D$. Rotation was only observed when the spheres touched the wall and it seemed that the spheres rolled down the surface with no motion away from the wall due to the lift force. Zeng *et al.* (2005) allowed free-rotation of the sphere in their three-dimensional simulations at moderate Re and they observed small rates of normal rotation, which aided the flow through the gap region. Perhaps surprisingly, many of the results of Zeng *et al.* (2005) for Re up to 100 are in quite good agreement with the much lower Re theory mentioned above. The small effect of rotation on the drag was consistent with the low Re findings of Cox & Hsu (1977) and Cherukat & McLaughlin (1994). Furthermore, the lift coefficients up to $Re = 100$ agree well with those of Takemura & Magnaudet (2003). Overall, Zeng *et al.* (2005) found the effect of free-rotation on the lift and drag forces to be small. However, near the wall the drag coefficient is increased above that for an unbounded uniform flow.

In their experimental investigation of the translation and rotation for a sphere various distances from a wall, Malysa & van der Ven (1986) observed small rates of rotation in the normally rolling direction, for the sphere approaching the wall ($G/D < 0.5$). However, in this case no comment was made on the possible transverse motion of the sphere and no cavitation was detected at the smallest gap of $20\mu m$. The largest value of α detected was approximately 0.10 at the smallest gap ratio of 0.01.

In contrast, Cox & Hsu (1977) predicted motions of the sphere both towards and away from the wall in creeping shear flows modeled with an inertial correction. The direction of predicted motion (and hence, the lift force) in their model was dependent on the particle buoyancy, wall distance and the shear rate. When the flow is uniform, theoretical and experimental studies have found that the sphere sedimenting near a vertical plane wall in a Newtonian fluid will always migrate away from the wall (Vasseur & Cox 1977; Cherukat & McLaughlin 1990; Liu *et al.* 1993; Becker *et al.* 1996).

In fluids with non-Newtonian properties and for spheres in a strong shear flow or between nearby walls, the accelerating fluid away from the wall can bring about a reversed rotation of the sphere. This type of rotation is shown in figure 1.10, with the sphere translating down the wall but rotating as if rolling upwards.

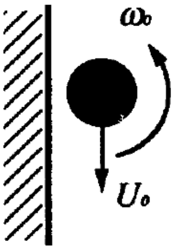

FIGURE 1.10: Anomalous rolling of a sphere as observed by Liu *et al.* (1993) for a sphere sedimenting in a channel.

Such reversed rotation is observed for sedimenting spheres in vertical tubes. Humphrey & Murata (1992) found that no-slip contact rolling only occurred for large spheres in a narrow tube when the inclination angle was less than 10° to the horizontal. In all other cases, there was a relative motion between the sphere and the tube and there existed a thin layer of fluid between the two. This type of lubrication layer will be discussed in the following section. For small tube inclination angles, the rotation of the sphere was reversed and the motion was dominated by the shearing action of the fluid. The same trends were observed by Liu *et al.* (1993) for sedimenting spheres in a rectangular channel with larger aspect ratio and with different critical inclination angles. Liu *et al.* (1993) observed motions ranging from reversed rolling to sliding and no-slip forward rotation. This was also observed in their two-dimensional simulations, where a particle would rotate in the reversed sense and move away from the nearby wall. Again this was done with relatively small Reynolds numbers ($Re < 10$) and the reversed rolling in this case may be due to the wall effects present in the simulations, even though the opposing wall is positioned many diameters from the body.

Liu *et al.* (1993) concluded that spheres dropped down a vertical channel in a Newtonian fluid will undergo reversed rotation and move away from the wall, whereas spheres in a non-Newtonian fluid will move toward the wall. Becker *et al.* (1996) attribute the results of Liu *et al.* (1993) to the fact that the spheres were dropped down a narrow channel and the wall effects acted to create anomalous rolling of the sphere. Without such nearby wall effects, the sphere would rotate in the opposite sense, as for normal rolling. Becker *et al.* (1996) conducted experiments in a larger tank filled with Newtonian fluid and were unable to detect any rotation of the sphere near the wall that was above the level of experimental noise. This was not the case for fluids with non-Newtonian properties, which all displayed anomalous rolling, the rotation rate of which appeared to decrease in magnitude with decreasing gap ratio.

Effect on the flow structures

Flow structures occurring in the wake of a near-wall sphere are described by Zeng *et al.* (2005), who observed the formation of a double threaded wake. Prior to the formation of this double thread, the flow was already asymmetric due to the presence of the nearby wall. The transition to the double-threaded mode occurs at lower Re than for the regular bifurcation behind an isolated sphere at $Re \approx 212$ and the Re of transition depends on the wall distance. Following this change in the wake structure, a dramatic increase in the overall coefficient of lift is observed, which is dominated by the pressure rather than the viscous component. When unsteady flow commences, the shedding takes the form of hairpin vortices and loops, as for the single-sided shedding observed behind an isolated sphere. The asymmetry of the geometry fixes the plane of symmetry normal to the wall and the force resulting from the shedding is also in the wall-normal direction.

Zeng *et al.* (2005) identify that the proximity of the wall has two competing effects on the flow. The viscous effects act to delay the onset of unsteady flow, while the asymmetry produced in the wake can enhance it. This is reflected in the critical Re of transition. As the sphere moves near the wall, the Re of transition to unsteady flow decreases to values below that observed for the isolated sphere but always remains above 250. However, as the sphere moves from a gap ratio of 0.5 to 0.25, the critical Re rapidly increases to above 300.

1.3 Lubrication effects and cavitation

When bluff bodies such as the cylinder and sphere are moving through a fluid in contact with a wall, a thin lubrication layer can appear in the fluid near the contact region. Furthermore, the low pressure that forms in this contact region can drop below the vapour pressure of the fluid, leading to the development of cavitation bubbles in the flow. Other possible causes of cavitation bubbles in the lubrication layer are given by Prokunin (2007) to be due to the diffusion of dissolved air from the surrounding fluid or through the presence on an air bubble trapped in the contact region prior to body motion. The presence of these bubbles can affect the relative motion of the body and cause a slipping action that prevents normal rolling. Unsteady motion of the sphere may also occur due to cavitation effects, when the size of the cavitation bubble is changing over time (Prokunin 2007). The following is a brief summary of the observed effects of cavitation on the motions of cylinders and spheres moving along a wall.

Several of the investigations mentioned in previous sections relating to the motion of a sphere near a wall have incorporated lubrication theory into their models. Goldman *et al.* (1967a) derive the lubrication-type theory applicable for the sphere approaching a wall. In their study, they discuss the analytical and experimental issues associated with the sphere moving in contact with the wall. In particular, their comments relate to the high and low pressures on either side of the near contact point, and the possible appearance of cavitation immediately behind the body. From their model, they find that the sphere cannot be in physical contact with the wall and that it slips as it moves along the surface.

Having observed cavitation experimentally between the sphere and the wall, Prokunin (2004, 2007) also developed a theoretical model to describe the motions of a sphere with cavitation. He found that when the cavitation force pushing the sphere away from the wall is greater than the wall-normal particle weight, a contactless steady sphere motion may be observed. They predicted $\alpha \approx 0.2$ for wall inclinations of $30^\circ \rightarrow 80^\circ$ from the horizontal, which was in good agreement with experimental results. This was less than 30% of the value of α predicted when cavitation was not taken into account. The study by Ashmore *et al.* (2005) observed a similar trend in α when lubrication effects were present for a sphere moving along a wall at low Re. Although the range of α did reach a value of unity, indicating normal rolling when the weight force of the spherical particle was directed almost normal to the wall, the majority of results appeared to asymptote to $\alpha \approx 0.2$ for increasing wall angles. Further results by Seddon & Mullin (2008) with a sphere placed inside a rotating drum also found α values to lie between 0.2 and 0.25 when cavitation was present.

Seddon & Mullin (2006) observed a similar formation of cavitation bubbles in the contact region beneath a small cylinder on the inner wall of a rotating drum. The cavitation bubbles formed, leading to a reduction from $\alpha \approx 1$ to 0. These cavitation bubbles continue to grow in size, leading to an almost continuous row of bubbles along the contact line. It is believed that the presence of these bubbles blocks the bulk flow of fluid through the gap. This blockage causes the incoming flow to reverse direction and move around the outside of the cylinder. This fluid flow creates a moment on the body, causing the cylinder to rotate in the reversed sense.

1.4 Review summary and points of interest for the present study

From the literature, a summary of the flow transitions occurring around a cylinder in unbounded flow at moderate Reynolds numbers is presented in table 1.1. The Reynolds numbers that shall be considered in the present study range from 20 to 500, and this covers the range over which the unbounded cylinder flow varies from two-dimensional and steady to unsteady and three-dimensional. Table 1.1 gives an indication of the Reynolds numbers at which each of these transitions takes place. When considering the cylinder geometry, the flow undergoes a Hopf bifurcation prior to the onset of three-dimensional flow.

Flow transition	*Re*
2D separated flow	6
2D unsteady	46
3D mode *A*	180-194
3D mode *B*	230-260

TABLE 1.1: Critical Reynolds numbers and flow transitions around the cylinder in unbounded flow.

The first three-dimensional mode to be observed with increasing *Re* is Mode *A*, and this transition is hysteretic, with an instability has a wavelength of approximately $4D$. The mode *A* instability has been attributed to an elliptic instability that grows in the vortex cores (Leweke & Williamson 1998b; Thompson *et al.* 2001b). The mode *B* transition occurs at still higher Re and has a wavelength of $0.8D$ and is attributed to a hyperbolic instability in the braid shear layer (Leweke & Williamson 1998b). These instabilities have been detected behind stationary cylinders with a range of cross-sections, and behind the cylinder undergoing transverse oscillations (Ryan *et al.* 2005; Leontini *et al.* 2007).

When a body rotation is introduced, the two-dimensional unsteady flow may be suppressed, provided that the rotation rate is large enough. This suppression has been found to take place at approximately $\alpha = 2$ for $Re > 200$, although this value of the critical rotation rate may be lower for smaller Re (Chew *et al.* 1995; Mittal & Kumar 2003; Kang *et al.* 1999). The other major impact of the cylinder rotation is an increase in the lift force. This takes place via the Magnus-Robbins effect.

When a non-rotating cylinder is placed next to either a moving or fixed wall, the wall acts to stabilise the flow and the transition to unsteady flow is delayed compared to that for the cylinder in unbounded flow (Taneda 1965; Arnal *et al.* 1991; Lei *et al.* 1999). The effects of the wall are highly dependent on the separation distance between the cylinder and the wall, and the stabilising effects become much greater as $G/D \rightarrow 0$.

For the cylinder in an unbounded flow, the Strouhal number of the unsteady wake gradually increases with Reynolds number until $Re > 200$, when the curve flattens out at values of St near 0.2. However, the effect of cylinder rotation on the Strouhal has not been clearly determined, with some investigations finding an increase of St with increasing α, and others finding a decrease or negligible change (Van Atta 1997; Jaminet & Van Atta 1969; Barnes 2000; Mittal & Kumar 2003; Kang *et al.* 1999). The effect of the nearby wall is to cause a decrease in St when the gap ratio is less than $0.5D$. In this situation, the frequency of the wake becomes less sensitive to changes in Re (Huang & Sung 2007; Lei *et al.* 1999, 2000; Arnal *et al.* 1991).

The flow around a sphere in a freestream undergoes transitions as summarised in table 1.2. The flow starts out as steady and axisymmetric and the first major transition is a regular bifurcation to steady asymmetric flow. The wake then takes the form of two streamwise vortices that maintain a planar symmetry while being displaced to one side of the sphere. This is often referred to as the 'two-tailed' wake. Following the onset of unsteady flow, the sphere wake is made up of a series of vortex loops, or hairpins, that maintain a planar symmetry and are shed on one side of the fixed sphere.

As is the case for the cylinder, when a body rotation is imposed on the sphere, an

Flow transition	Re
Separated axisymmetric flow	20
Steady asymmetric	210
Unsteady	270

Table 1.2: Critical Reynolds numbers and flow transitions for the sphere in unbounded flow.

induced lift force is created. Furthermore, Nakagawa *et al.* (2006) describe the flow present behind the rotating sphere as qualitatively similar to the 'two-tailed' wake with the presence of two streamwise vortices that form near the sphere surface at the axis of rotation.

When the sphere is moving adjacent to a wall, as for sedimenting particles in a channel, it is possible for the fluid forces to create a net rotation of the sphere. For spheres in a confined channel or non-Newtonian fluid, this can result in rotations with $\alpha < 0$. However, forward rolling is more commonly observed in Newtonian fluids or when there is an interaction between the sphere and the wall.

In their study of the translating sphere near a wall, Zeng *et al.* (2005) found that the wall could suppress the shedding of hairpin vortices when it was sufficiently close. At gap ratios larger than the critical value for suppression, the vortex shedding took place in a manner similar to that behind the sphere in a freestream. When the wall was close enough to enforce a steady wake, the asymmetry of flow created a wake pattern reminiscent of the steady asymmetric sphere wake, with two streamwise vortices present.

For rolling or sliding bodies such as the cylinder and sphere described above, lubrication effects and cavitation may play a part. The formation of cavitation bubbles beneath the cylinder allow free motion of the body relative to the wall and this situation can cause the rotation rate to change from positive to negative through the effect of a flow-induced moment. Experimental studies of cavitation between a sphere and a wall have found that the rotation tends towards an intermediate rolling and sliding corresponding to $\alpha \approx 0.2$ (Prokunin 2007; Ashmore *et al.* 2005). These intermediate α may therefore have a greater relevance in flows where cavitation is frequently observed.

Chapter 2

Numerical method and resolution studies

The following chapter outlines the numerical techniques used throughout this investigation. The equations governing the flow are given in section 2.1 along with a description of the numerical method. This is followed by sections 2.1.4 and 2.1.5 that describe the numerical resolution studies for the cylinder and sphere respectively.

2.1 Numerical simulations

Simulations are carried out in the non-rotating frame attached to the cylinder/sphere centre and all results are presented with the flow moving from left to right. As the frame of reference is not accelerating, no additional terms need to be included in the governing equations. Instead, the influence of the moving frame is effected through modifications to the boundary conditions, as will be described later. For simplicity, the results are represented in non-dimensional form, with the relevant variables normalised by the body diameter, D, and the freestream velocity, U. Likewise, the time is non-dimensionalised according to $\tau = tU/D$.

2.1.1 Governing equations

The numerical scheme solves the viscous, incompressible Navier-Stokes equations. These comprise the equations governing momentum transfer,

$$\frac{\partial \mathbf{u}}{\partial t} = -(\mathbf{u} \cdot \nabla)\mathbf{u} - \frac{1}{\rho}\nabla P + \frac{1}{\rho}\nabla \cdot \mu \nabla \mathbf{u}, \tag{2.1}$$

and continuity,

$$\nabla \cdot \mathbf{u} = 0, \tag{2.2}$$

in the fluid flow. Equations 2.1 and 2.2 are given in vector form, where $\mathbf{u}(x, y, z, t) = (u, v, w)$ is the velocity vector, ρ the fluid density, P the scalar pressure field and μ is the dynamic viscosity. As the density is considered to be constant throughout this investigation, the equations can be re-defined in terms of the dynamic pressure $p = P/\rho$. Likewise, the dynamic viscosity can be combined with the pressure to form the kinematic viscosity, $\nu = \mu/\rho$.

Equation 2.1 gives the rate of change of momentum (per unit mass) of the fluid flow, with the left-hand side made up of terms (from left to right) describing the convection, pressure and the viscous diffusion. The non-linearity of the convection term gives rise to complications in the governing mathematics, which shall be discussed later. The continuity equation (2.2) follows from the assumed incompressibility of the fluid and the rules of mass conservation. These equations apply to Newtonian fluids, in which a linear relationship exists between the shear stress and strain. Consequently, only such incompressible, Newtonian fluids shall be considered in the present investigation.

2.1.2 Numerical scheme

The above equations 2.1-2.2 are discretised with the use of a spectral element scheme that incorporates time-splitting for the temporal discretisation. The following is a brief description of the numerical scheme that was employed in both two and three dimensions to model the flow about wall-mounted cylinders and spheres. This code has previously been used to obtain accurate solutions for the flow around cylinders (Thompson *et al.* 2001b; Ryan *et al.* 2005), spheres (Thompson *et al.* 2001a, 2006) and rings (Sheard *et al.* 2003b).

Two versions of the code exist with regard to the time integration: a semi-implicit method is used throughout the cylinder studies and a more complex version, capable of iterative time-stepping, is used in the sphere simulations. This latter version of the code allows a relaxation of the time-step constraints that are associated with this geometry (specifically the small elements near the gap region in the 3D space) and provides a more stable scheme.

Temporal Discretisation

In order to overcome the non-linearity inherent in equation 2.1, the temporal discretisation takes place via a fractional step method that was first developed for the spectral element method by Karniadakis *et al.* (1991). It consists of separating the Navier-

Stokes equations into convection, pressure and diffusion terms, and integrating these terms in three separate sub-steps.

The first sub-step in the code deals with the convection component of equation 2.1. From this non-linear term, an intermediate velocity is calculated at the nth iteration as follows-

$$\frac{\mathbf{u}^{*} - \mathbf{n}^{n}}{\Delta t} = -(\mathbf{u} \cdot \nabla)\mathbf{u}. \tag{2.3}$$

Due to the non-linearity, this equation is generally solved explicitly using a third order Adams-Bashforth scheme. However, the version of the code used with the three-dimensional sphere simulations instead employs an iterative predictor-corrector method to increase the stability of the scheme and allow a larger timestep. The very first iteration is obtained with the Adams-Bashforth method, as described above, but following this, all subsequent iterations take place via the semi-implicit, third order Adams-Moulton routine. This is done using estimates of the velocity from the previous iteration for the terms on the right-hand side. Details of these schemes can be found in Ferziger & Perić (2002).

The next sub-step is that which addresses the pressure term and an updated estimate for the velocity field is obtained by

$$\frac{\mathbf{u}^{**} - \mathbf{u}^{*}}{\Delta t} = -\nabla p^{*}. \tag{2.4}$$

It is necessary to treat equation 2.4 in two parts as both the velocity field and the pressure field must be integrated forward in time. An estimate of the pressure field, p^{*}, is obtained by taking the divergence of equation 2.4 and forcing the velocity field at the end of the step, $\mathbf{u}^{**}$, to obey the continuity relation of equation 2.2. Enforcing $\nabla \cdot \mathbf{u}^{**} = 0$ ensures that $\nabla \cdot \mathbf{u}^{n+1} = 0$ at the end of the complete timestep, provided that the field is divergence free at the start of the timestep. This process leads to Poisson's equation for the pressure,

$$\nabla^{2} p^{*} = \frac{1}{\Delta t} \nabla \cdot \mathbf{u}^{*}, \tag{2.5}$$

and equation 2.4 may now be solved directly.

The final step in the iteration is that dealing with the diffusion. The diffusion component is of the form

$$\frac{\mathbf{u}^{n+1} - \mathbf{u}^{**}}{\Delta t} = \nu \nabla^{2} \mathbf{u}, \tag{2.6}$$

and in order to maintain a reasonable timestep at low Reynolds number, this equation is solved implicitly using the Crank-Nicholson method. Both the pressure and diffusion sub-steps were identical in the two versions of the code. With this overall formulation, the errors typically associated with time-splitting techniques have been reduced and the method provides second-order time accuracy for the velocity field the two-dimensional mesh was translated along the geometric symmetry axis. As mentioned above the cross-stream boundary condition was defined to be periodic.

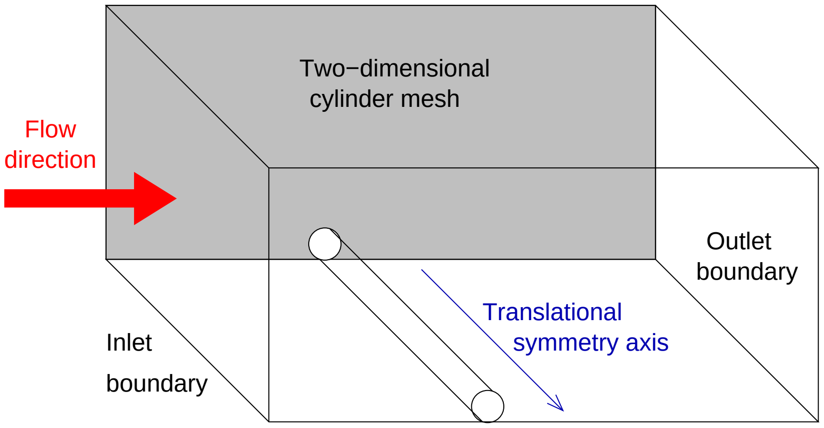

FIGURE 2.1: Schematic showing the two- and three-dimensional domains considered in simulations of the rolling and sliding cylinder.

Due to the location of the geometric symmetry axis in the sphere simulations (indicated in figure 2.2), it was not possible to define a separate outlet boundary. Instead, the same boundary of the two-dimensional mesh served as both inlet and outlet for the flow. Consequently, Dirichlet conditions were defined on all the exterior boundaries of the mesh to specify the velocity as being equal to the free-stream in both direction and magnitude. Details of the convergence studies for the boundary placement in each of these cases is given in sections 2.1.4 and 2.1.5.

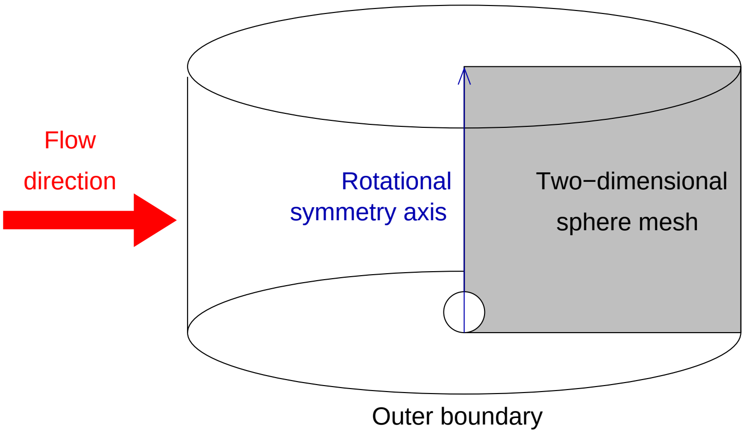

FIGURE 2.2: The three-dimensional domain created by rotating the sphere mesh around the symmetry axis.

2.1.3 Linear stability analysis

In order to examine the sensitivity of the flow to three-dimensional perturbations, a linear stability analysis was carried out. This is generally done by taking the two-dimensional base flow and adding a random perturbation in the third dimension, such that the new velocity and pressure terms become

$$\mathbf{u}(x, y, \tau) + \mathbf{u}'(x, y, z, \tau), \tag{2.7}$$

$$p(x, y, t) + p'(x, y, z, t), \tag{2.8}$$

where the primed variables indicate the perturbation components. At the boundaries of the domain the velocity and pressure perturbations are set to zero, except at a specified outflow condition, where equation **??** applies.

The above equations 2.7-2.8 are substituted into the Navier-Stokes equations, and the original, 2D base flow is subtracted. The resulting equations are then linearised, to give (in component form),

$$\frac{\partial u'}{\partial t} = -u\frac{\partial u'}{\partial x} - v\frac{\partial u'}{\partial y} - u'\frac{\partial u}{\partial x} - v'\frac{\partial u}{\partial y} - \frac{\partial p'}{\partial x} + \nu\left(\frac{\partial^2 u'}{\partial x^2} + \frac{\partial^2 u'}{\partial y^2} + \frac{\partial^2 u'}{\partial z^2}\right), \tag{2.9}$$

$$\frac{\partial v'}{\partial t} = -u\frac{\partial v'}{\partial x} - v\frac{\partial v'}{\partial y} - u'\frac{\partial v}{\partial x} - v'\frac{\partial v}{\partial y} - \frac{\partial p'}{\partial y} + \nu\left(\frac{\partial^2 v'}{\partial x^2} + \frac{\partial^2 v'}{\partial y^2} + \frac{\partial^2 v'}{\partial z^2}\right), \tag{2.10}$$

$$\frac{\partial w'}{\partial t} = -u\frac{\partial w'}{\partial x} - v\frac{\partial w'}{\partial y} - \frac{\partial p'}{\partial z} + \nu\left(\frac{\partial^2 w'}{\partial x^2} + \frac{\partial^2 w'}{\partial y^2} + \frac{\partial^2 w'}{\partial z^2}\right), \tag{2.11}$$

$$\frac{\partial u'}{\partial x} + \frac{\partial v'}{\partial y} + \frac{\partial w'}{\partial z} = 0, \tag{2.12}$$

which govern the perturbation field, the growth of which can then be monitored over time.

As the above set of partial differential equations is linear and has constant coefficients with respect to z, it is possible for the z dependent terms to be defined as the sum of complex exponential terms in a Fourier expansion. In fact, by taking perturbation variables of the form

$$u'(x, y, z, t) = \hat{u}(x, y, t)\sin(2\pi z/\lambda), \tag{2.13}$$

$$v'(x, y, z, t) = \hat{v}(x, y, t)\sin(2\pi z/\lambda), \tag{2.14}$$

$$w'(x, y, z, t) = \hat{w}(x, y, t)\cos(2\pi z/\lambda), \tag{2.15}$$

$$p'(x, y, z, t) = \hat{p}(x, y, t)\sin(2\pi z/\lambda), \tag{2.16}$$

the linearised equations (2.9-2.12) are satisfied and the perturbation in the z direction is specified in terms of the characteristic wavelength, λ. The general solution can then be constructed as a sum of these Fourier modes (see Barkley & Henderson (1996) for details).

The resulting equations, in terms of the new perturbation variables $\hat{u}$, $\hat{v}$,$\hat{w}$ and $\hat{p}$, which are now only dependent on two spatial variables, can be solved using the same techniques outlined in section 2.1.2. Hence, the growth of the perturbation in the z-direction, at a specified wavelength, λ, may be calculated.

Stability theory then considers solutions of the form,

$$\hat{r}(x, y, t+T) = \mathrm{e}^{\sigma T}\hat{r}(x, y, t), \tag{2.17}$$

where $\hat{r}$ is any of the perturbation fields $\hat{u}$, $\hat{v}$, $\hat{w}$ and $\hat{p}$, and T is a relevant period of time. This type of stability analysis may be carried out on either a steady or unsteady base flow. When unsteady periodic flow is considered, the process is termed Floquet analysis and T corresponds to a single period of the unsteady base flow. Taking into account the periodicity of such flows, equation 5.1 is commonly redefined in terms of the Floquet multiplier, $\mu = \mathrm{e}^{\sigma T}$. When a steady base flow is considered, T represents an arbitrary period over which the growth of the mode is recorded and this is typically in the order of one non-dimensional time unit. In the case of time-invariant flow, T is somewhat arbitrary, and the Floquet multiplier is therefore meaningless. In such cases the stability of the flow is generally referred to in terms of the growth rate, σ, of the mode.

In practice, the complex eigenvalue problem does not need to be set up and solved explicitly. Rather, the following procedure is used. The perturbation field is initialised with low amplitude white noise, which is then explicitly integrated forward in time. After each period of integration, T, the growth of the mode is assessed by taking the L_2 norm of any of the perturbation velocity components. The perturbation fields are then renormalised to unity by dividing by the value of the L_2 norm and the process of integration is repeated. After this process is repeated over many periods, only the fastest growing mode remains, and this is the one that will come to dominate the flow. Because of the renormalisation after each period, the L_2 norm itself is a measure of the growth in the magnitude of the perturbation field from one period to the next. In this way, the L_2 norm can be directly related to the value of the largest growth rate at the specified wavelength.

A positive value of the growth rate indicates that the mode will be amplified over time, while a negative value of σ implies that the mode will die out. For a specified λ, the Reynolds number at which $\sigma = 0$ is termed the critical Reynolds number as it indicates the value above which the flow will become locally unstable to three-dimensional perturbations and below which the flow will remain two-dimensional.

When dealing with a periodic base flow, three-dimensional instability modes are frequently observed that have a period equal to that of the base flow. However, this is not necessarily the case, and modes which have a frequency twice that of the base flow, or which are aperiodic, have also been detected. Aperiodic modes have a frequency which differs from the sampling frequency ($1/T$), and the Floquet multiplier comprises a complex conjugate pair. Such modes will be referred to from hereon as 'complex' modes.

With the power method employed throughout the present stability analysis, a perturbation mode which is either time-invariant, or with a frequency equal to the sampling frequency, T, will display a converged value for the Floquet multiplier. When the frequency of the mode differs to that at which the L_2 norm is calculated, the Floquet multiplier will appear to oscillate about a mean value over consecutive periods. Likewise, when dealing with the steady base flow, a steady three-dimensional mode that develops will display converged values of the 'Floquet' multiplier, but these will vary, depending on the value of T chosen.

Once a mode has been predicted to grow, its evolution in the real flow must eventually be non-linear, and hence, accurate information of the fully saturated mode cannot be obtained with the use of a linear stability analysis. This may apply also to the case of consecutive three-dimensional modes that develop with increasing Re. Once the three-dimensional flow resulting from the development and saturation of an initial 3D instability mode has evolved, the 2D base flow on which the perturbation analysis is based no longer applies. Therefore, further instability mode predictions based in the same 2D base flow lose their validity. In practice, however, higher order instability modes, or their analogues are often still observed (as in the circular cylinder wake (Henderson 1997; Williamson 1996a)).

Finally, due to the intrinsic three-dimensionality of the flow around the sphere, the analysis outlined above was only possible for the cylinder study, in which two-dimensional simulations could be used to develop the base flow.

2.1.4 Resolution studies for the cylinder

From two-dimensional cylinder simulations, the parameter space defined by $20 \leq Re \leq 500$ and $\alpha = -1$, -0.5, 0, 0.5 and 1 was investigated. From the simulations, the results for the lift and drag forces and St were reported. The sensitivity of these parameters to variations in the boundary placement, gap ratio and mesh resolution are shown in the following sections. The mesh used for the 2D cylinder study is given in figure 2.3 and increased resolution is present in the vicinity of the cylinder to capture the small-scale structures in the wake. There is also an increased resolution in the wake region for a distance of $30D$ downstream.

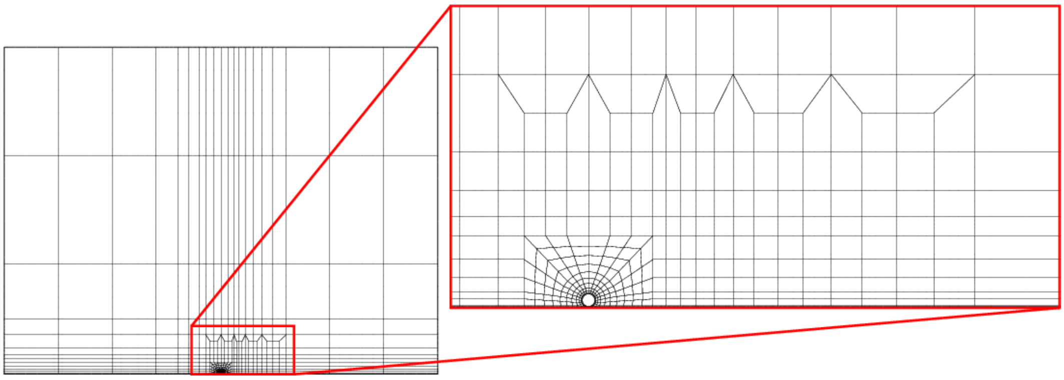

FIGURE 2.3: View of the cylinder mesh with detail of the region near the body.

In the present study, for $\alpha = 1$, 0.5 and 0, Reynolds numbers in the range $20 \leq Re \leq 200$, were suitable to capture the transition to unsteady flow. However, for $\alpha < 0$, the flow was more stable and it was necessary to increase the range of Re up to 500 in order to capture the unsteady transition. Resolution studies were therefore carried out at the extreme values of rotation rate ($\alpha = -1$ and 1) and Reynolds number ($Re = 20$, 200 and 500).

During the unsteady flow regime, the wake was considered to have reached the converged periodic solution when the variation in the peak lift was less than 1% over several cycles (in most cases this was less than 0.1%). The Strouhal number was then calculated from the frequency of the fluctuating lift coefficient.

The numerical code was tested to ensure that the solution was insensitive to variations in the chosen time step, Δt. This was found to be the case, where halving the timestep from 0.001 to 0.0005, for the Re and α given above, showed a variation in C_L, C_D and St of less than 0.1%.

Boundary resolution

The streamwise and transverse boundaries were placed far from the cylinder location to reduce blockage effects. The sensitivity of this boundary placement was tested using six different versions of the mesh, as shown in figure 2.4.

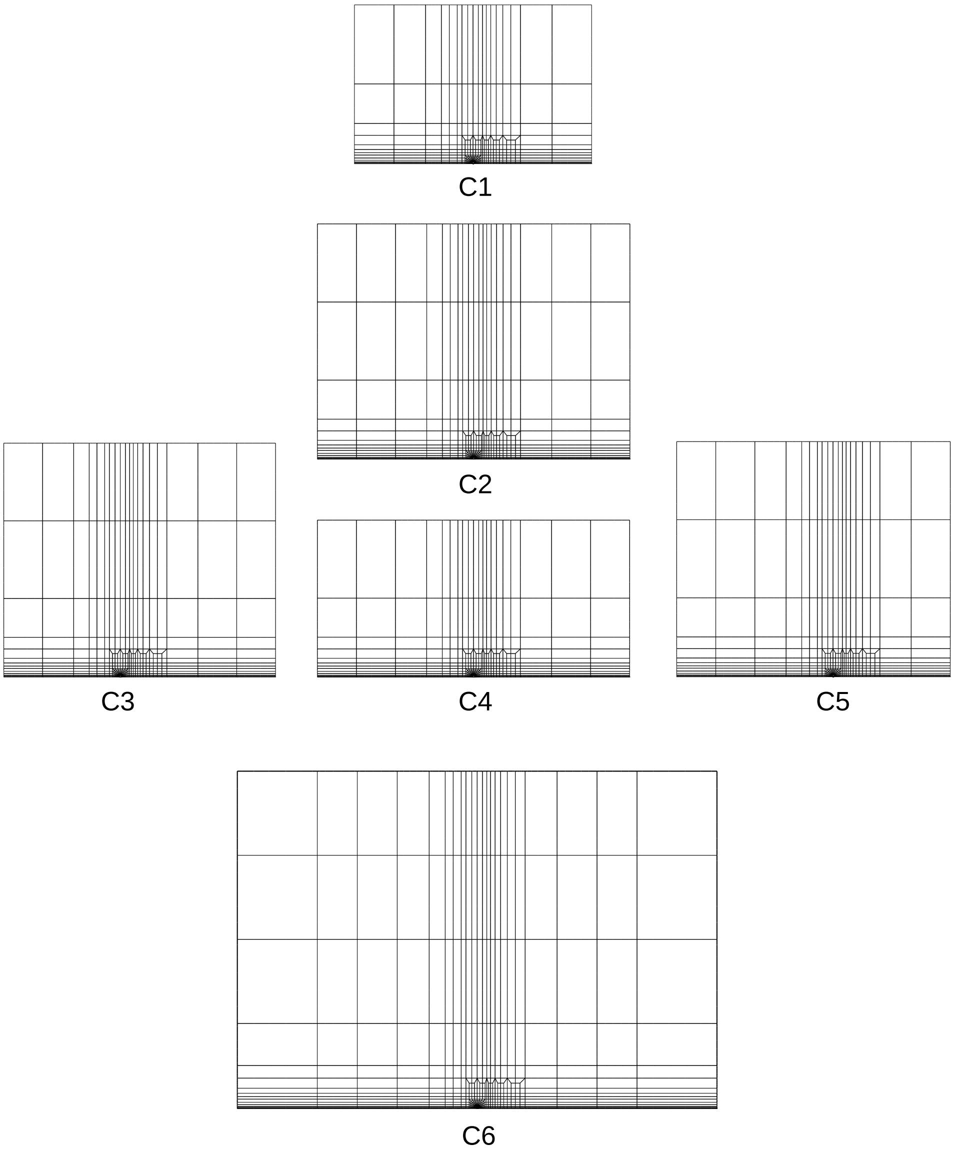

Figure 2.4: 2D cylinder meshes.

The number of macro elements, M, and the placement of the boundaries for each of the six meshes is given in table 2.1. The position of the upstream and downstream boundaries, are given by $x1$ and $x2$ respectively, while the position of the transverse boundary is given by $y1$. All boundary positions are non-dimensional and are given in terms of the cylinder diameter, D.

Mesh	M	$x1$	$x2$	$y1$
$C1$	516	-75	75	100
$C2$	562	-100	100	150
$C3$	548	-75	100	150
$C4$	542	-100	100	100
$C5$	548	-100	75	150
$C6$	612	-150	150	200

Table 2.1: Dimensions of the various meshes used to test domain size convergence.

The resolution studies for meshes $C1$, $C2$ and $C6$ are given in tables 2.2 and 2.3. These meshes were used to test the effect of enlarging the entire domain, while the meshes $C3-5$ were used to test the sensitivity of the solution to the placement of individual boundaries. While there is some variation in the values of C_L, C_D and St obtained with the different meshes, all values were found to be well within 1% of the value on the mesh with the largest boundary displacement. The greatest variation in both the magnitude and percentage of these values occurred in the higher Re range for $\alpha = 1$. For the unsteady flow at $Re = 200$, the Strouhal number varied by around 0.5%, although in this instance, the Strouhal number is of very low magnitude and the difference is in the 4th decimal place. The change in the relevant variables at $Re = 20$ was less than 0.1%.

	$Re = 20,\ \alpha = 1$		$Re = 20,\ \alpha = -1$	
Mesh	C_L	C_D	C_L	C_D
$C1$	2.3334	11.0364	5.1606	9.8756
$C2$	2.3330	11.0350	5.1602	9.8750
$C6$	2.3324	11.0340	5.1598	9.8750

Table 2.2: Boundary resolution for two-dimensional simulations of flow around the cylinder during low Reynolds number, steady flow.

The meshes $C3-5$ result from shortening specific boundaries of the $C2$ mesh. Of the upstream, downstream and transverse boundary placements, it appears to be the shortening the upstream length, $x1$, that causes the greatest variation in the lift and drag forces. By reducing the inflow domain length, the values of C_L and C_D increase to values similar to those for the smallest mesh, $C1$.

	$Re = 200,\ \alpha = 1$			$Re = 500,\ \alpha = -1$		
Mesh	St	$\bar{C_L}$	$\bar{C_D}$	St	$\bar{C_L}$	$\bar{C_D}$
$C1$	0.0530	1.1670	3.3216	0.1840	3.5392	0.8390
$C2$	0.0529	1.1660	3.3180	0.1839	3.5386	0.8383
$C6$	0.0528	1.1656	3.3172	0.1839	3.5380	0.8378

Table 2.3: Boundary resolution for two-dimensional simulations of flow around the cylinder for higher Reynolds number, unsteady flow.

Throughout the remainder of the investigation, results are obtained using mesh $C2$. This was considered to give adequately converged solutions and the differences between these and the larger mesh, $C6$, were calculated to be less than 0.1%.

Mesh resolution

As described in section 2.1.2, interpolants of order $N - 1$ are used to represent the solution variables during the spatial discretisation. This leads to a set of $N \times N$ internal node points within each macro-element of the mesh. The mesh resolution was varied by changing the order of these interpolants from 6 to 10. The results of this study are shown in table 2.4 for the higher Reynolds number flows at $\alpha = -1$ and 1.

The greatest difficulty in resolving the flow for the present study concerned the spatial resolution in the small gap region between the cylinder and the wall. If the order of the interpolant was too low, the flow in this region could not be resolved and at $Re = 500$, for $\alpha = -1$, the code diverged with $N = 6$.

	$Re = 200,\ \alpha = 1$			$Re = 500,\ \alpha = -1$		
N	St	$\bar{C_L}$	$\bar{C_D}$	St	$\bar{C_L}$	$\bar{C_D}$
6	0.0531	1.1692	3.3130	-	-	-
7	0.0530	1.1676	3.3200	0.1840	3.5390	0.8389
8	0.0529	1.1660	3.3180	0.1839	3.5386	0.8383
9	0.0529	1.1657	3.3192	0.1840	3.5382	0.8380
10	0.0529	1.1658	3.3228	0.1840	3.5382	0.8379

Table 2.4: Mesh resolution study for the two-dimensional simulations of flow around the cylinder.

In table 2.4, the values of St, C_L and C_D are all well within 1%, regardless of the value of N chosen. Here the selection of an appropriate N value relied rather on the range of N for which the solution did not diverge. A value of $N = 7$ was the minimum required to prevent divergence. Furthermore, for the lower Reynolds number limit of $Re = 20$, the values of the steady lift and drag coefficients remain identical to five significant figures for $N \geq 8$. This resulted in the selection of $N = 8$ for providing stable, converged solutions throughout the remainder of the simulations.

Note that the meshes are constructed to give increased resolution at the cylinder and sphere surface and near the wall. The parameters chosen to test resolution are also most sensitive to providing good resolution in the vicinity of the body. Further from the body the resolution is less, and for the higher Reynolds number cases, there can be some loss of resolution in the far wake region. This can be reflected by some graininess of the vortex structure as the vortices pass through the internal mesh boundaries. Nevertheless, further mesh resolution checks indicate that this does not affect the wake dynamics.

Gap resolution

As described earlier, it was necessary to impose a small gap between the body and the wall to avoid a collapsed mesh element at the wall. The gap was minimised as far as possible to accurately model the flow around a cylinder positioned in contact with the wall. Seven separate meshes were constructed with gap ratios of $G/D = 0.004$, 0.005, 0.006, 0.007, 0.008, 0.009 and 0.01. Due to numerical constraints the minimum gap ratio possible was $G/D = 0.004$. The sensitivity of the flow parameters over this range of gap ratio was then tested.

The variation of the lift and drag coefficients at $Re = 20$ are shown in figure 2.5. The lift shows a slight increase as the gap ratio is reduced for all values of α and the trend appears to be linear. The drag coefficient shows a clearly non-linear relationship and increases according to a power law as $G/D \rightarrow 0$. This increase in C_D was due to a substantial increase in the pressure force as the flow through the small gap was suppressed.

To confirm a power law relationship the data for C_D was replotted on a log-log scale in figure 2.6. The power law relationship of the replotted data is now clearly apparent, and the relationship between the drag coefficient and the gap ratio takes the form $C_D = a(G/D)^b$, where $a \approx 1.2$ and $b \approx -0.41$.

Assuming the trends for the lift shown in figure 2.9 to remain linear as $G/D \rightarrow 0$, the difference in magnitude of C_L between $G/D = 0.005$ and 0.01 should be approximately

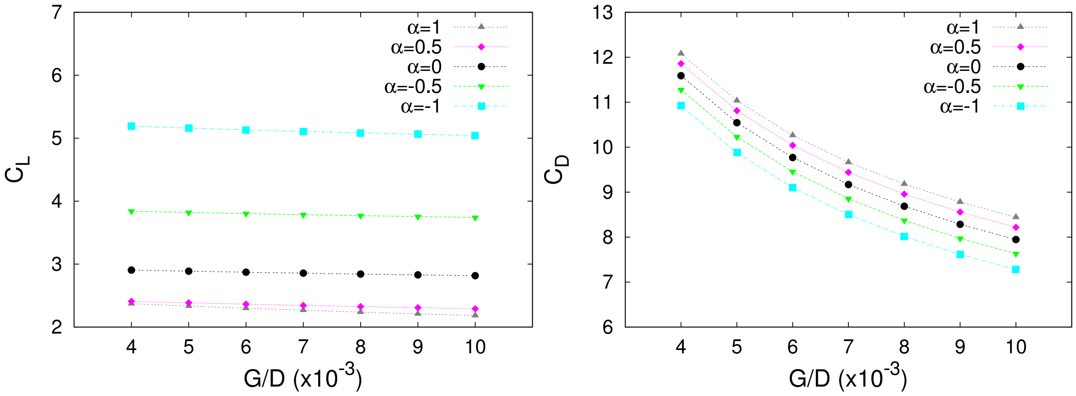

FIGURE 2.5: Variation in the lift and drag force with varying gap ratio at $Re = 20$.

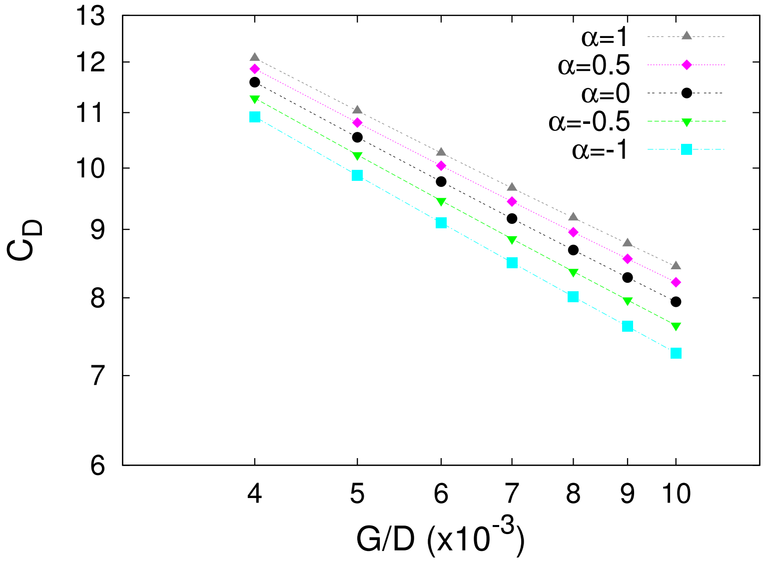

FIGURE 2.6: Logarithmic variation in the drag force with the gap ratio at $Re = 20$.

equal to the difference between C_L at $G/D = 0.005$ (hereby denoted $C_{L\ 0.005}$) and when the cylinder is touching the wall ($G/D = 0$). This variation has been expressed as a percentage error, $E(C_{L\ 0.005})$, in table 2.5.

The sensitivity of the drag forces to small variations in this gap distance was more pronounced at lower Reynolds numbers. Figure 2.7 shows the variation in the mean lift and drag of the unsteady flows at the upper Reynolds number limit for each α. At these higher Re, the variation in the drag force is less pronounced, however, there is still a nonlinear trend, especially for the results at $Re = 200$. As was done previously, these results were replotted on a log-log scale and appear to obey a power law relationship. The reduction in magnitude of the lift force at these higher Re means that the percentage difference as G/D is varied is larger. These predicted errors are given in table 2.6.

α	$E(C_{L\ 0.005})$
1	6.88%
0.5	3.99%
0	2.47%
-0.5	2.06%
-1	2.30%

TABLE 2.5: Percentage error in C_L at $Re = 20$ with $G/D = 0.005$.

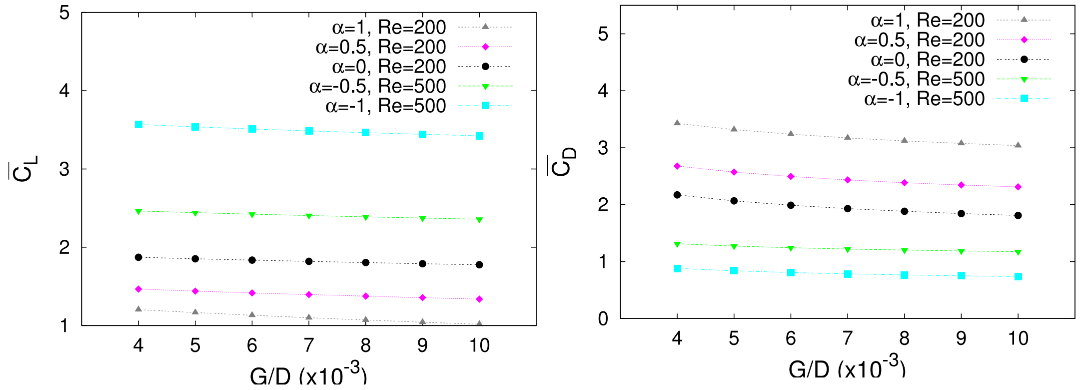

FIGURE 2.7: Variation in the lift and drag force with varying gap ratio at $Re = 200$ and 500.

During the unsteady flow regime, the variation in St with gap ratio was recorded and is shown below in figure 2.9. The Strouhal number trend was very linear and the predicted error in St with a gap ratio of $G/D = 0.005$, $(E(St_{\ 0.005}))$ is calculated as for the lift coefficient in table 2.5. The result is given in table 2.6. A negative error indicates a predicted decrease in St as $G/D \rightarrow 0$.

All simulations from this point forward are obtained with the mesh of gap ratio of 0.005. As mentioned above, the lower magnitude of C_L at higher Reynolds numbers has resulted in a larger percentage error in table 2.6. These values for $E(C_L)$ and $E(St)$ shall therefore be considered as an upper limit on the error of the lift force and wake frequency, obtained using the $G/D = 0.005$ mesh, as an approximation for the cylinder on the wall. Unfortunately, it is difficult to obtain an accurate error estimate for the drag as the relationships shown in Figs. 2.6 and 2.8 indicate that C_D diverges at $G/D \rightarrow 0$. Rather, although the magnitude of the force may vary, it is expected that the trends observed in C_D with varying Reynolds number and cylinder rotation rate will still hold. Likewise, when the flow visualisations are compared for the various gap ratios, the streamlines of the flow show no discernible difference and the flow structures are also assumed to be general.

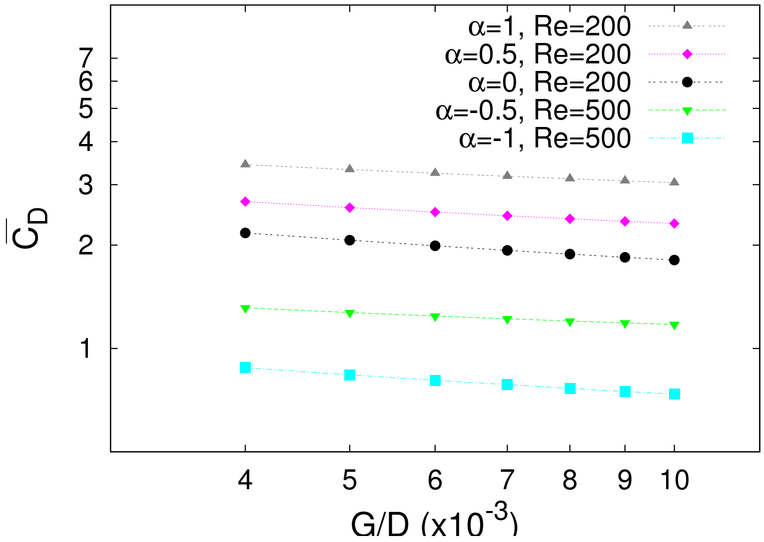

FIGURE 2.8: Logarithmic variation in the drag force with the gap ratio at $Re = 200$ and 500.

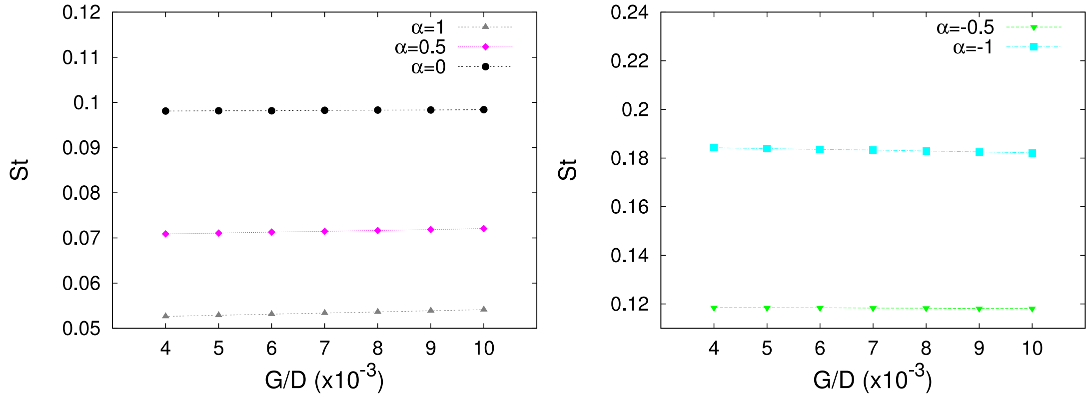

(a) $\alpha \geq 0$, $Re = 200$.

(b) $\alpha < 0$, $Re = 500$.

FIGURE 2.9: Variation in Strouhal number with varying gap ratio.

Three-dimensional simulations for the cylinder are used for qualitative comparisons with the experimental and two-dimensional numerical results. The three-dimensional expansion uses 36 Fourier planes in the spanwise direction spread over a distance of either one or four wavelengths of the dominant 3D instability mode for each α. Mesh $C2$ was also used for all the three-dimensional simulations and fifth order polynomials ($N = 6$) were used to solve for the relevant variables within each macro-element of the mesh.

2.1.5 Resolution studies for the sphere

Due to the setup and boundary conditions applied to the three-dimensional sphere domain, there was some difficulty in resolving magnitude of the forces acting on the sphere.

α	Re	$E(\bar{C}_{L\ 0.005})$	$E(St_{\ 0.005})$
1	200	12.8%	-2.37%
0.5	200	7.12%	-1.40%
0	200	4.14%	-0.30%
-0.5	500	3.45%	0.28%
-1	500	3.24%	1.14%

TABLE 2.6: Percentage error in St and C_L for with $G/D = 0.005$.

This was primarily due to fixing the velocity component on the external boundary, leading to a sensitivity of the lift and drag forces to the boundary placement. However, the structures present in the wake and the frequency of the unsteady mode proved to be largely insensitive to changes in the mesh parameters. Results for the sphere simulations are used for comparison with the experimental study and the frequency of vortex shedding was obtained both experimentally and numerically. Resolution studies showing convergence of the Strouhal number are given below.

The sphere mesh was created by adapting the right hand half of the cylinder mesh described in section 2.1.4. The sphere mesh is shown in figure 2.10, with the left hand boundary defined as the symmetry axis.

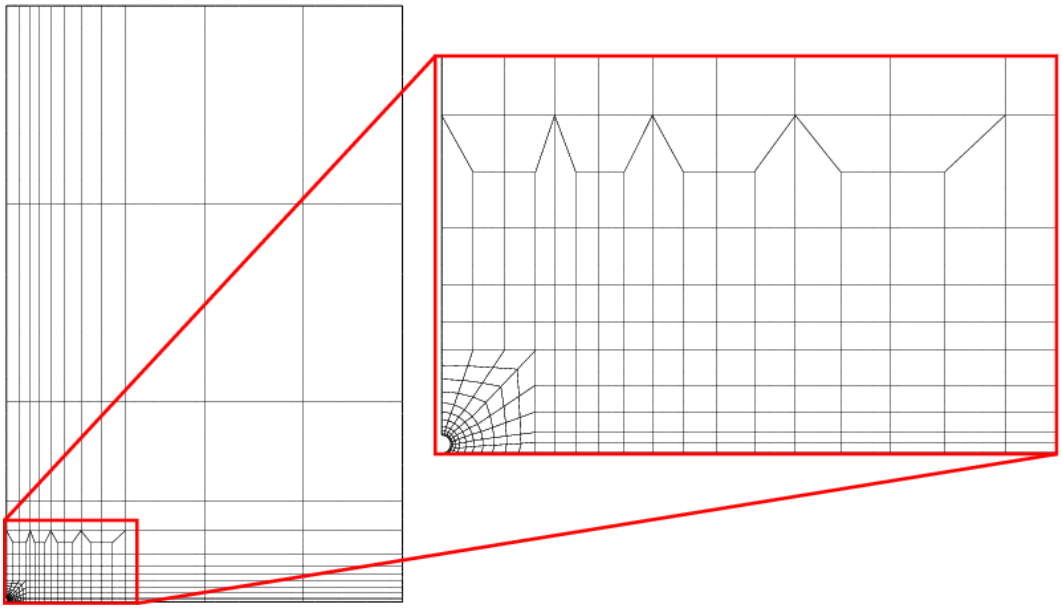

FIGURE 2.10: View of the sphere mesh with detail of the region near the body. The left hand boundary acts as the rotational symmetry axis.

Resolution studies are shown for the two extremes of the rotation rate, -1 and 1, and at the highest Reynolds number considered in each case. These were $Re = 200$

for the forward rolling sphere and $Re = 300$ for reversed rolling. A different unsteady wake mode was apparent in each case and the frequency of these two unsteady modes, were found to be independent of the chosen timestep. Values of Δt ranging from 0.001 to 0.0025 were tested and the variation of St in each case was less than 1%.

To accurately resolve the structures in the near wake of the sphere, the mesh of figure 2.10 was repeated with 128 Fourier planes around the symmetry axis. This created very small elements in the region near the central axis, and especially in the small gap region between the sphere and the wall. The resultant Courant condition leads to a restriction on the timestep and $\Delta t = 0.0025$ was selected as an appropriate upper limit. The use of $\Delta t = 0.001$ resulted in simulations of very long duration before the flow converged to a regular periodic state. This was found to be impractical and $\Delta t = 0.0025$ was used in all subsequent simulations.

Boundary resolution

To test the sensitivity of the sphere wake to the placement of the outer boundaries, three different meshes were constructed. The meshes, $S1$, $S2$ and $S3$ are shown in figure 2.11 and their corresponding dimensions are given in table 2.7. Here $x1$ and $y1$ are the distances from the sphere center to the outer and upper boundaries respectively and M is the number of macro-elements in each mesh.

Mesh	M	$x1$	$y1$
$S1$	296	75	100
$S2$	320	100	150
$S3$	346	150	200

Table 2.7: Dimensions of the three meshes used to test domain size convergence for the sphere.

The values of St obtained with each of the three sphere meshes are shown in table 2.8. The results from the smallest mesh displayed some sensitivity to the boundary placement with higher values of St for both extremes of sphere rotation. In addition, the boundary effects created larger velocities in the flow that restricted the maximum timestep to approximately 0.001. This made mesh $S1$ impractical to use for longer simulations. However, values of St measured with $S2$ and $S3$ were both within 0.5% and are therefore considered to provide values that are independent of the outer boundary placement.

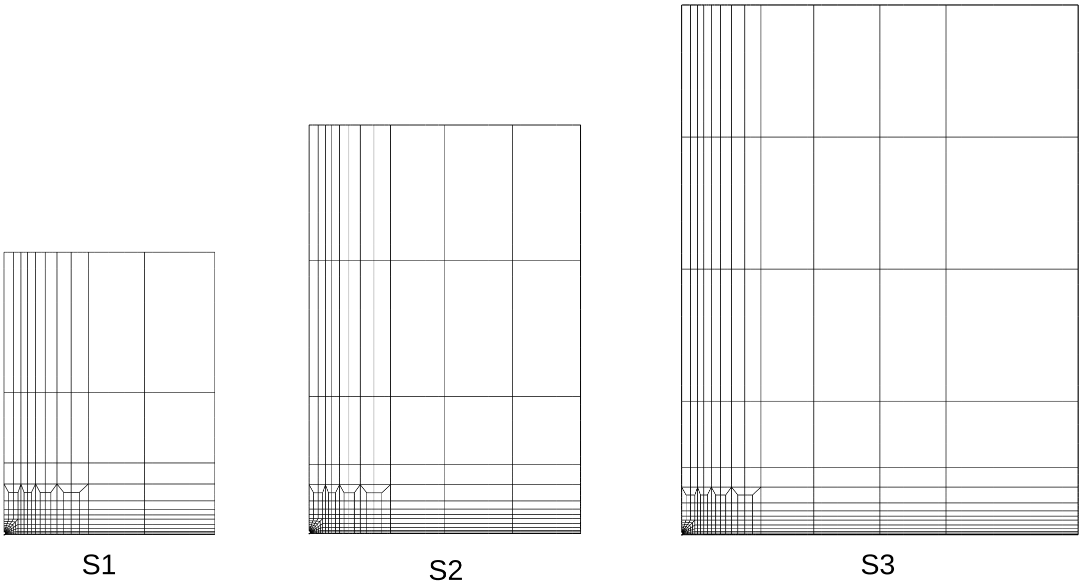

FIGURE 2.11: The three meshes used to test boundary resolution for the flow around the sphere.

	$Re = 200,\ \alpha = 1$	$Re = 300,\ \alpha = -1$
Mesh	St	St
$S1$	0.1139	0.1646
$S2$	0.1133	0.1646
$S3$	0.1134	0.1642

TABLE 2.8: Boundary resolution for three-dimensional simulations of unsteady flow around the sphere.

The difference in St values for $\alpha = 1$ and -1 in table 2.8 reflects the fact that two different wake modes occur. For $\alpha = 1$, a symmetric mode occurs and the Strouhal number is calculated from the lift-time history. For $\alpha = -1$ an antisymmetric mode is present that exerts a transverse force on the sphere. The wake frequency is therefore calculated from the cross-stream component of the forcing on the sphere. The form of these modes will be discussed in more detail in later sections.

Mesh resolution

To check for the convergence of the simulations with respect to the spatial resolution, the order of the interpolating polynomials was varied from third to fifth order. The polynomial order affected the timestep restriction of the simulations and therefore values of N less than 4 and greater than 6 were not considered as the timestep constraints became impractical. At the lowest spatial resolution tested ($N = 4$) the values of St was lower, and increasing the polynomial order showed a monotonic increase in St. For all three resolutions tested, the Strouhal number was within 1% and the spatial resolution was found to be sufficient. All future simulations were run with $N = 6$ as this provided the highest resolution with the greatest relaxation on the timestep.

	$Re = 200,\ \alpha = 1$	$Re = 300,\ \alpha = -1$
N	St	St
4	0.1131	0.1630
5	0.1133	0.1643
6	0.1133	0.1646

TABLE 2.9: Mesh resolution study for the three-dimensional simulations of flow around the sphere.

Gap resolution

The sensitivity of the sphere wake to variations in the gap ratio was tested on four different meshes and the results are shown in table 2.10. As for the case of the cylinder, reported above, the wake shows some sensitivity to small variations in the gap ratio. Interestingly, the frequency of the wake tends to increase slightly with G/D, for forward rolling and decrease slightly when the sphere is undergoing reversed rolling. In both cases the variation is monotonic for the gap ratios considered here.

	$Re = 200,\ \alpha = 1$	$Re = 300,\ \alpha = -1$
G/D	St	St
0.004	0.1131	0.1649
0.005	0.1133	0.1646
0.006	0.1138	0.1640
0.01	0.1160	0.1633

TABLE 2.10: Sensitivity of the Strouhal number to small variations in the gap ratio.

When the data in table 2.10 is extrapolated linearly to $G/D = 0$, the value of St at $G/D = 0.005$ is within 3% in each case. This is similar to the variation predicted for the cylinder. A gap ratio of $G/D = 0.005$ will be used throughout the remainder of this investigation.

2.2 Chapter summary

The numerical scheme used throughout this investigation is a spectral element method that has been previously applied to a variety of bluff body flows (Leontini *et al.* 2007; Thompson *et al.* 2006; Ryan *et al.* 2005; Thompson *et al.* 2001b; Sheard *et al.* 2003a). Versions of the program are available to carry out either two- or three-dimensional simulations and a tool for linear stability analysis of the flow is incorporated into the code.

The numerical method for simulating the flow around the rolling and sliding cylinder are described in both two and three dimensions and the technique of linear stability analysis is outlined. The sphere flow, which is inherently three-dimensional, is to be modeled with three-dimensional simulations that provide a comparison with the experimental work.

Convergence studies for the two dimensional simulations have been carried out with respect to the timestep, boundary placement, mesh resolution and gap ratio. At the chosen gap ratio of 0.005 the selected parameters were found to give converged results for the lift and drag force and the Strouhal number to within 1%. Small changes in the gap ratio give the greatest variation and the drag coefficient diverges according to a power law as $G/D \to 0$. Error estimates are presented for the lift coefficient at each rotation rate and the Strouhal number is found to be reasonably well approximated by the value of St at $G/D = 0.005$, with an estimated error of less than 3%.

Convergence studies for the Strouhal number of the unsteady sphere wake are presented. The convergence data is shown for the two extreme values of rotation rate (-1 and 1) at the upper limit of Re considered. These results are shown to be adequately resolved with respect to the timestep, boundary placement and mesh resolution, with the accuracy within 1%. As for the rolling cylinder, the sphere wake shows some variation in frequency with small changes in the gap ratio. The value of St at $G/D = 0.005$ is within 3% of the linearly approximated value at zero gap ratio.

Chapter 3

Experimental method

What follows is a description of the experimental setup including details of the construction and operation of the closed circuit water channel. The calibration techniques are outlined and velocity profiles in the empty channel are provided.

3.1 Experimental setup

The experimental setup was created through the modification of an existing closed cycle water channel. The closed test section measures $120W \times 140H \times 800L$ mm^3, and is equipped with a moving floor. Once the water levels have been appropriately set in the storage tanks, the channel operates via a gravity feed mechanism. This eliminates any flow perturbations that may be associated with a driving pump. This setup is capable of running at very low speeds (approximately 1 cm/s) and consequently, great care has been taken to ensure the uniformity of the flow and a low level of background turbulence.

The flow is governed by a twin tank arrangement, as shown in figure 3.1. When the water channel is in operation, the flow rate is controlled by a single centrifugal pump that draws water from a lower tank and discharges into an upper tank. From this second tank, the water passes through two regions of honeycomb, and a series of four fine mesh filters, before the flow enters a converging section. The two-tank arrangement of figure 3.1 means that the water could be moved into the lower storage tank via a gravity feed, leaving the test section empty for cleaning or maintenance.

The test section is closed but could be opened for cleaning or adjustment of the experimental setup by means of an access panel in the top surface. Having a closed test section allows the water level in the storage tank to be elevated above the top of the test section. This then permits the flow to enter the test section through a three-dimensional contraction, rather than the two-dimensional contraction frequently observed when a free-surface is present. In the present setup, the ratio of the contraction inlet to outlet area is 16:1. The three-dimensional contraction provides increased uniformity to the flow in the test section compared to the two-dimensional case.

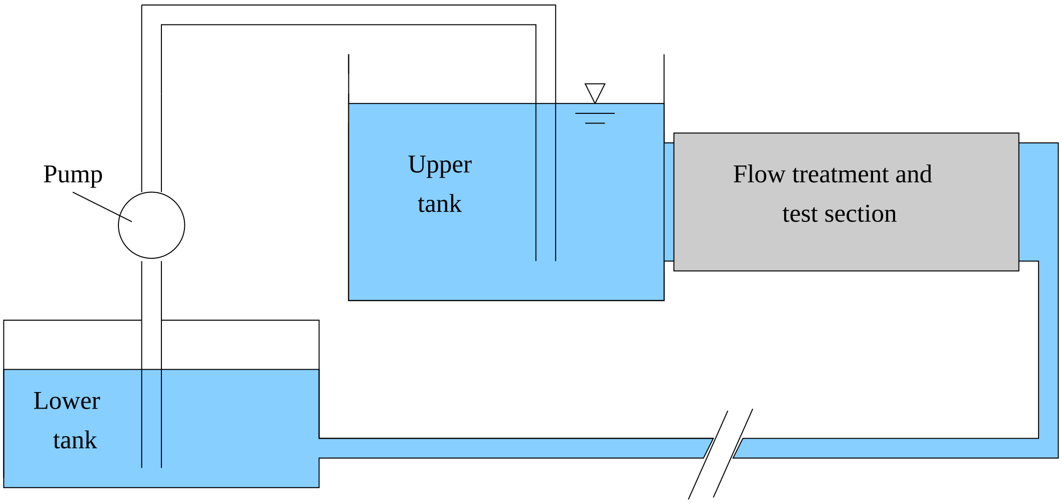

FIGURE 3.1: Upper and lower tank arrangement used to control flow in the water channel.

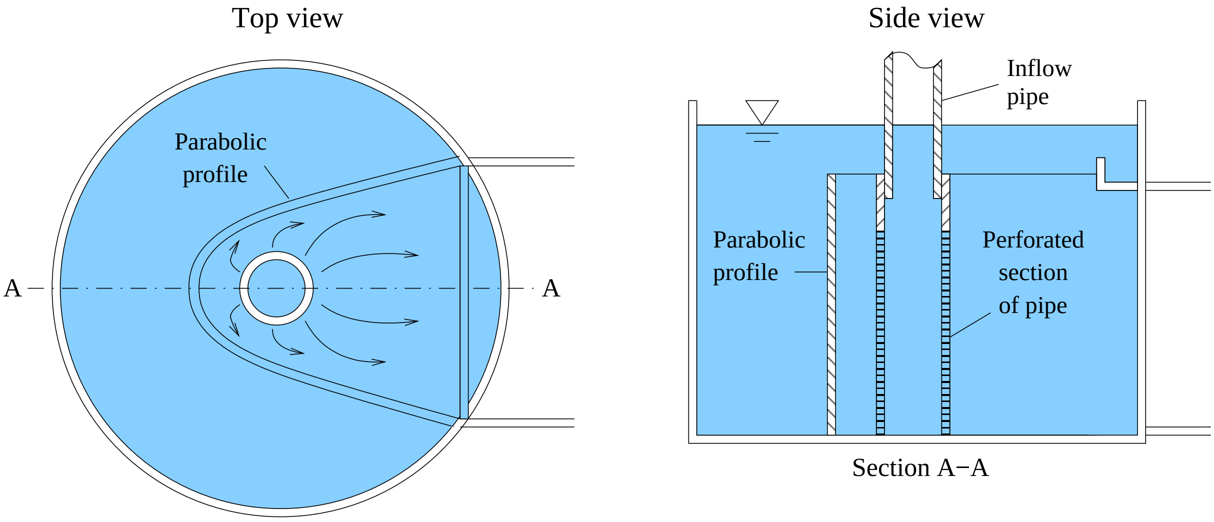

FIGURE 3.2: Top and side views of the upper storage tank with parabolic inflow geometry.

In addition to the honeycomb and filters mentioned above, several other measures have been taken to ensure the uniformity of the flow in the working section. The flow being pumped into the upper tank of figure 3.1 enters via a submerged section of perforated pipe that is fixed to a parabolic profile. This is shown from above and from the side in figure 3.2. The parabolic perspex profile is firmly fixed to the inlet of the working section to create a more uniform flow velocity in the cross-stream direction, while the perforated outlet pipe acts to create a more uniform flow in the vertical direction.

Details of the channel test section are shown in the schematic and photograph given in in figure 3.3, with the moving floor, boundary layer suction and dye injection points indicated on the photograph. The top and side walls of the test section are constructed of transparent perspex to allow visualisation of the flow from various angles and the side walls diverge at as angle of approximately 0.7° to the streamwise direction. This is to compensate for an increase in the speed of mid-channel flow due to a thickening of the fluid boundary layers on the top and side walls.

The angle of divergence of the side wall was calculated based on the boundary layer displacement thickness for laminar flow over a flat plate

$$\delta^* = \frac{1.72x}{\sqrt{Re}}, \tag{3.1}$$

where x is the streamwise distance along the plate. The growth of the boundary layer was considered over the length of the test section fitted with the moving floor and for a range of flow speeds. An angle was then selected to compensate for the average boundary layer growth on the fixed walls. As only the side walls are diverging, the angle is slightly higher than that predicted directly from the theory, to compensate for the boundary layer growth on the upper boundary. The divergence of the walls is set to optimise the channel operation when the freestream flow speed is from 1 to 3 cm/s.

Boundary layer suction takes place upstream of the moving floor, to remove the boundary layer that develops in the converging section of the upstream channel. A small centrifugal pump with constant flow capabilities is used to remove the boundary layer in the region outlined with blue in figure 3.3(b). The slot through which the boundary layer is removed measures $120W \times 10H$ mm and the volumetric flow rate of the fluid is calculated to give a mean velocity across this area that is equal to the freestream velocity. This fluid is then recirculated into the upper storage tank. The region enclosed in blue in figure 3.3(b) also incorporates a steel wool damper that assists in creating a uniform suction across the slot. Following the boundary layer suction, the freestream fluid passes over a perspex plate, approximately 75 mm in length, before reaching the region of the test section equipped with a moving floor.

The moving floor of the test section (shown in green in figure 3.3(b)) was independently calibrated to move at a velocity equal to the freestream. This configuration allows the sphere/cylinder position to be fixed, while the adjacent tunnel floor moves

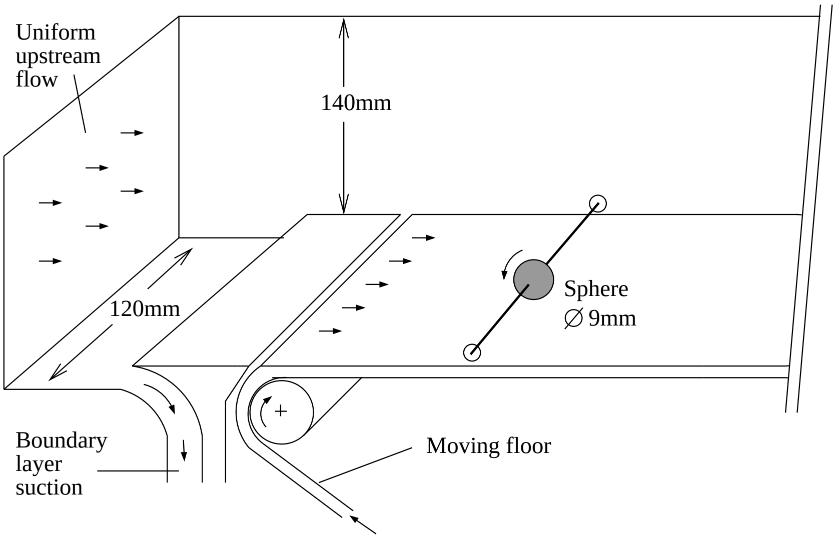

(a) Schematic of the start of the test section showing the sphere setup.

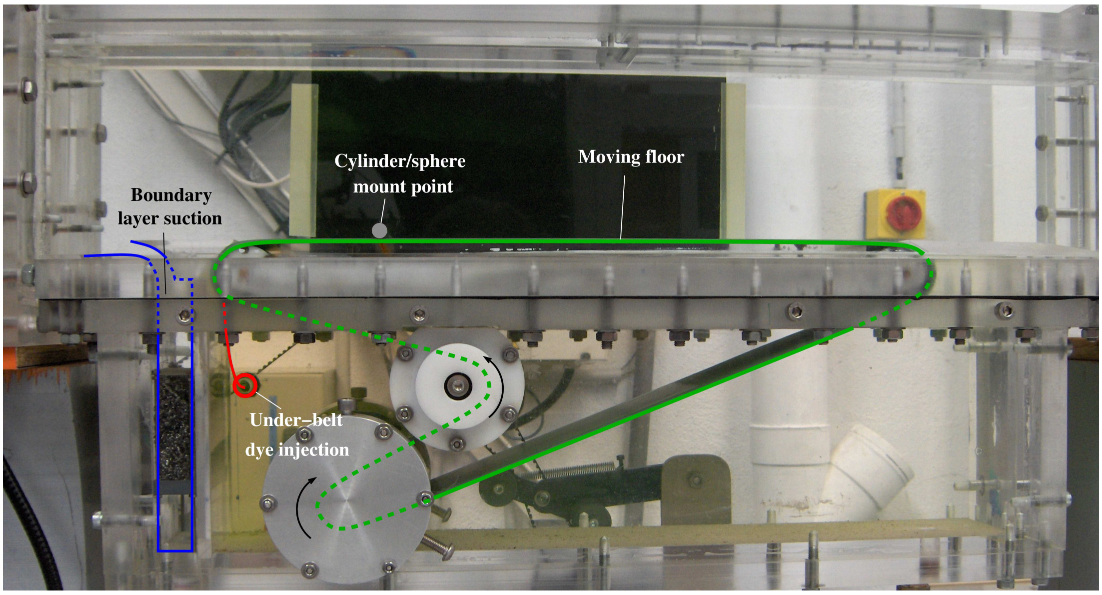

(b) Photograph of the entire test section, showing the moving floor, the boundary layer suction and the under-belt dye injection point

FIGURE 3.3: Schematic and photograph of the water channel test section.

past the body at the same velocity as the freestream flow. This is analogous to a body moving along a fixed wall at a constant velocity through a quiescent fluid when a change of reference frame is taken into consideration. The moving floor is represented by a seamless belt that spans the test section in the cross-stream direction, with an average displacement of 5 mm between the edge of the belt and the side walls. The moving floor begins near the upstream end of the test section following the boundary layer suction, and continues downstream for a distance of approximately 450 mm. In addition to rollers positioned at the start and finish of the moving floor, which act as guides, the belt passes around two separate rollers that are positioned below the test section. The lower of these two rollers (shown with a clockwise rotation in figure 3.3(b)) can be adjusted to tension the belt, while the upper roller (which rotates anticlockwise in figure 3.3(b)) is used to drive the belt motion.

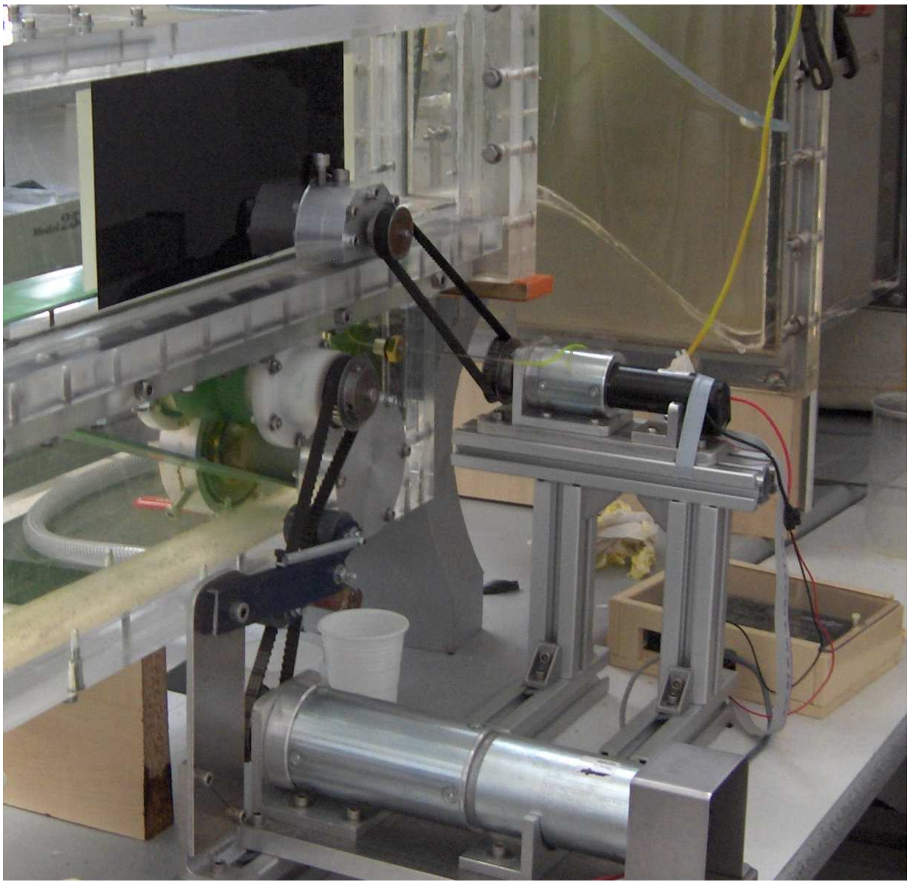

FIGURE 3.4: View from the back of the test section, showing the two motors that are used to drive the moving floor and the cylinder/sphere assembly.

The motion of the channel floor and the cylinder/sphere are controlled from one side by two separate stepper motors. These are located on the opposite side of the channel to the viewing area and are shown in figure 3.4. The smaller motor located near the middle of the image is connected to the cylinder/sphere assembly and both motors are independently computer controlled. The larger motor near the bottom of the image has a gear reduction of 20:1 and is used to drive the moving floor. This large gear ratio helps to increase the available torque and reduce vibrations that may propagate through the structure and affect the flow.

Velocity profiles in the empty channel are obtained with Laser-Doppler Anemometry (LDA), using hardware supplied by Dantec Dynamics. This technique was also used to calibrate the speed settings for the belt and cylinder/sphere rotation. When using the LDA setup, The empty tunnel flow is seeded with particles of 30 μm diameter and the velocity of the particles is recorded as they pass through the crossing point of two beams of a Yttrium Aluminium Garnet (YAG) laser with a wavelength of 532 nm. The signals recorded by the system are then analysed with Burst Spectrum Analyser (BSA) flow software (V3.00). One-dimensional velocity profiles are obtained in the test section with both the moving floor and active boundary layer suction, and these shall be presented in section 3.1.1.

A cylinder and a sphere of 9 mm diameter are mounted cross-stream, 100 mm downstream from the start of the moving floor. Images of these two geometries in the test section are shown in figure 3.5. The cylinder is machined from a steel rod and the sphere is manufactured from Teflon. The sphere is supported mid-stream by a metal supporting rod with a maximum diameter of 1.5 mm. Two variations of the supporting rod were used throughout this study. Initially, a supporting rod was constructed with a variable diameter along its length and a minimum diameter of 1 mm at the centre of the span. This provided a smaller diameter in the region near the sphere to minimse the effect on the flow, while increasing the diameter of the rod away from the sphere to improve the rigidity. However, this design required welding and any heat treatment had to be carried out with great care to avoid deforming the rod. Furthermore, the minimum diameter of 1 mm was found to be susceptible to bending if great care was not taken when installing the sphere in the test section. Consequently, this support was eventually replaced by a steel rod of fixed diameter 1.5 mm.

With the 1.5 mm diameter support, the rod/sphere diameter ratio is equal to 1:6. In the experimental study of the sphere, the typical Reynolds number range is from 20 to 300. At the top of this range, the Reynolds number associated with the supporting rod is approximately 50. This is just over the critical Reynolds number for vortex shedding from a stationary cylinder. While not ideal, this is a compromise between properly supporting the sphere and limiting the downstream wake interference. Furthermore, previous experimental studies of the isolated sphere in a free-stream, it has been found that the presence of similar supporting structures has negligible effect on the qualitative properties of the wake, when compared to the predicted numerical results (Schouveiler & Provansal 2002; Thompson *et al.* 2001a; Johnson & Patel 1999; Ghidersa & Dušek 2000). A comparison between numerical and experimental results is also reported in chapter 6 of the present investigation.

In the experimental setup, the vertical position of the body could be adjusted. Whenever possible, the cylinder and sphere are positioned in contact with the floor. For the cases of $\alpha = -0.5$ and -1, when the relative motions of body and floor are in opposite directions, a small gap (up to 5% of the diameter) is present. This distance is carefully minimised, but is still necessary to prevent the moving floor from interfering with the body motion, especially in the case of the sphere.

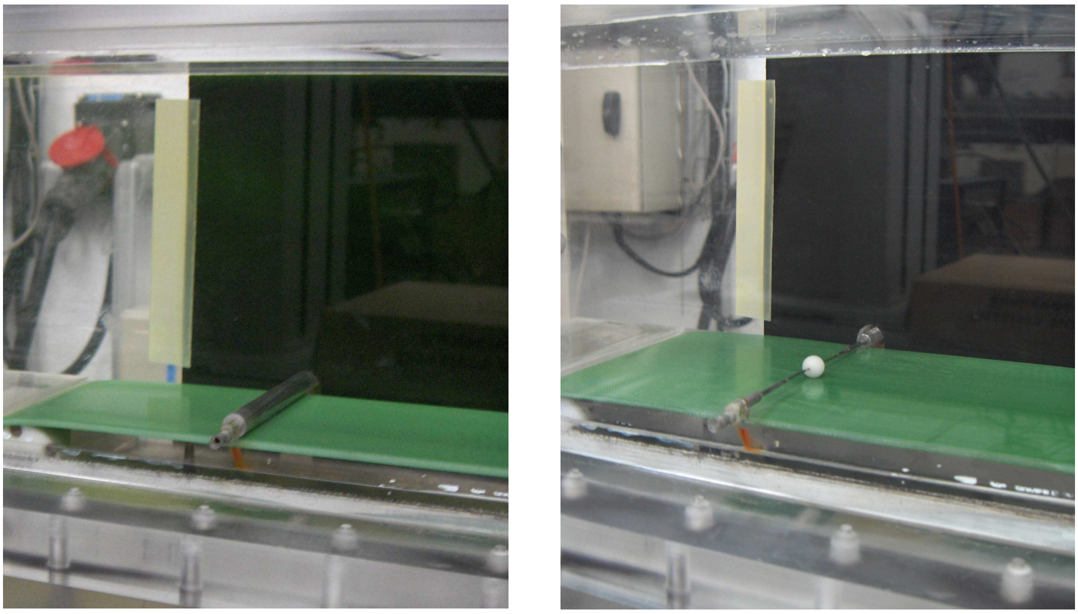

(a) Cylinder mounted in the test section.

(b) Sphere mounted in the test section.

FIGURE 3.5: Zoomed in view of the cylinder and sphere mounted in the test section. The sphere is shown here with the variable diameter support.

Flow visualisation in the water channel uses fluorescein dye, illuminated with the light from an Argon laser at 488 nm. Because of the range of body rotations to be tested, there is some difficulty in locating a single position for dye injection that is effective for all α. As a result, two positions were settled upon; one injects dye through a thin tube located in the upstream flow and the other introduces dye onto the surface of the moving belt. The latter is positioned beneath the belt assembly and is highlighted in red in figure 3.3(b). In this image, the dye is introduced via a thin tube that is inserted through the back wall of the channel below the belt. This tube then bends upwards and the dye outlet is located at a point just below the belt surface. The dye reservoir is stored at an elevated height above the test section to allow for a gravity feed mechanism. The thin dye film provides streaklines of the fluid flow that are coincident with the streamlines during the steady flow regimes. The relative density of the dye and the water are very close and the dye stream provides minimal disturbance to the fluid flow.

When the cylinder is installed in the test section, the injection point on the belt surface is used, regardless of the value of α. The dye is injected on the underside of the belt assembly as a thick band of dye (approximately 20 mm wide) at the centreline of the belt. This dye remains on the belt surface as it is carried up into the test section, upstream of the cylinder. Even when the cylinder is undergoing forward rotation, the blockage effect of the flow means that the dye is lifted off the belt surface and carried over the top of the cylinder, creating an image of the flow structures in the wake. This method is also effective for the sphere when $\alpha < 0$, as sphere rotation entrains a layer of dye from the belt and lifts it over the body and into the wake.

When the sphere setup is used with $\alpha \geq 0$, the relative motion of the sphere and the floor results in the dye on the moving floor not being lifted into the flow, but instead remains on the floor and passes around the sides of the sphere. Instead, the upstream dye injection point is required. In this case, the metal tube is located far upstream of the test section so as to not interfere with the flow. When using the injection point located in the free stream, great care is needed to position the dye stream such that it effectively coats the sphere.

The dye visualisation method described above allows qualitative and quantitative data to be obtained relating to the nature of the flow. Still images were taken from in front of and above the test section and movies of the unsteady flow are recorded from which it is possible to extract the dominant frequency of the wake. The light from the Argon laser is spread into either a thin sheet, for visualisation of flow in a plane, or into a thick sheet, which allows a volume to be visualised. As mentioned above, images of the flow may be recoded either from above, or from the side (such as in figure 3.3(b).

For calculation of the Reynolds number of the flow, the water viscosity and density were assumed to follow the functional fits given in White (1999),

$$\ln\left(\frac{\mu}{\mu_0}\right) = -1.704 - 5.306\left(\frac{273}{T_K}\right) + 7.003\left(\frac{273}{T_K}\right)^2, \qquad (3.2)$$

and

$$\rho = 1000 - 0.0178|T_K - 277|^{1.7}, \qquad (3.3)$$

where $\mu_0 = 1.788 \times 10^{-3}$ kg/(m·s), T_K is the measured temperature in Kelvin and ρ is calculated in kg/m^3. These equations apply for temperatures from 0 °C to 100 °C. The accuracy of equation 3.2 is given by White (1999) as ±1% and that for equation 3.3 is ±0.2%. The water temperature is measured prior to each experimental run and the thermometer is placed within the area of the parabolic profile in the upper tank. This is removed before measurements are taken so as not to disturb the inlet flow. The duration of the individual runs is such that the temperature variation during a single experiment is negligible.

3.1.1 Calibration and convergence tests

Once all the motors and pump speeds had been independently calibrated, they were connected to a series of electronic controllers with a software interface in Labview. Without the cylinder or sphere mounted in the test section, velocity profiles were obtained using the LDA technique mentioned in section 3.1, with both the moving floor and boundary layer suction in operation. Profiles are taken in the vertical centre-plane of the moving belt. The origin is located on the belt at the position where the cylinder or sphere shall be mounted. The x-axis is positive in the streamwise direction and the y-axis is perpendicular to the belt.

From figure 3.3, it can be seen that the boundary layer suction takes place upstream of the moving floor and following this, the flow passes over a solid section of perspex, approximately 75 mm in length, before reaching the section of the channel equipped with the moving floor. In this intermediate region, a thin boundary layer re-forms. This can be seen in the velocity profile of figure 3.6 at $x = -100$ mm, taken just ahead of the moving floor. As the flow moves downstream, the effect of the moving floor counteracts this velocity deficit and by $x = 0$ mm an almost uniform velocity profile is obtained.

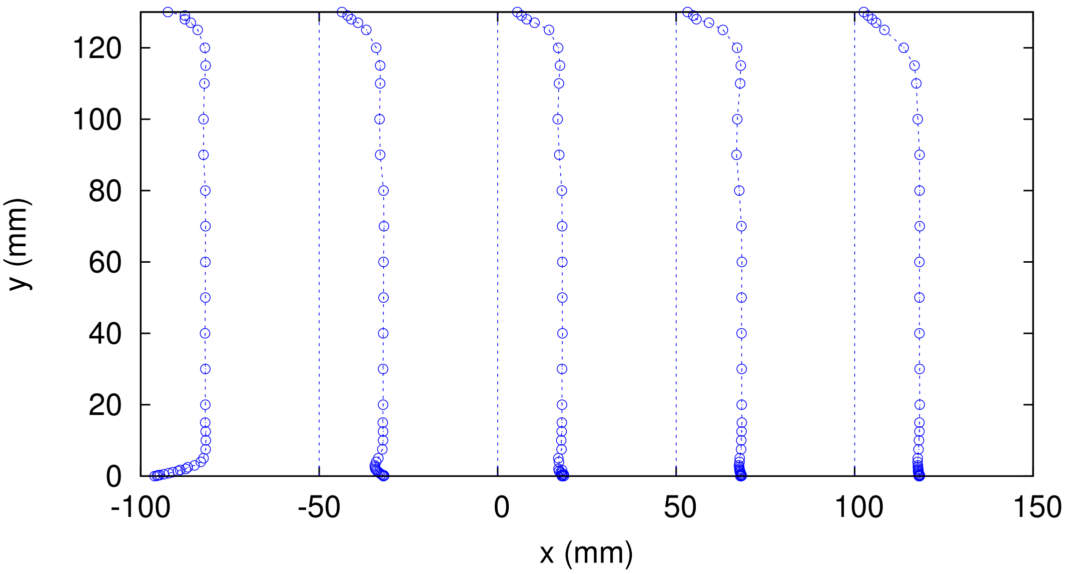

FIGURE 3.6: Velocity profiles measured along the centreline of the moving floor, upstream and downstream of the body position. The freestream velocity (as measured at x=0 mm and y=50 mm) is equal to 1.8 cm/s.

A point at (0 mm,50 mm) is used to measure the speed of the freestream. From figure 3.6, it can be seen that the velocity profile at this point is very uniform, with no disturbing effect from the boundary layer developing along the top surface. The velocity profiles given in figure 3.6 are shown at a characteristic freestream velocity of 1.8 cm/s. This corresponds to a Reynolds number, based on the 9 mm body diameter, of approximately 170. Any deficit present in the velocity profile that exists as a remnant of the boundary layer is less pronounced at lower freestream velocities.

As mentioned in section 3.1, the walls of the test section diverged slightly to counteract the effects of boundary layer growth on the top and side wall of the channel, resulting in an increase in the freestream flow speed mid-channel. Streamwise velocity profiles were used to check the effectiveness of the downstream divergence of the test section. The variation in the freestream velocity is measured along the axis $y = 50$ mm from $x = 0$ mm (the point at which the channel velocities were calibrated) to $x = 200$ mm. Over this distance the variation in the flow speed is less than 2.5%. This indicates that when the cylinder or sphere are mounted in the test section, there should be only a minor increase in the freestream speed, over a distance of more than $22D$, due to the thickening of the fluid boundary layers.

The parabolic profile described in section 3.1, in conjunction with the honeycomb and filter system, provided a background turbulence level ($U_{RMS}/\bar{U}$, defined as the root-mean-square velocity at a point in mid-stream, divided by the time-mean velocity at that point) of less than 1.5%. This value was obtained using the LDA equipment to measure the flow speeds at the reference point, (0 mm,50 mm), and represents an upper limit for the turbulence levels. Based on observations of the dye visualisation and the deformation of the structures over the length of the test section, it is expected that the true turbulence level in the water channel is not more than 1%.

The minimum Reynolds number achievable in the water channel with the 9 mm diameter cylinder and sphere is 75. The corresponding flow flow speed necessary for this *Re* is approximately 0.8 cm/s. This make experiments challenging, as natural convection in the flow begins to affect the results if the water temperature is not in almost perfect equilibrium with the ambient. The maximum *Re* possible was around 350 (corresponding to a freestream velocity of approximately 3.7 cm/s). This limit was imposed by the motor governing the motion of the belt. At higher flow speeds, the moving floor could not match the freestream velocity. Furthermore, the vortex shedding effects of the supporting rod in the sphere assembly become non-negligible at *Re* above approximately 300.

A smaller diameter cylinder was tested to further reduce the minimum Reynolds possible in the channel. However, it was decided that detailed flow visualisation becomes too difficult to obtain when the length scale is further reduced. Likewise, in the case of the sphere, the required diameter of the supporting rod made further reduction in the sphere diameter impractical.

3.2 Chapter summary

A description had been given of the closed cycle water channel, equipped with a moving floor and boundary layer suction. This is used to model the flow around a rolling or sliding body moving through a quiescent fluid. The channel construction incorporated a slight divergence in the walls of the working section, to compensate for an increase in U due to the development of boundary layers on the top and side walls. The boundary layer suction, which takes place just upstream of the test section, and motion of the floor are both set equal to the freestream velocity during operation.

Calibration of the water channel was carried out using an LDA setup to monitor the speed of the freestream, floor and body rotation. Following this, midstream profiles in the empty channel showed that the effect of the boundary layer has been almost completely removed at the streamwise location of the cylinder and sphere mounting.

During operation, the range of Reynolds numbers achievable in the channel was approximately 75 to 350. This corresponds to a range of experimental flow speeds between 0.8 and 3.5 cm/s. The range of Reynolds number coincides closely with the range chosen for experimental work and covers a range of major transitions observed in the wake behind cylinders and spheres in an unbounded flow. Experiments shall focus on the qualitative and quantitative information that can be obtained from the flow visualisations. Fluorescein dye is used to visualise the steady and unsteady structures in the wake, and these are recorded as both movies and still images.

Chapter 4

Two-dimensional flow around the cylinder

It is known that the flow around a cylinder in a freestream remains predominantly two-dimensional until $Re \approx 190$ when the mode A transition to three-dimensional flow takes place (Williamson 1996a; Barkley & Henderson 1996). Consequently, it makes sense to begin the investigation of the cylinder moving along a wall with the modeling of two-dimensional flow. Although the transition to three-dimensional flow in the present study does not necessarily take place in the same manner, or at the same Re as for the unbounded cylinder flow. It is expected that the flow remains two-dimensional in the lower Reynolds number range, however, this aspect of the flow shall be investigated further in section 5.

The following chapter presents results obtained from the two-dimensional numerical simulations of the flow. The steady-flow regime is discussed in some detail with reference to the recirculation zones that form behind the cylinder and how these are affected by the rotation rates of the cylinder. The trends in the lift and drag coefficients with changing rotation rate, α, are also discussed. Following this, the critical Reynolds number at which unsteady flow occurs is identified and the pattern of observed vortex shedding is discussed along with the corresponding Strouhal number and lift and drag data.

4.1 Flow in the contact region

To fully understand the flow structures that form around the rolling cylinder, it is helpful to first examine the flow at the point of near contact between the cylinder and the wall. As described in chapter 2, numerical restraints require a small gap ($0.005D$

is chosen here) to be present between the body and the wall. For any given α, the flow structures are largely insensitive to small changes in the gap ratio; however, the flow is heavily dependent on the value of α chosen.

Figure 4.1 shows streamline plots of the flow in the contact region at representative values of α. These streamlines were plotted at irregular intervals so as to better illustrate the regions where stagnation points are present. As was observed by Bearman & Zdravkovich (1978), there exist stagnation points in the contact regions, the number and location of which depend on the value of α. It was not possible to detect any movement of these stagnation points, either with variations in Re at each rotation rate, or with the onset of unsteady flow.

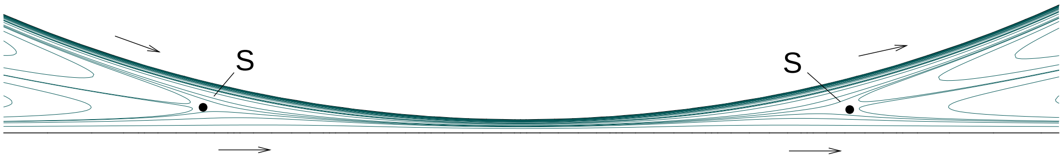

(a) $\alpha = 1$

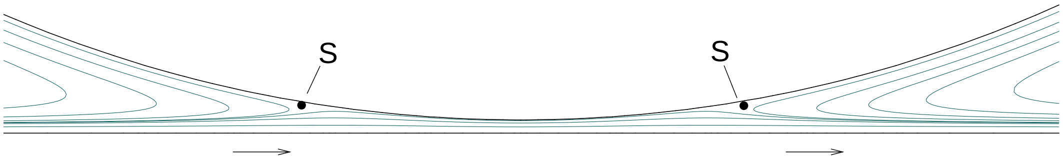

(b) $\alpha = 0$

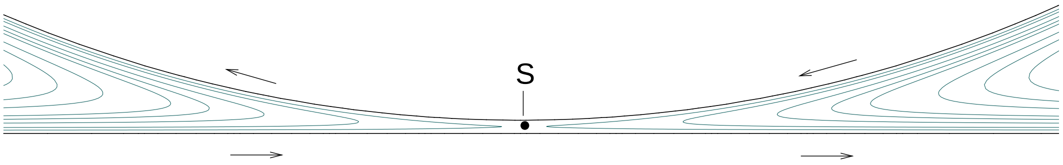

(c) $\alpha = -1$

FIGURE 4.1: Streamlines are plotted for irregularly spaced values of the streamfunction to indicate the flow through the contact region for $Re = 50$ and various rotation rates. Arrows indicate the relative motion of the cylinder and wall. The stagnation points in the flow are indicated with an 'S'.

Figure 4.1(a) shows the streamlines present for 'normal' rolling when $\alpha = 1$. Two stagnation points are present, upstream and downstream of the gap. These are pushed away from the solid boundaries by the entrained fluid layers moving along the wall and the cylinder surface, as is the case for the rotating cylinder in unbounded flow (Ingham

1983; Coutanceau & Ménard 1985; Chew *et al.* 1995; Mittal & Kumar 2003). On the upstream side of the cylinder, the fluid is being carried into the contact region by the moving boundaries. The rapid constriction then causes the flow to change direction and an outflow jet is formed. The reverse is true on the downstream side of the cylinder, where the boundary motions transport the fluid away from the constriction. The flow on the downstream side of the cylinder is therefore carried into the contact region by a central inflow jet. The stagnation points are present in the regions of hyperbolic flow. At the point of nearest contact between the cylinder and the wall, the streamlines are almost parallel and the flow is from left to right.

For $\alpha = 0$ (figure 4.1(b)), there exist two stagnation points, as for $\alpha = 1$, but these are now positioned on the non-rotating cylinder surface. The flow is encouraged to pass through the narrow gap by the relative motion of the moving lower wall. The outflow of fluid from the gap on the upstream side and the inflow on the downstream side now take place closer to the cylinder surface rather than in the region equidistant between the two walls. There also exists a very large shear rate near the cylinder surface where the fluid velocity goes to zero.

Figure 4.1(c) shows the representative streamlines for reversed rotation rates at $\alpha = -1$. In this case, the cylinder and wall motions are opposite in direction at the point of near contact, creating a single region of hyperbolic flow, which has a single stagnation point associated with it. In this configuration, the fluid on the upstream side of the cylinder moves into the gap region along the plane wall and then experiences a reversal and moves away in accordance with the direction of cylinder motion. The opposite is true on the downstream side of the cylinder, with the flow leaving the gap region adjacent to the plane wall. From these plots, one would intuitively expect the case of $\alpha = -1$ to yield the most stable flows, with the possibility of the incoming flow remaining fully attached as it passes from the upstream wall to the cylinder surface and is then carried downstream with the motion of the plane wall.

The presence of the single stagnation point for $\alpha = -1$ yields a flow analogous to that described by Seddon & Mullin (2006), which arises when a continuous row of cavitation bubbles form in the contact region, between the cylinder and the wall. These bubbles block the bulk flow through the gap, causing a complete reversal of the flow upstream of the cylinder and allow the cylinder to move in the opposite direction to the plane wall.

4.2 Steady flow

4.2.1 Flow structure

The steady flow around steps and wall-mounted obstacles has been the subject of studies for some time, with recirculation zones frequently being observed or predicted in the downstream flow. Perhaps the best known example of such a flow is that over a backward-facing step (Armaly *et al.* 1983; Williams & Baker 1997; Barkley *et al.* 2002). In this case, the step and the downstream wall have zero relative velocity and the flow separating from the trailing edge of the step re-attaches to the wall, thereby defining the boundary of a single recirculation zone. In the current investigation, such a re-attachment is not possible as the downstream wall is moving relative to the cylinder. Results from Arnal *et al.* (1991), for the flow behind the square cylinder sliding along a wall, show that this configuration can lead to the formation of *two* recirculation zones. In the present study, this was also found to be the case, with the order in which these two recirculation zones form being dependent on the rotation rate.

α	$R1$	$R2$
1	<20	40
0.5	<20	50
0	<20	70
-0.5	70	100
-1	140	115

TABLE 4.1: Reynolds number of formation of the upper and lower recirculation zones, $R1$ and $R2$. Re was varied in increments of 5.

The values of Reynolds number at which the upper recirculation zone (hereafter referred to as $R1$) and lower recirculation zones ($R2$) are first observed are summarised in table 4.1. These simulations were run at Re increments of 5, and the simulations were started from an unperturbed flow and allowed to develop. The formation of the closed recirculation zones was determined by a detailed inspection of the streamlines at each Re. The typical location of these two recirculation zones are shown by examples of the limiting streamlines in figure 4.2 for three representative rotation rates.

When $\alpha = 0.5$ and 1, the rotation of the cylinder entrains a layer of fluid that opposes the freestream flow. This opposing fluid motion results in the recirculation zone, $R1$, which forms around the cylinder and is displaced away from the wall at its downstream end. This recirculation zone is shown in figure 4.2(a), along with the

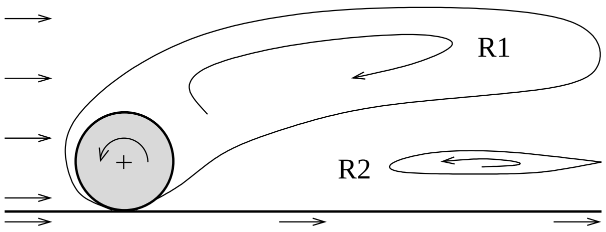

(a) $\alpha = 1$.

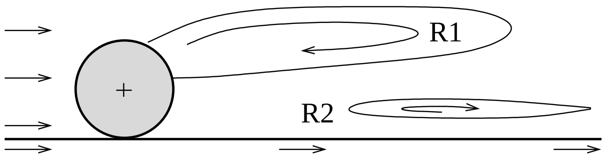

(b) $\alpha = 0$.

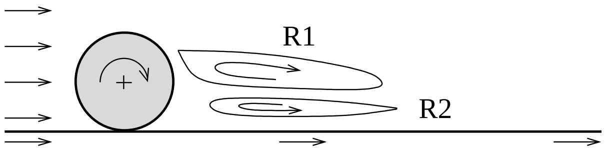

(c) $\alpha = -1$.

FIGURE 4.2:

smaller recirculation zone, $R2$, that forms near the wall. The boundary of $R1$ in the gap region can also be observed in figure 4.1(a) and is represented by the upstream and downstream areas of reversed flow near the cylinder surface. For $\alpha = 0$ (figure 4.2(b)), there is no imposed velocity on the surface of the cylinder and the upper recirculation zone forms from separation and reattachment points on the cylinder surface. For all cases of $\alpha \geq 0$, when both recirculation zones are present the upper recirculation zone is much larger than $R2$ and dominates the wake. The flow around the cylinder for $\alpha = -1$ (figure 4.2(c)), is markedly different to those described above. Due to the sense of rotation of the cylinder when $\alpha < 0$, the entrained fluid moving with the cylinder surface displaces the recirculation zones away from the boundary and into the downstream flow. Also at these rotation rates, the upper recirculation zone is greatly reduced in size and $R2$ forms further upstream toward the cylinder than for $\alpha \geq 0$.

Further information regarding the flow at $\alpha = 1$ can be seen in the streamlines and vorticity contours of figure 4.3(a). The upper recirculation zone, $R1$, is present at all Reynolds numbers considered (down to $Re = 20$), for $\alpha = 0.5$ and 1. The closed recirculation zone creates a corresponding region of reversed flow, downstream of the cylinder near the wall. This reversed flow can be seen in the streamlines of figure 4.3(a), and in 4.3(b), the second recirculation zone near the wall has formed. Also shown in figure 4.3, is the lengthening of the upper recirculation zone with increasing Re, along with the region of negative vorticity that forms over the top of the cylinder.

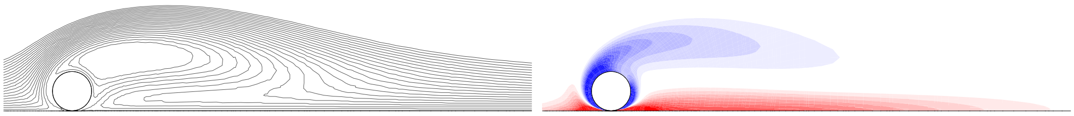

(a) $Re = 30$.

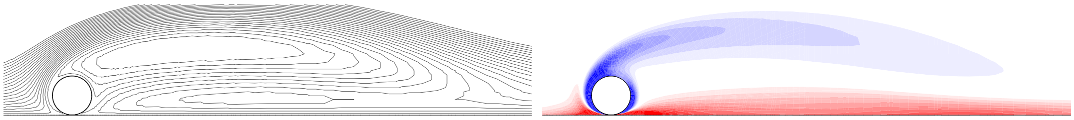

(b) $Re = 60$.

FIGURE 4.3: Streamlines (left) and vorticity contours (right) for steady flow with $\alpha = 1$. Red and blue shading indicates regions of positive and negative vorticity, respectively.

Examples of the steady flow at $\alpha = 0$ are shown in figure 4.4. The flow at this rotation rate bears similarities to that for $\alpha = 1$ and again, $R1$ is present at the lowest Reynolds number considered, $Re = 20$. The position of the separation and reattachment points on the cylinder surface are shown in figure 4.5 for varying Reynolds number. It can be seen that the reattachment point nearer the plane wall remains almost stationary while the upper separation point moves steadily towards the front of the cylinder as Re increases. The lower recirculation zone near the wall forms following an increase in Reynolds number. Again, the length of the recirculation zones increase with Re. However, without any cylinder rotation being present, the regions of reversed flow and vorticity lie closer to the plane wall. This configuration is also more stable than for $\alpha > 0$, with the steady flow extending to higher Re.

The streamlines of figure 4.6(a) show only a slight reversal of the flow near the top of the cylinder when $\alpha = -1$. The majority of the vorticity is in close proximity to the downstream wall. Unlike the other four values of α studied, the lower recirculation zone forms first for $\alpha = -1$. With the cylinder undergoing reversed rotation, it is possible for the flow to remain fully attached as it moves with the boundaries. For both

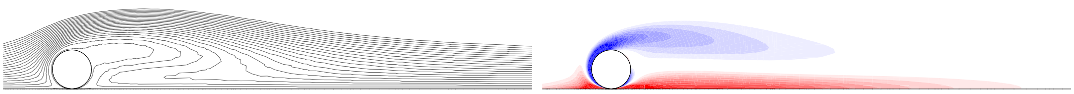

(a) $Re = 50$.

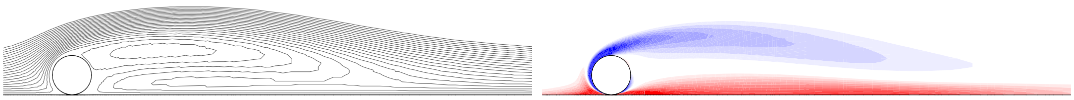

(b) $Re = 100$.

FIGURE 4.4: Streamlines and vorticity contours for steady flow with $\alpha = 0$.

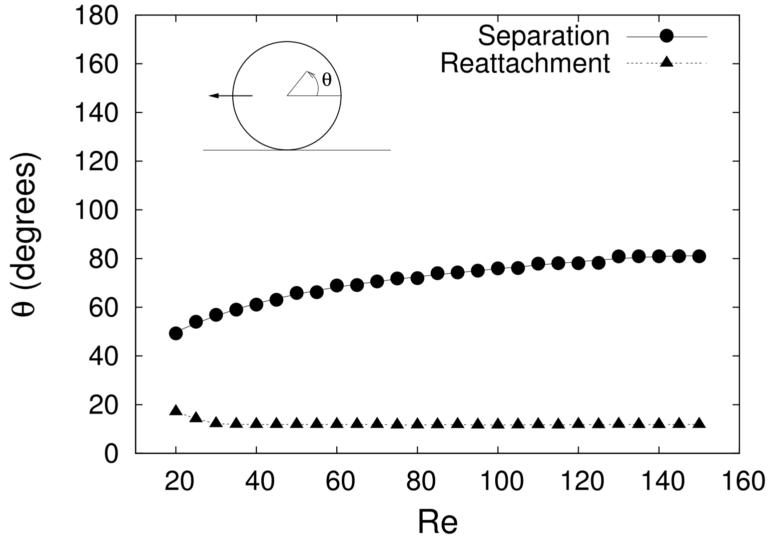

FIGURE 4.5: Separation and reattachment angles (in degrees) of the upper recirculation region for $\alpha = 0$. Angle is measured anti-clockwise from the rear of the body.

$\alpha = -0.5$ and -1, there are no closed recirculation zones present at $Re = 20$. Thus, $\alpha = -1$ provides the most stable configuration observed, with steady flow predicted at Reynolds numbers over 300.

The effect of the rotation rate appears to be that positive values of α displace the steady recirculation zone further from the wall, in agreement with the findings of Cheng & Luo (2007), while the negative rotations confine the vortical structures in the region close to the wall. This is shown in Figs. 4.3 to 4.6, along with the characteristic changes in recirculation length and streamlines with increasing Reynolds number. The stability of the flow is enhanced as the rotation rate is varied from 1 to -1.

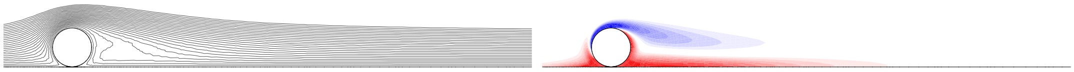

(a) $Re = 80$.

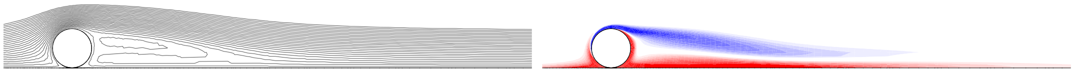

(b) $Re = 300$.

FIGURE 4.6: Streamlines and vorticity contours for steady flow with $\alpha = -1$.

4.2.2 Recirculation lengths

The position and length of the closed recirculation regions vary with the Reynolds number of the flow. The start and end positions of these zones are measured as the upstream- and downstream-most points of the limiting streamline. Accordingly, for $\alpha > 0$, the start of the upper recirculation zone, $R1$, is upstream of the cylinder, while for $\alpha = 0$ it lies on the downstream cylinder surface and for $\alpha < 0$ it is located in the wake. The lower recirculation zone, $R2$, terminates at a hyperbolic point in the flow. These various start and end positions have been plotted as a function of Re for each of the five rotation rates. These results are shown in figure 4.7. The non-dimensional location of the start and end positions are given by $x^* = x/D$, where x is the streamwise co-ordinate measured from the cylinder centre.

It can be seen from figure 4.7 that the start position of $R1$ does not vary greatly with Re. For $\alpha > 0$, the thickness of the entrained fluid layer decreases slightly as the magnitude of rotation decreases. The result is a slight shift in the upstream-most point of $R1$, closer to the cylinder surface. For all other rotation rates, the start of $R1$ moves a small distance upstream as Re is increased. For $\alpha = 0$, this reflects an anti-clockwise movement of the separation point on the cylinder surface toward the top of the cylinder. The scenario is quite different for $R2$, where the upstream-most point of the recirculation zone varies strongly with Re. After initial formation, $R2$ extends a small distance upstream and then maintains a nearly constant value of x^*. This is not the case for the downstream limit of $R2$. For both $R1$ and $R2$, the downstream limit and the overall length increases linearly with Re, following an initial period of non-linear

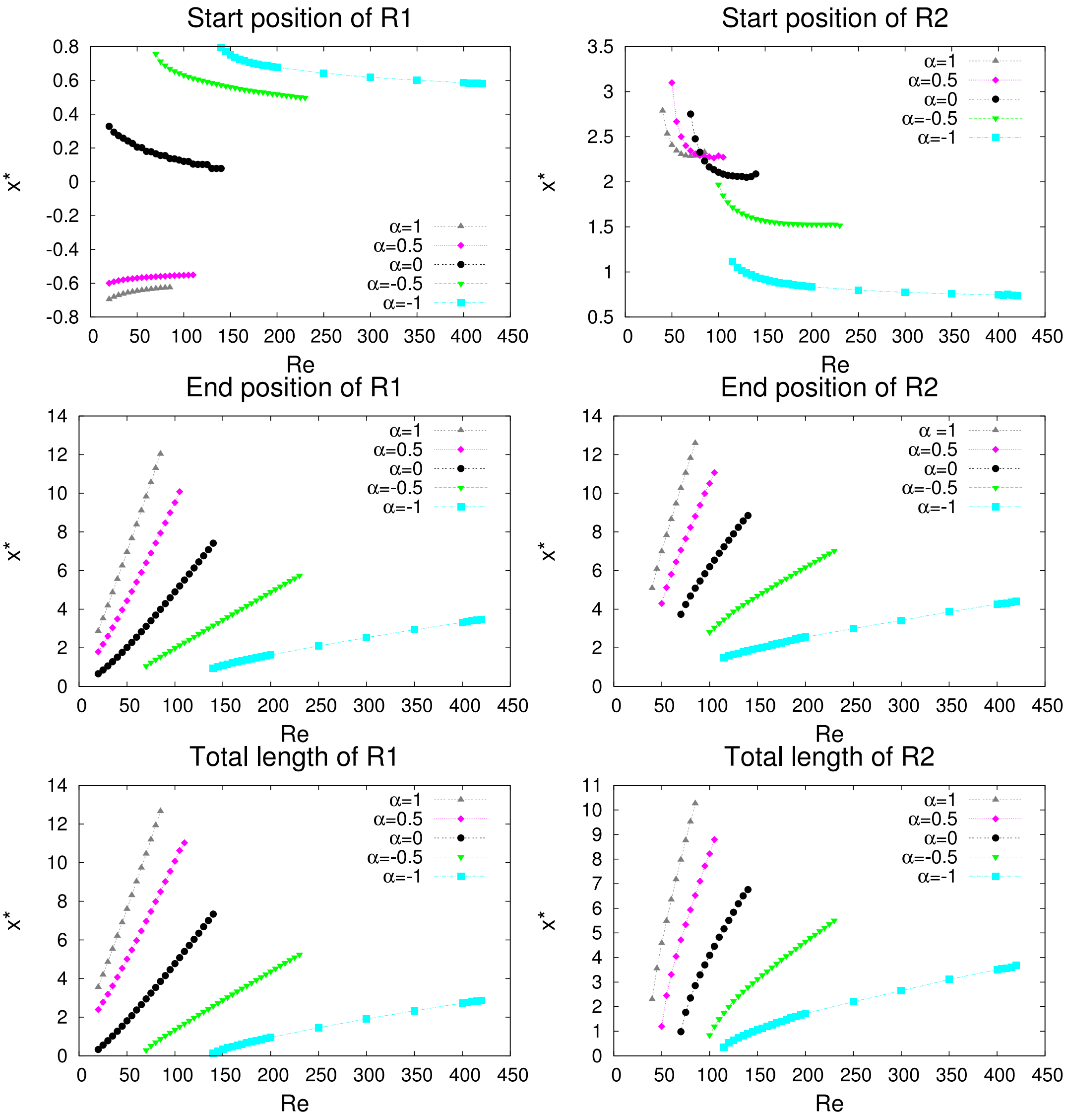

FIGURE 4.7: Streamwise start and end positions and total lengths of the recirculation zones $R1$ and $R2$. The start position of the recirculation zones tends to undergo an initial displacement at lower Re, before reaching an approximately constant position. This is particularly apparent for $R2$. The end position, however, continues to move steadily downstream with increasing Re for both of the recirculation zones. This motion results in two recirculation zones, which following their initial formation, increase size linearly with Re.

growth at Re just above formation. Such a linear increase in the recirculation length is similar to that observed for the recirculation zone behind a cylinder in unbounded flow (Taneda 1956b; Tamaki & Keller 1969; Kawaguti 1966; Dennis & Chang 1970).

As hinted at above, the flows that occur for $\alpha < 0$ are significantly different to those for $\alpha \geq 0$. This relates to the fact that the flow may remain fully attached to the cylinder surface at low Re and for $Re = 20$; no recirculation zones are present for either $\alpha = -0.5$ or -1. The case of $\alpha = -1$ also differs from the other flows in that $R2$ forms at lower Re than $R1$. To gain a clearer understanding of the growth of the recirculation zones, the streamwise positions of $R1$ and $R2$ have been shown with increasing Re in figure 4.8 for the cases of negative α. The rotation rates of $\alpha = -0.5$ and -1 have been shown, where the recirculation zones are detached from the cylinder surface. In both cases the recirculation zone, $R1$, begins at $x^* > 0.5$, (with $x^* = 0.5$ representing the downstream edge of the cylinder). This is not the case for $\alpha \geq 0$, where $R1$ may enclose the cylinder and start upstream of the cylinder boundary. Note that figure 4.8 does not show the displacement of the recirculation zones relative to the plane wall. A typical indication of this is provided in the streamlines of Figs. 4.3(b)-4.6(b).

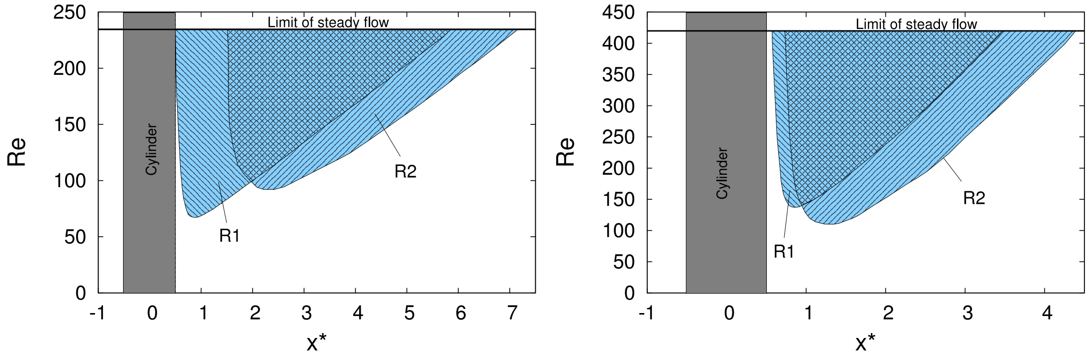

(a) Recirculation zones for $\alpha = -0.5$ with $R1$ forming at lower Re than $R2$.

(b) Recirculation zones for $\alpha = -1$ with $R2$ forming first.

FIGURE 4.8: Growth of the two recirculation zones behind the cylinder for $\alpha < 0$, with increasing Re. The typical case is shown by (a), when the upper recirculation zone, $R1$, forms first. This is observed for all $\alpha \neq -1$. Only at $\alpha = -1$ (as shown in (b)) does the lower recirculation zone, $R2$, form first.

The recirculation zones shown in figure 4.8(a) are typical of the steady flows observed for $\alpha \geq 0$, with $R1$ forming prior to $R2$. The opposite trend is shown in figure 4.8(b), with $R2$ forming prior to $R1$ and with both recirculation zones being significantly shorter. During the investigation, it was observed that the total length of the recirculation zones decreases as α goes from 1 to -1.

4.2.3 Lift and drag trends

Trends in the lift and drag coefficients have been plotted in figure 4.9, for the steady flow regime. Although the forces on the cylinder show some sensitivity to the gap ratio, the resolution study described in section 2.1.4 indicates that the trends shown with increasing Re are expected to hold for $G/D \neq 0.005$ when the cylinder is very close to the wall. The coefficient of drag in figure 4.9 has a log-log relationship that is inversely proportional to Re. The drag coefficient decreases slightly with decreasing α, but is only weakly dependent on the rotation rate. For clarity, only the values of $\alpha = -1, 0$ and 1 have been plotted for C_D, with the other rotation rates lying between these curves.

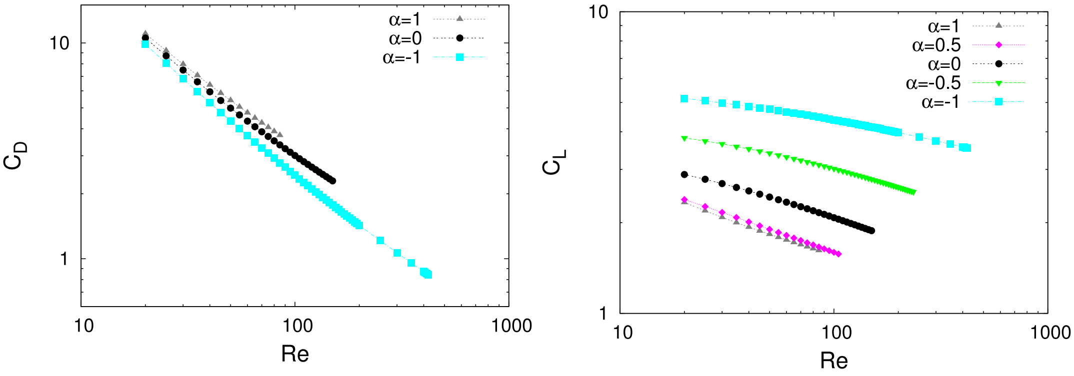

FIGURE 4.9: Coefficients of lift and drag for varying Re and α in the steady regime.

The effect of changing the rotation rate has a much greater influence on the lift than on the drag, especially when $\alpha < 0.5$. The lift force in figure 4.9 decreases with increasing Re and when plotted on log-log axes, the data curves are not as clearly linear as for C_D. When $\alpha = 0.5$ and 1, C_L appears less affected by the varying rotation, and the change in C_L with Re is much closer to a log-log relationship. Unlike the drag force, C_L is observed to increase as α varies from 1 to -1.

In the case of the non-rotating cylinder away from the wall, Henderson (1997) finds that at $Re = 40$, $C_D \approx 1.55$. This is in contrast to the present results for the cylinder sliding along the wall (with $\alpha = 0$), which are over three times this value, with $C_D = 5.93$. From the study of Mittal & Kumar (2003) for the rotating cylinder in an unbounded flow at $Re = 200$, the mean drag coefficients for $\alpha = 1$ and 0.5 are approximately 1.05 and 1.27, respectively. When these values are compared to the present cases where the cylinder motion assists the fluid flow over the surface (when $\alpha = -1$ and $\alpha = -0.5$), the present values of 1.43 and 1.69 again show a significant increase. This indicates that the presence of the wall has a very strong influence on the drag force experienced by the cylinder when undergoing sliding and reversed rolling. This effect may be even more pronounced at lower Reynolds numbers. Also at $Re = 200$, Mittal & Kumar (2003) find that the absolute magnitude of the mean lift coefficient for $\alpha = 1$ and $\alpha = 0.5$ are approximately 2.5 and 1.25, respectively. This compares to values of 3.98 and 2.62 in the present study, indicating that the wall acts to increase the lift as well as the drag.

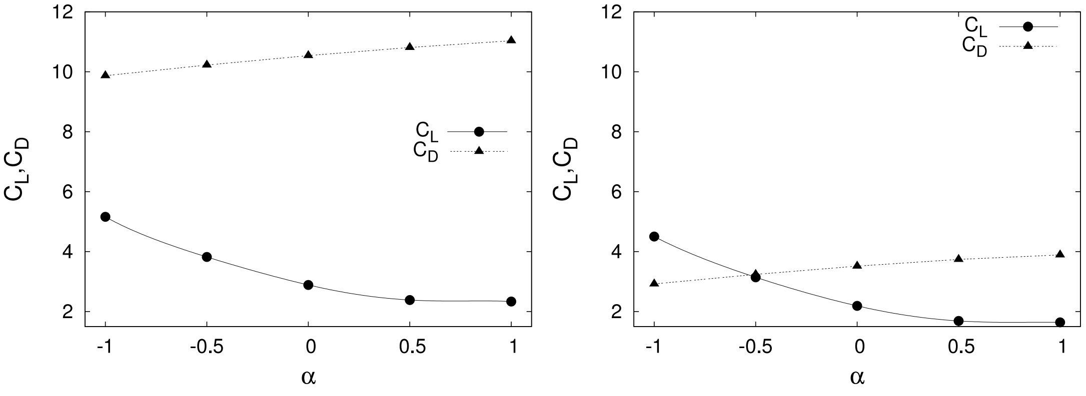

(a) $Re = 20$.

(b) $Re = 80$.

FIGURE 4.10: Change in C_L and C_D with varying α and fixed Re. Increasing the Reynolds number causes a dramatic decrease in C_D, while the overall trends for C_L and C_D remain largely unchanged.

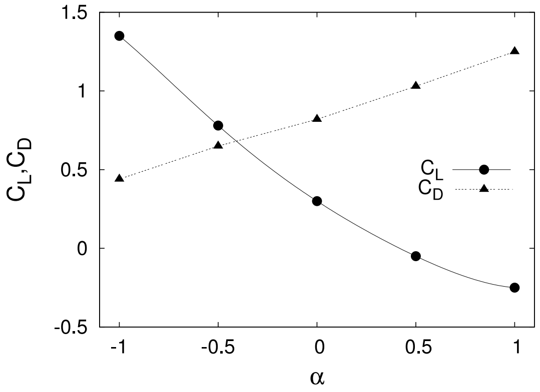

FIGURE 4.11: Lift and drag coefficients taken from Cheng & Luo (2007) for the rotating cylinder near a stationary wall at $Re = 200$ and gap ratios of 0.2 to 0.3.

The effect of varying the rotation rate in the present study can be seen more clearly in the lift and drag plots of figure 4.10. As α is varied from -1 to 1, the change in the steady state lift and drag coefficients is shown at two different Reynolds numbers. At $Re = 20$ (figure 4.10(a)), the drag force dominates for all α and is approximately 2 to 5 times the magnitude of the lift, depending on the value of α. At $Re = 80$ (figure 4.10(b)), this situation changes and the lift and drag are of similar magnitude. Furthermore, as the rotation rate is varied from -1 to 1, the forces on the cylinder change from being lift-dominated to drag-dominated. For all values of α and Re, the lift force is directed away from the wall.

The magnitude of the lift in figure 4.10 increases slightly for all α from $Re = 50$ to

80 but the overall trend remains unchanged. The drag force experiences a far greater drop in magnitude with the increase in Re. As Reynolds number is increased beyond $Re = 80$, the flow becomes time dependent for certain values of α, and therefore a direct comparison of the steady flow C_L and C_D cannot be made at these higher Re.

Although it may be coincidental, the results of figure 4.10(b) show a trend in the lift and drag coefficients that is very similar to those observed by Cheng & Luo (2007), who investigated the flow around a rotating cylinder near a stationary wall at $Re = 200$. They found that, at the smallest gap ratios studied ($0.2 < G/D < 0.3$), the flow was steady for all rotation rates. Their results for the lift and drag coefficients have been replotted in figure 4.11 above.

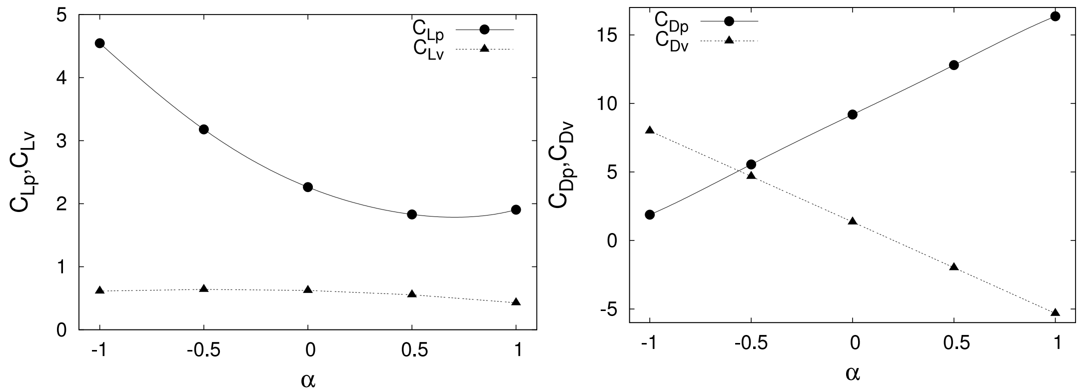

(a) Lift (left) and drag (right) components at $Re = 20$.

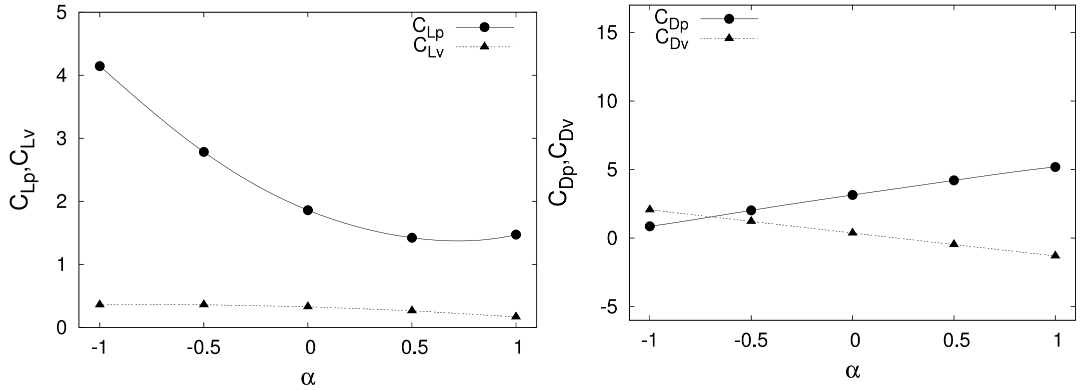

(b) Lift (left) and drag (right) components at $Re = 80$.

FIGURE 4.12: Magnitude of the pressure and viscous components of C_L and C_D for $Re = 20$ and 80. The pressure component dominates the lift force for all Re and α values considered in this study, but the drag force changes from being viscous- to pressure-dominated with varying α.

The viscous drag components shown in figure 4.12 for $Re = 20$ and 80, vary linearly from positive values at $\alpha = -1$, to negative values at $\alpha = 1$. This is because the viscous drag is dominated by the very large velocity gradients at the cylinder surface near the gap region. When the cylinder is undergoing forward rolling ($\alpha > 0$), the velocity gradients in this region will be negative, resulting in a negative viscous drag. This decrease in the viscous drag is offset by an increase in the pressure drag as α goes from -1 to 1. The result is that the total drag force is only slightly affected by varying the rotation rate, while the magnitudes of the pressure and viscous components decrease with increasing Re.

Relative contribution of the pressure and viscous forces on the lift remain almost constant for a given α and increasing Re throughout the steady regime. Figures 4.12(a) and (b) show the relative contributions at $Re = 20$ and 80, respectively. In both cases the trends remain much the same with varying Re. Furthermore, the viscous component of the lift remains almost constant with changing α, while the pressure force provides the dominant contribution to the lift force and decreases as α goes from -1 to 1. However, a slight increase in C_{Lp} is observed for $0.5 < \alpha < 1$, with $\alpha = 1$ having a higher value of C_{Lp}. This increase in the pressure component results in the total lift coefficient being almost equal for $\alpha = 0.5$ and 1. This is in contrast to the results of Cheng & Luo (2007) (figure 4.11), who found C_L to decrease steadily. This may be due to the larger gap ratios employed in their study or the fact that the plane wall was stationary.

The drag coefficient is dominated by the pressure force for all $\alpha \neq 1$. The current observations of the pressure being dominated by the lift force and switching of dominance between the pressure and viscous drag is similar to observations by Kang *et al.* (1999); Tang & Ingham (1991) and Mittal & Kumar (2003) for the rotating cylinder in a freestream. However, in this instance the contribution of C_{Lv} to the total lift is far more significant than for those cases where the wall is not present.

The pressure distribution over the surface of the cylinder has been plotted in figure 4.13, for all values of α and at $Re = 20$, when the pressure forces are greatest. The dominant pressure forces occur in the gap region beneath the cylinder. A positive peak in the pressure develops upstream of the gap where there is strong converging flow and a negative pressure develops downstream in the diverging region. The magnitude of these pressures increases greatly for the cylinder undergoing positive rotation. C_P for $\alpha = 1$ is two orders of magnitude greater than for $\alpha = -1$. As Re increases in the steady regime, the magnitude of these pressure peaks steadily decreases for all α.

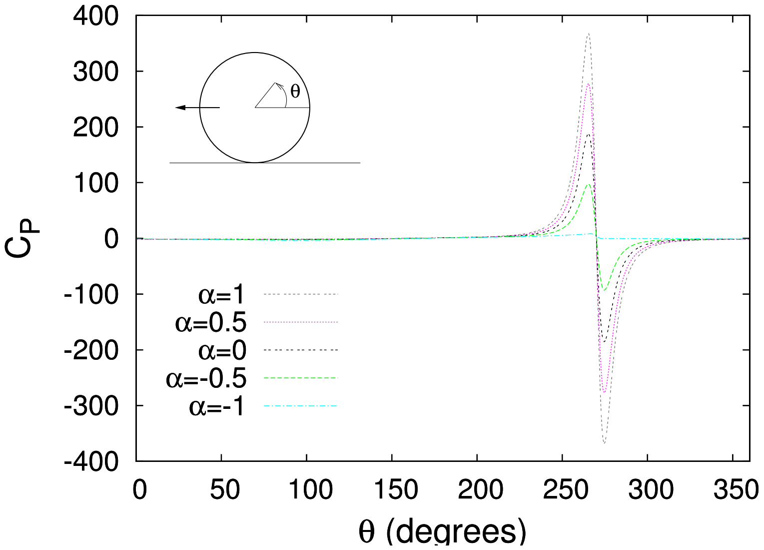

FIGURE 4.13: Pressure distribution on the cylinder surface at *Re* = 20. This represents the minimum Reynolds number considered in the present study, and the one for which the pressures forces on the cylinder are of the highest magnitude.

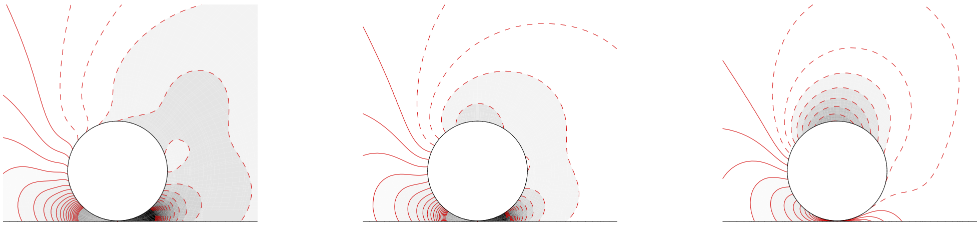

(a) $\alpha = 1$.

(b) $\alpha = 0$.

(c) $\alpha = -1$.

FIGURE 4.14: Contours of constant pressure around the cylinder at *Re* = 20 and various rotation rates. Regions of negative pressure are enclosed with dashed lines.

Figure 4.14 shows the contours of constant pressure in the region of the cylinder during the steady flow regime. Results are shown for representative values of α, with negative pressures enclosed by dashed lines. In can be seen that varying the rotation rate from forward to reversed rolling causes a region of low pressure to move from the rear of the cylinder towards the top of the body, away from the wall. For $\alpha = -1$ (figure 4.14(c)), a region of negative pressure is concentrated very near the top of the cylinder, resulting in an increase in the total lift force. However, the low pressures on the cylinder surface still extend around the downstream side of the cylinder and into the gap region.

4.3 Unsteady flow

4.3.1 Critical *Re* of transition

The critical Reynolds numbers at which the flow is predicted to become unsteady are shown in figure 4.15 below. It has previously been found that the presence of the wall is able to suppress unsteady flow as the gap ratio is reduced and the critical Reynolds number of transition may be extended well beyond that for a cylinder in a freestream (Arnal *et al.* 1991; Nishino *et al.* 2007; Cheng & Luo 2007). In the present study, for $\alpha = 0$, the critical Reynolds number is found to be $Re \approx 160$. This is 3.5 times greater than the value of Re observed for a cylinder in unbounded flow.

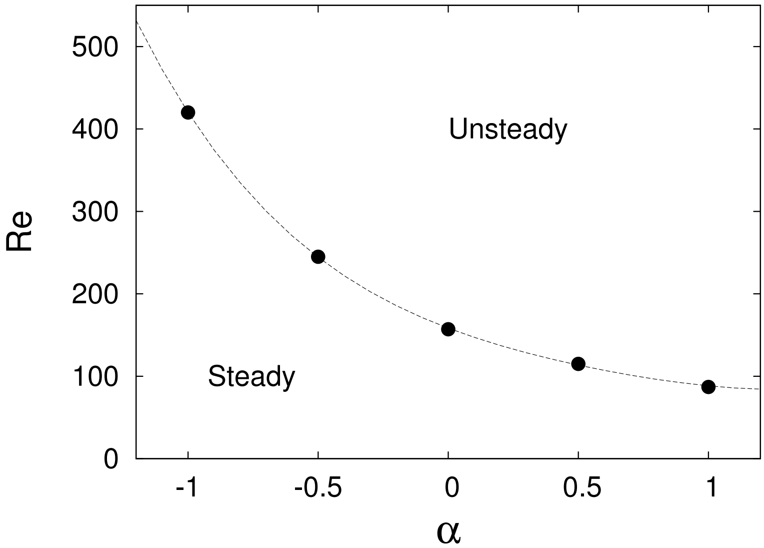

FIGURE 4.15: Transition from steady to unsteady flow as predicted from the two-dimensional simulations. The dashed line represents an approximate curve fit to the transition Reynolds numbers calculated for each α.

From the results of Cheng & Luo (2007), it was found that for the rotating cylinder near the stationary wall, the flow is steady for all $-1 < \alpha < 1$ at gap ratios of 0.2 to 0.3 and $Re = 200$. As the gap ratio in the present study is well below these values, and the transition to unsteady flow occurs at $Re < 200$ for several values of α, the results indicate that the relative motion of the plane wall has a significant destabilising effect on the flow when compared to the cylinder positioned near a stationary wall.

Simulations were generally run from rest, as outlined in Chapter 2. However, a series of simulations were run from previous solutions above and below the Re of transition. As the new solutions develop across the critical Re boundary given in figure 4.15, no hysteresis of the flow is detected. This indicates that the transition takes place via a super-critical Hopf bifurcation.

4.3.2 Flow structures

When the flow becomes time dependent, vortex shedding takes place in the cylinder wake. The shear layer vorticity that forms over the top of the cylinder rolls up into a strong, compact vortical structure. This in turn destabilises the wall shear layer as described in the studies by Sengupta *et al.* (2003) and Lim *et al.* (2004). The current flow satisfies the criteria laid out by Lim *et al.* for unsteady flow to occur. Namely, that the shed vortex is moving significantly slower than the freestream and that the vorticity in the wall shear layer and the shed vortex are of opposite sign.

The destabilised wall shear layer rolls up and forms a counter-rotating vortex pair with the shed vortex. A similar phenomenon has been observed by Arnal *et al.* (1991), in the wake behind a square cylinder in contact with and translating along a plane wall. The movement of the shed vortices in the present study is shown in figure 4.16, with $Re = 200$ and $\alpha = 0$, over a typical shedding cycle. The unequal strength of the two vortices results in a net clockwise rotation of the weaker vortex around the strongest vortex as they propel away from the wall.

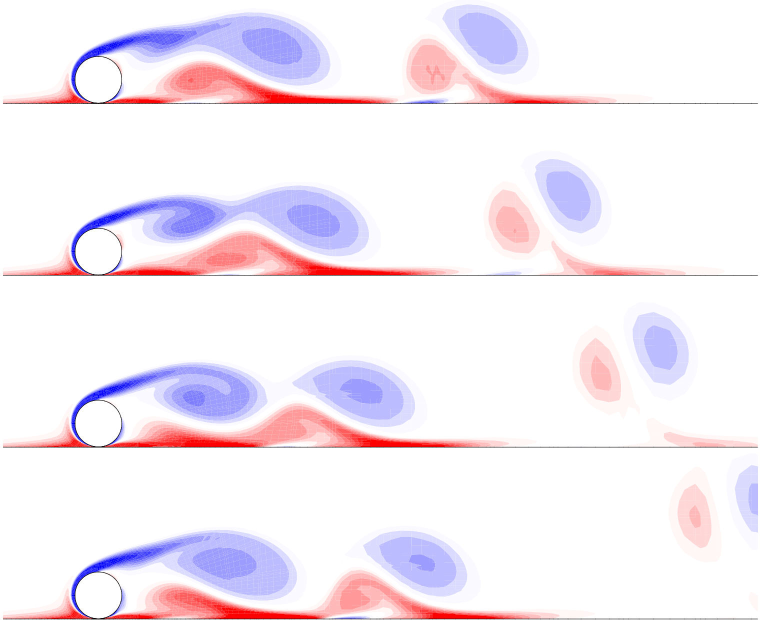

FIGURE 4.16: Vorticity contours for the cylinder with $\alpha = 0$ at $Re = 200$ over a single shedding cycle. The pairing of opposite sign vorticity is shown in red and blue, with a counter-rotating vortex pair propelling away from the wall over time. Following this series of images, the shedding sequence repeats again from the top.

Figs. 4.17 and 4.18 show a comparison of the vortex shedding for varying cylinder

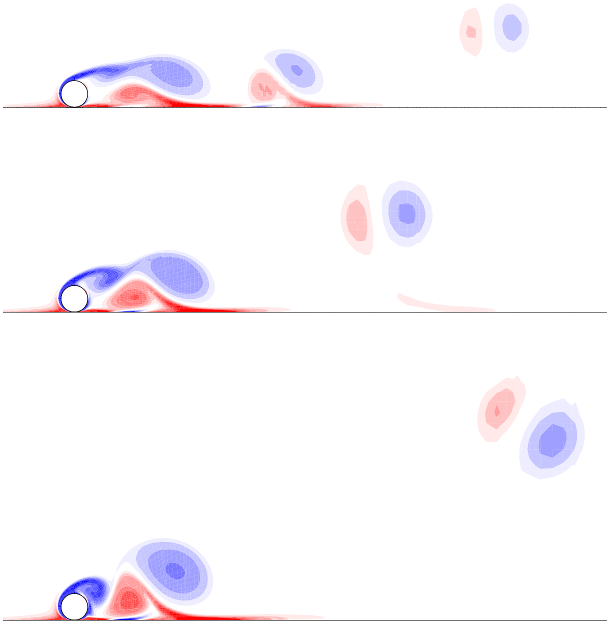

FIGURE 4.17: Vorticity contours for unsteady shedding at $Re = 200$ for $\alpha = 0$, $\alpha = 0.5$ and $\alpha = 1$ respectively, from top. Increasing the magnitude of rotation increases the strength of the shed vorticity and reduces the formation length. Furthermore, the vortex pair that forms in the wake migrates further from the wall.

rotation rates. All images are shown at the moment of maximum lift coefficient in the shedding cycle. Figure 4.17 gives the vorticity contours at $Re = 200$ for the values of $\alpha \geq 0$. From this, it is apparent that increasing the rotation rate from 0 to 1 decreases the formation length of the flow and increases the magnitude of the shed vorticity, causing the vortex pair to be propelled further from the wall. There is also an associated drop in the shedding frequency, which will be discussed in more detail later. At $Re = 200$, the simulations with negative rotation rates still exhibited steady flow. It is therefore necessary to consider higher Re in these cases.

Figure 4.18 shows the unsteady flows for $\alpha \leq 0$ when $Re = 450$. At this higher Re, the flow for $\alpha = 0$ now closely resembles the flow with $\alpha = 1$ from figure 4.17. Increasing the Reynolds number therefore has a similar effect on the flow as increasing the rotation rate. The wake for $\alpha = -1$ is markedly different from the other cases, as the frequency of shedding is much higher and the weak vortex pairs remain adjacent to the wall as they move downstream.

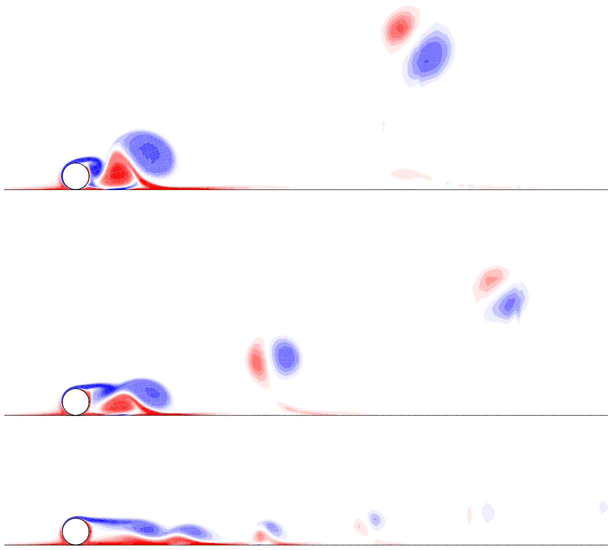

Figure 4.18: Vorticity contours for unsteady shedding at $Re = 450$ for $\alpha = 0$, $\alpha = -0.5$ and $\alpha = -1$ respectively, from top. The same trends are observed as for $\alpha \geq 0$, although the wake for $\alpha = -1$ displays a much higher frequency and lower strength mode of vortex shedding.

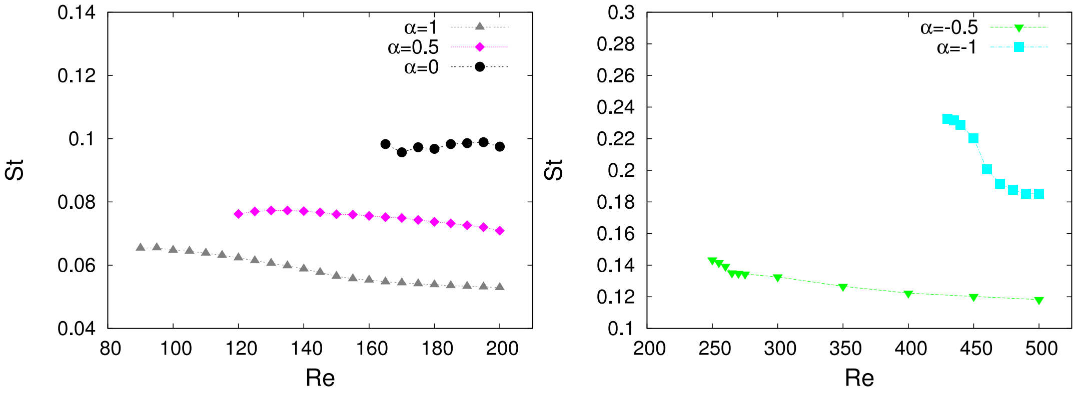

Figure 4.19: Strouhal number plots for all values of α. The trends remain fairly constant over the range of Re considered, except for $\alpha = -1$, where St shows a rapid and steady decrease for $425 < Re < 475$.

4.3.3 St-Re relationship

During the unsteady regime, the frequency of vortex shedding was measured for each value of α and the results are shown in figure 4.19. The Strouhal number increases steadily as α varies from 1 to -1. For all rotation rates apart from $\alpha = -1$, St is lower than for the non-rotating cylinder in an unbounded flow. This is in agreement with the findings of Arnal *et al.* (1991) for the square cylinder sliding along a wall. Arnal *et al.* also found that St remained fairly constant with changes in Re, and a value of $St \approx 0.08$ was recorded. This is slightly lower than the present value of $St \approx 0.1$ for the circular cylinder with $\alpha = 0$. However, the near-constant trend of St with Re is in good agreement with the present findings for all values of $\alpha \neq -1$. Other studies have also found that the wavelength of the vortex street increased for the cylinder near the moving wall (Taneda 1965; Huang & Sung 2007; Lei *et al.* 2000).

The Strouhal number for $\alpha - 0.5$ shows a slight initial decrease with Re. However, this is small in comparison to the variation in St for $\alpha = -1$. In contrast to all the other rotation rates, the shedding frequency for $\alpha = -1$ undergoes a smooth and steady decrease with increasing Re, until an apparent flattening off as $Re \to 500$. The reason for this difference in the flow is not immediately apparent. The relative insensitivity of St to Re for a given α (excepting $\alpha = -1$) is in keeping with the results for unsteady flow behind the cylinder near a stationary wall (Huang & Sung 2007; Lei *et al.* 1999, 2000; Arnal *et al.* 1991).

4.3.4 Lift and drag trends

Once the flow has reached the unsteady regime, the perfectly periodic vortex shedding can be characterised by the mean values of the lift and drag, as shown in Figs. 4.20-4.21.

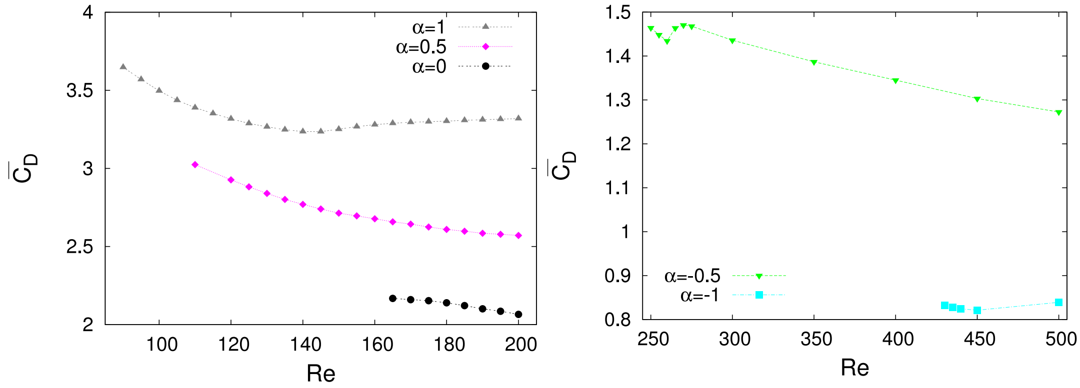

FIGURE 4.20: Mean values of the drag coefficient during the unsteady regime.

For $\alpha = 1, 0.5$ and 0, $\bar{C_L}$ and $\bar{C_D}$ show a smooth variation. The mean drag coefficient changes greatly with α, but has only a weak dependence on Re, with a slight decrease observed in some cases. The overall value of the drag decreases as α goes from 1 to -1. Meanwhile, the lift steadily decreases for $\alpha = 1$ but is almost constant for $\alpha = 0.5$ and 0. For the negative rotation rates, the lift coefficient is nearly constant but with some variation for Re near the initial onset of unsteady flow. As was the case for the steady flow, the magnitude of $\bar{C_L}$ increases as α goes from 1 to -1, with the greatest increases when $\alpha < 0.5$.

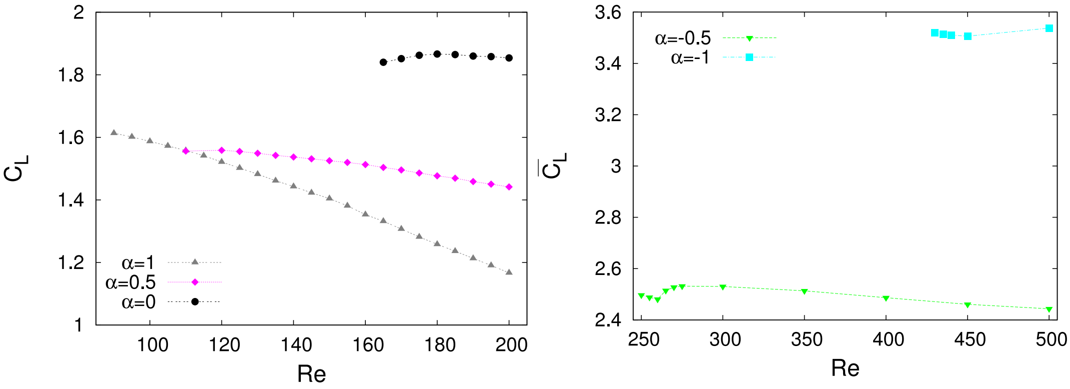

FIGURE 4.21: Mean values of the lift coefficient during the unsteady regime.

4.4 Chapter summary

The numerical simulations have shown that in the small gap region present between the cylinder and the wall, the flow experiences a strong reversal in direction both on the upstream and downstream sides of the cylinder. The flow in this near-contact region is characterised by either one or two stagnation points and the location and number of these points depends on the rotation rate of the cylinder. During the steady flow regime, two recirculation zones are observed in the wake behind the cylinder and these grow linearly with Re, as is reported for the steady wake behind a cylinder in an unbounded flow (Taneda 1956b; Tamaki & Keller 1969; Kawaguti 1966; Dennis & Chang 1970).

When the Reynolds number is increased in the steady regime, the lift and drag forces on the cylinder both decrease. For $\alpha > 0$, the drag dominates the system, while negative rotation rates vary from being drag dominated to lift dominated with increasing Re during the steady flow regime. This trend was similar to that observed by Cheng & Luo (2007) for the rotating cylinder near a stationary wall.

α	Re
1	90
0.5	115
0	160
-0.5	245
-1	425

TABLE 4.2: Critical Reynolds number for the transition from steady to unsteady flow.

Larger magnitude, negative rotation rates are shown to provide the most stable flow, with the unsteady transition delayed until much higher Reynolds numbers. Table 4.2 summarises the Reynolds numbers at which time varying flow was first detected for each α. These values of Re are all much greater than the transition Reynolds number measured for the wake of a cylinder in a freestream. The values of $\alpha > 0$ act to destabilise the flow and decrease the Reynolds number of transition, while $\alpha < 0$ creates a more stable flow that delays the transition. This indicates that if a cylinder was being used in a mixing vessel near a solid boundary, a rotation corresponding to $\alpha > 0$ could enhance the mixing effect.

The unsteady flow that is recorded has similarities to that which develops behind a cylinder in a freestream, with opposite sign vortices forming a pair in the wake. However, in the case of the cylinder near the wall, one vortex is formed from the shear layer over the top of the cylinder and an opposite sign vortex is induced in the wall shear layer behind the body. These vortex pairs propel away from the wall as they move downstream. Except for $\alpha = -1$, the shedding frequency shows less sensitivity to Re than the wake of a cylinder placed in unbounded flow.

Chapter 5

Three-dimensional flow around the cylinder

As an extension of the two-dimensional simulations discussed in section 4, a linear stability analysis was carried out to determine the sensitivity of this two-dimensional base flow to three-dimensional perturbations. This is similar to the methods employed by Barkley & Henderson (1996) and Blackburn & Lopez (2003) for the wake behind a cylinder. The present stability analysis reports that three-dimensional flows will develop prior to the onset of unsteady flow. This is discussed in section 5.1.

A further investigation of the steady three-dimensional wake utilises three-dimensional simulations of the flow. These results are presented in section 5.2 and show very good agreement between the predicted perturbation modes and the fully developed wake.

Finally, section 5.4 reports on the wake that is observed experimentally for the rolling cylinder. The aspect ratio of the cylinder in the experimental setup creates some difficulties in obtaining sustained, two-dimensional flow. However, in both the steady and unsteady regimes, the experimental results provide good qualitative agreement with the numerical simulations when the initial, predominantly two-dimensional wake was considered.

5.1 Linear stability analysis

5.1.1 Critical Re and growth of the mode

As described in section 2.1.3, random noise was added to the two-dimensional flow fields and allowed to develop. The growth of any potential 3D modes was monitored with respect to an associated spanwise or azimuthal wavelength, λ, and the growth rate, σ, recorded. A growth rate greater than zero indicates that the mode will continue to grow over time, while $\sigma < 0$ indicates that the mode will decay. As Re is increased, the wavelength at which the growth rate first reaches zero is referred to as the critical wavelength, λ_c.

The present study finds that, for each of the five values of α, a three-dimensional mode will grow at Reynolds numbers below the predicted onset of unsteadiness. The critical wavelength and Reynolds number, Re_c, as predicted from the linear stability analysis are given in table 5.1 for each value of α. The critical Reynolds numbers are significantly lower than the onset of unsteady flow determined from the two-dimensional simulations of chapter 4. In each instance, the value of Re_c is less than half of the Reynolds number predicted for the development of time-dependent flow.

α	Re_c	λ_c/D
1	35.6	8.5
0.5	48.2	6.9
0	70.8	5.4
-0.5	112	3.6
-1	182	2.2

Table 5.1: Critical wavelength and Reynolds number at which the three-dimensional mode first develops.

The three-dimensional mode occurring in the wake of the rolling and sliding cylinder is markedly different to the mode A and B instabilities occurring behind the cylinder in unbounded flow. For the isolated cylinder, the wake undergoes a Hopf bifurcation and the three-dimensional flow develops on the unsteady base flow. In the present study, the dominant three-dimensional mode occurs during the steady flow regime and the critical wavelength varies greatly with α. The large range of α, from $2.2D$ to $8.5D$ indicates that the three-dimensional mode does not scale directly on any physical aspect of the cylinder geometry such as the diameter.

The fact that the present instability arises on the steady base flow is more closely associated with the absolute instability in the wake behind a backward-facing step, as reported in the studies by Barkley *et al.* (2002) and Beaudoin *et al.* (2004). In their investigation, Barkley *et al.* (2002) found that a backward-facing step with an expansion ratio of 2 undergoes a steady three-dimensional bifurcation at $Re = 748$ (based on the step height, H) with a wavelength of approximately $7H$. In this configuration, the downstream wall is stationary with respect to the step and the wavelength of the instability is directly linked to the length of the recirculation zone. In the study by Beaudoin *et al.* (2004), the critical wavelength varied from $4.5H$ to $7H$ and was dependent, to a certain degree, on the expansion ratio of the channel. A connection between λ_c and the primary recirculation zone is also a possibility in the present study and will be discussed further in section 5.3.

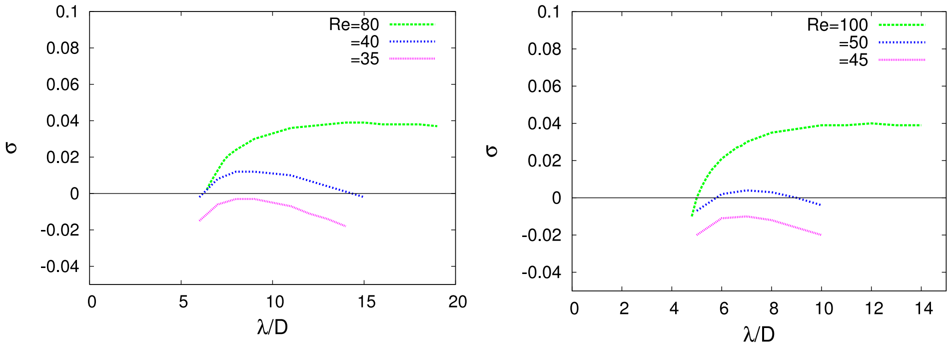

(a) $\alpha = 1$.

(b) $\alpha = 0.5$.

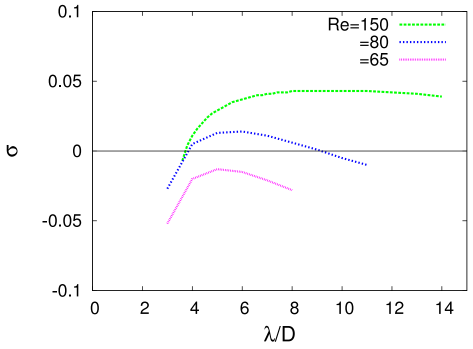

(c) $\alpha = 0$.

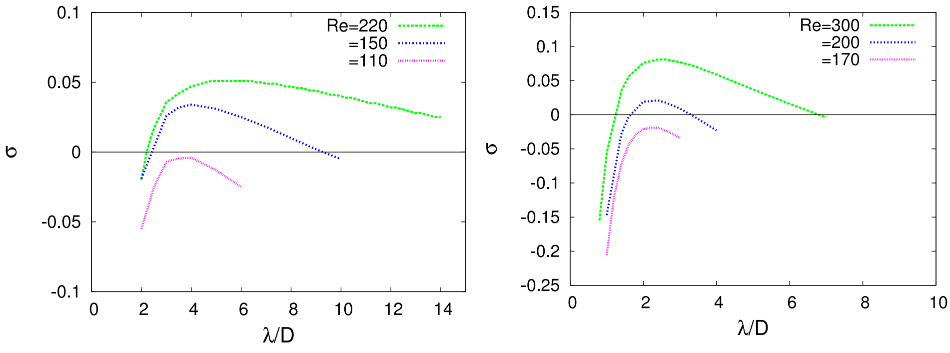

(d) $\alpha = -0.5$.

(e) $\alpha = -1$.

FIGURE 5.1: Variation in growth rate, σ, with wavelength, λ, for Re above and below Re_c.

For each value of α, the dominant three-dimensional mode (i.e., the one that first starts to grow) is time-invariant and the numerical code returns converged (to within

0.1%), real values of the multiplier, μ. From these, and knowing the sampling rate T, the growth rate σ can be calculated according to $\mu = \mathrm{e}^{\sigma T}$, as described in section 2.1.3. Figure 5.1 shows the growth rate as a function of the wavelength for Reynolds numbers above and below Re_c for each rotation rate. In figures 5.1(a)-5.1(e), there is a similarity between the stability contours for Re above and below Re_c. However, as the Reynolds number increases above Re_c, the wavelength with the largest growth rate gradually shifts to larger values. This is particularly apparent in figures 5.1(a)-5.1(c), in which the stability curve flattens out at higher λ and there is a large range of λ with approximately equal growth rate.

5.1.2 Neutral stability curves

For each $Re > Re_c$, there are two values of λ for which $\sigma = 0$. For wavelengths between these two values, the growth rate is greater than zero (as demonstrated by the blue curves in figure 5.1) and the flow is unstable to three-dimensional perturbations. These values of λ for which $\sigma = 0$ can therefore describe the boundaries between two- and three-dimensional flow with varying Re. These are often termed contours of neutral stability, and they are plotted for each α in figure 5.2. For Reynolds numbers to the left of these contours, the flow is steady and two-dimensional, while to the right the flow is steady and three-dimensional. The values of λ_c and Re_c correspond to the left-most point on each curve.

5.1.3 Perturbation modes

From the stability analysis, it is possible to plot the fields of perturbation vorticity acting on the two-dimensional, steady base flow. Regions of the flow with a high perturbation vorticity serve as an indication of the areas in which the three-dimensional mode first develops. Figure 5.3 shows the contours of streamwise perturbation vorticity at representative values of α. The spanwise vorticity of the two-dimensional base flow and the streamlines of the flow have also been shown to indicate the structure present in the base flow.

For $\alpha \geq 0$, the strongest regions of perturbation vorticity lie on the surface of the cylinder, near the top on the downstream side and on the moving wall just downstream of the cylinder. This configuration has similarities to those reported by Barkley *et al.* (2002) for the backward-facing step. They found that the regions of strongest instability (and those with the largest spanwise velocity) occurred on the downstream face of the

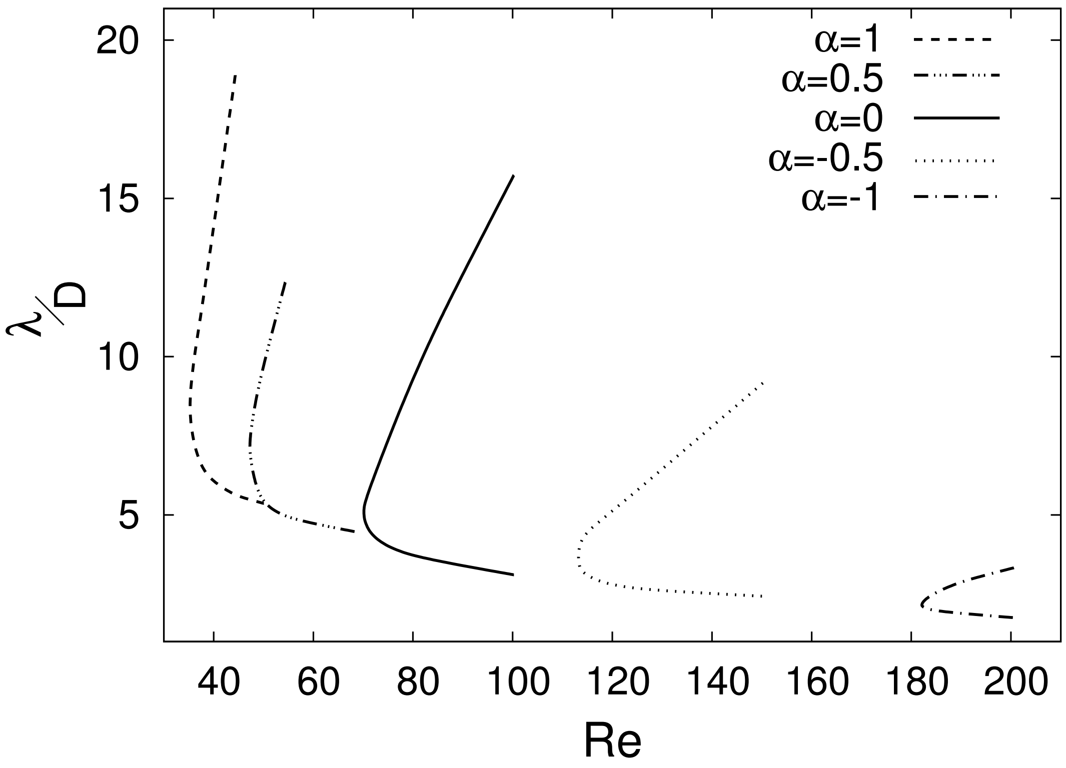

FIGURE 5.2: Curves of neutral stability for which $\sigma = 0$, indicating the transition to three-dimensional flow.

step and in the reattachment point of the primary recirculation zone. In the present case, there is no concentration of streamwise vorticity at the downstream ends of the upper or lower recirculation zones (the lower recirculation zone was small but present in each of the figures). Instead, the perturbation vorticity in the wake tends to lie within the limits of the recirculation zones.

The images to the left of figure 5.3 show areas of lower intensity streamwise vorticity associated with the upper region of base flow vorticity. However, it is only for the cases of $\alpha < 0$ that the strength of the vorticity in these regions dominates the perturbation field. In figure 5.3(c), there remain regions of vorticity on the surface of the cylinder but these have reduced in both size and magnitude. This is a logical consequence of the reversed rotation of the cylinder, in which the shear on the surface has been significantly reduced.

The perturbation vorticity is periodic along the span of the cylinder. This accounts for the regions of vorticity in figure 5.3(b) that appear to be of opposite sign to the corresponding regions in figures 5.3(b) and 5.3(c). In this case, the random perturbation that is initially added to the flow field has developed ‘out-of-phase’ to the other two. This is inconsequential as the sign of the perturbation vorticity changes every half

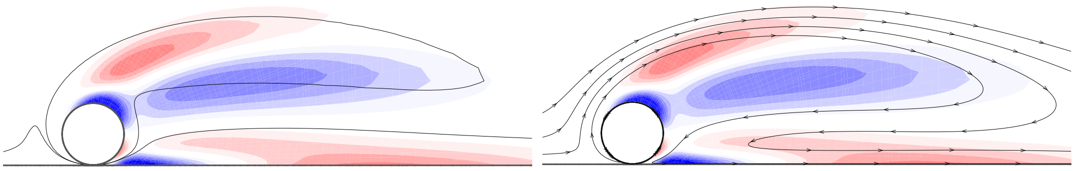

(a) $Re = 40$, $\lambda = 9D$.

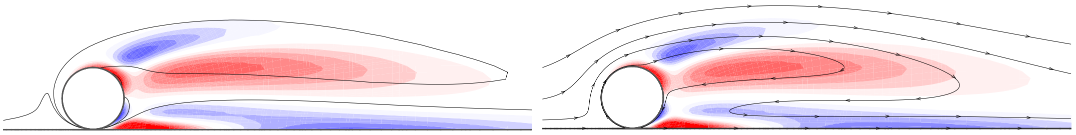

(b) $Re = 75$, $\lambda = 6D$.

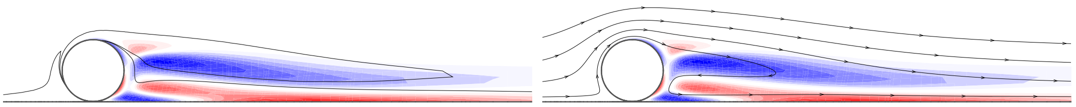

(c) $Re = 200$, $\lambda = 2.8D$.

FIGURE 5.3: Streamwise perturbation contours are shown in red (positive) and blue (negative). The figures to the left have a single level of the base flow vorticity plotted, while the figures on the right show streamlines of the flow. The streamlines have been plotted at irregular intervals to give an indication of the regions of recirculating fluid.

wavelength along the span of the cylinder. This alternation in the spanwise direction is more clearly apparent in a three-dimensional reconstruction of the perturbation mode.

The two-dimensional perturbation fields obtained from the stability analysis can be entered into the three-dimensional code described in section 2.1.2 and extended in the spanwise direction. This provides a clearer image of the structure of the perturbation mode. Three-dimensional surface plots of vorticity, illustrating the modes reported in figures 5.3(a)-5.3(c), are given in figure 5.4 over one wavelength of the span. The plotting conventions are the same as in the previous figure and the surfaces of streamwise vorticity are all shown at approximately one quarter of the maximum/minimum.

The vortical structures of figure 5.4 represent the shape of the *initial* perturbation to the flow. As such, it may not be the same as the streamwise vorticity in the fully developed three-dimensional flow. After the mode first develops, it may continue to grow and non-linearities are necessary to cause the mode to saturate, thereby changing the structure. Similarities between the perturbation mode and the three-dimensional flows will be examined in more detail in section 5.2.

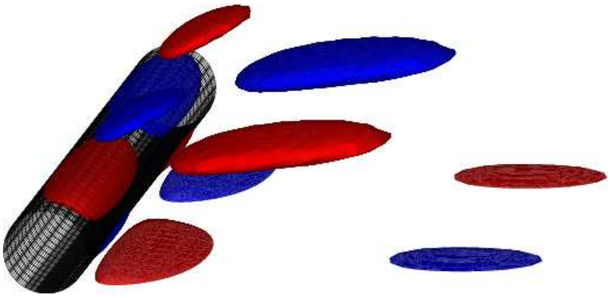

(a) $\alpha = 1$, $Re = 40$, $\lambda = 9D$.

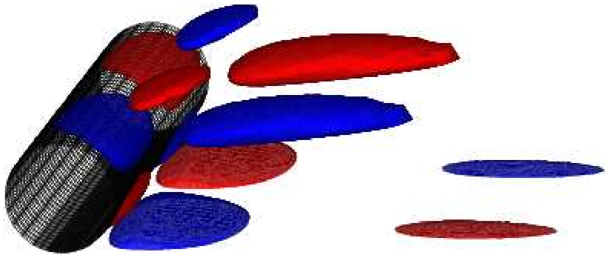

(b) $\alpha = 0$, $Re = 75$, $\lambda = 5D$.

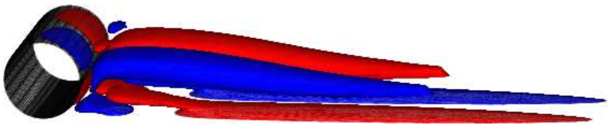

(c) $\alpha = -1$, $Re = 200$, $\lambda = 2.2D$.

FIGURE 5.4: Three-dimensional reconstruction of the predicted perturbation mode. Contours show the streamwise perturbation vorticity.

As noted above for the two-dimensional fields of perturbation vorticity, figure 5.4 shows the presence of three-dimensional regions of vorticity on the cylinder surface and the downstream wall. The vorticity in the wake takes the form of an opposite signed pair of flattened streamwise vortices that extend downstream. This is similar to the three-dimensional wake behind the backward-facing step, which is described by Barkley *et al.* (2002) as a series of 'flat rolls'. In the present study, these 'flat rolls' are displaced further from the wall by the relative motion of the wall and the lower recirculation zone.

In figure 5.4, there exist smaller regions of opposite sign vorticity that lie further from the body, toward the freestream. These small regions of vorticity have almost disappeared for $\alpha = -1$, indicating that their formation is linked to the size and strength of the vorticity forming on the top surface of the cylinder. As was the case for the spanwise vorticity observed in the two-dimensional simulations of section 4.2, the placement of the streamwise vortices moves closer to the wall as α varies from 1 to -1. Furthermore, the spanwise length of the structure narrows until, for $\alpha = -1$, the width of each of the streamwise vortices is close to $1D$. In the case of $\alpha = -1$, the perturbation mode looks less like the 'flat rolls' described by Barkley *et al.* (2002) for flow behind the backward-facing step (the form of which can be seen in figure 5.4(a) and 5.4(b) without too much difficulty), and more closely resemble Görtler vortices, which form long streamwise vortices (see Saric (1994) for details). This shall be considered further in section 5.3.

Although the dominant mode has been found to develop on the steady base flow, there exists the possibility of other three-dimensional modes with an associated periodicity. There is some evidence for this at higher Reynolds number when the base flow is unsteady, and the growth rate (as calculated from the real component of μ) is observed to vary over time. Only a very limited number of cases were considered for the three-dimensional structures present on the unsteady base flow, due to the fact that the flow is known to first become three-dimensional. However, the results of Floquet analysis carried out on the unsteady base flow shall be mentioned briefly as a point of interest, with the possibility of complex periodic modes.

When considering the time-varying base flow, one point of interest was the detection of a non-dominant complex mode that appears to repeat every two base flow periods. The Floquet multiplier for this mode is given in figure 5.5 for $\alpha = 1$ at $Re = 100$. This differs from the subharmonic, or period doubling mode, in that $|\mu|$ oscillates about a mean value. In the case of the subharmonic mode, the sign of vorticity switches each period but the distribution of vorticity remains the same, and as a consequence, the value of $|\mu|$ remains constant. Details of subharmonic modes can be found in Sheard *et al.* (2005) for the flow around rings and Leontini *et al.* (2007) for a cylinder undergoing forced oscillation.

The Floquet multiplier in figure 5.5 is calculated and plotted over consecutive base flow periods. As discussed in section 2.1.3, if a three-dimensional mode has an associated periodicity, μ takes the form of a complex pair, the complex component of which is not resolved by the current power method. However, Blackburn & Lopez (2003) have shown that the oscillatory values of $|\mu|$, and hence σ, obtained by the power method will

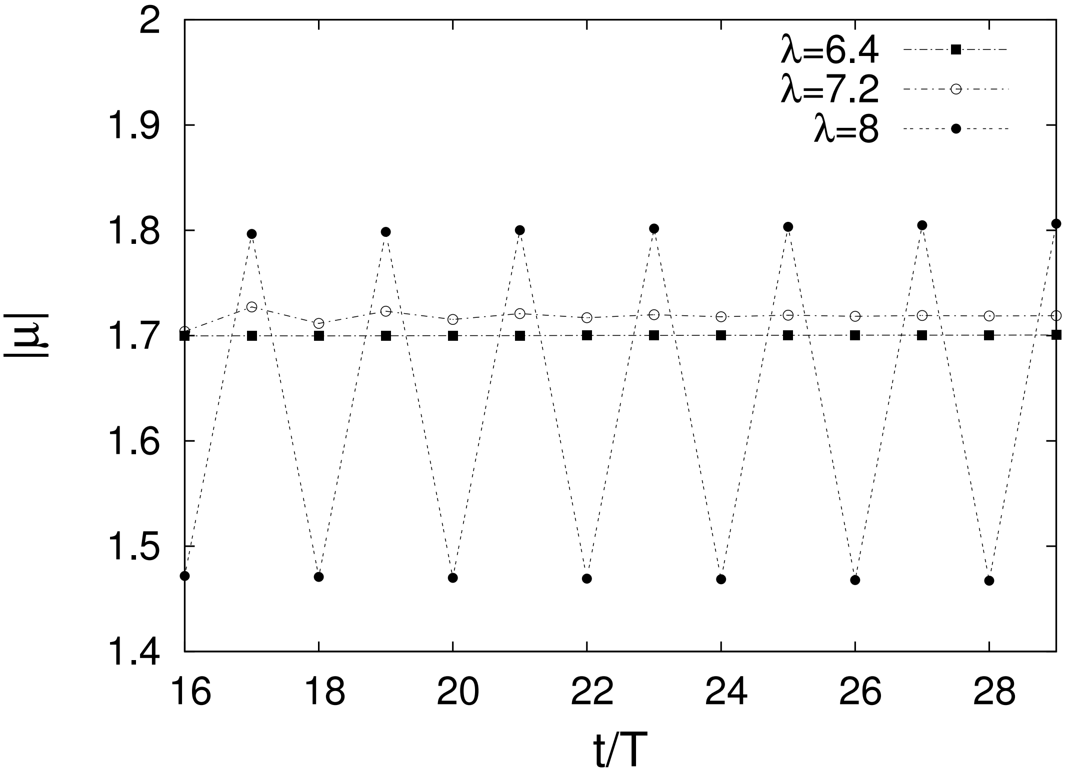

FIGURE 5.5: Floquet multipliers calculated for each base flow period with $\alpha = 1$, $Re = 100$.

oscillate about a mean value that is equal to $|\mu|$ as obtained from the Krylov subspace method, which considers the complex value of the multiplier. The oscillation of $|\mu|$ in figure 5.5 is therefore indicative of a complex mode, the true magnitude of which is the average of the oscillating values. As the mean value of $|\mu|$ for $\lambda = 8$ is less than the constant values of $|\mu|$ at lower wavelength, this is not the fastest growing mode.

The streamwise perturbation vorticity for the modes at $Re = 100$, $\lambda = 6$ and 8 is shown in figure 5.6, and the solid lines indicate the contours of spanwise base flow vorticity. Figure 5.6(a) shows a region of negative vorticity in the core of the vortex forming over the top of the cylinder and a region of positive vorticity developing in the high shear region between vortices. This is a real mode, having a period equal to that of the base flow. Images taken one period apart are identical for this mode. Visually, the location of the perturbation vorticity in figure 5.6(a) bears some resemblance to the mode A instability behind a cylinder in unbounded flow (Barkley & Henderson 1996; Leontini *et al.* 2007). However, the proximity of the wall in the present study precludes any straightforward assumptions linking the transition mechanisms present in the two flows.

Figure 5.6(b) shows two images of the perturbation vorticity taken one period apart

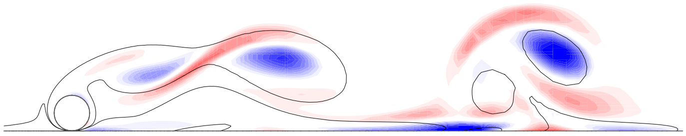

(a) $\lambda = 6D$.

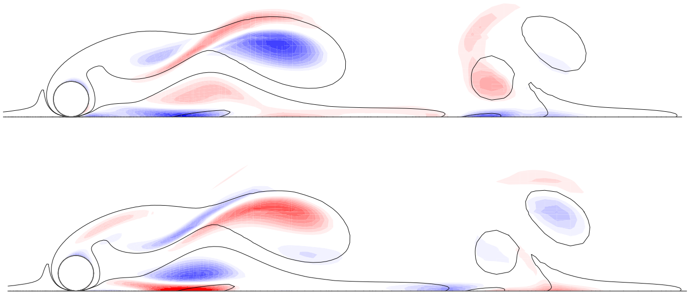

(b) $\lambda = 8D$. Top image has $|\mu| = 1.47$ and the bottom image has $|\mu| = 1.81$

FIGURE 5.6: Plots of the streamwise perturbation vorticity for $\alpha = 1$, $Re = 100$ showing (a) the converged instability mode at $\lambda = 6D$, which repeats with the base flow, and (b) the complex three-dimensional mode predicted for $\lambda = 8D$, which varies slowly over time with the wake flow almost repeating every two base flow periods.

with $\lambda = 8D$. Inspection of the vorticity contours indicates that this mode may not be fully converged, and that the values of $|\mu|$ shown in figure 5.5 vary by a small amount every two periods of the base flow. From one period to the next, the dominant regions of perturbation vorticity in the near wake change sign. Compared to the dominant mode of figure 5.6(a), there exists also an additional region of vorticity near the plane wall. The study of the fully three-dimensional, unsteady flow behind the rolling and sliding cylinder presents an interesting opportunity for further work.

5.2 Three-dimensional simulations

In order to analyse the agreement between the predicted perturbation modes described above and the fully developed three-dimensional flow, simulations were run using the three-dimensional code described in section 2.1. The spanwise cylinder domain is set equal to either one or four wavelengths of the three-dimensional instability, with 36 Fourier planes used in the spanwise direction. This corresponds to either 9 or 36 planes per wavelength.

During the three-dimensional simulations, the same mesh was used as for the two-

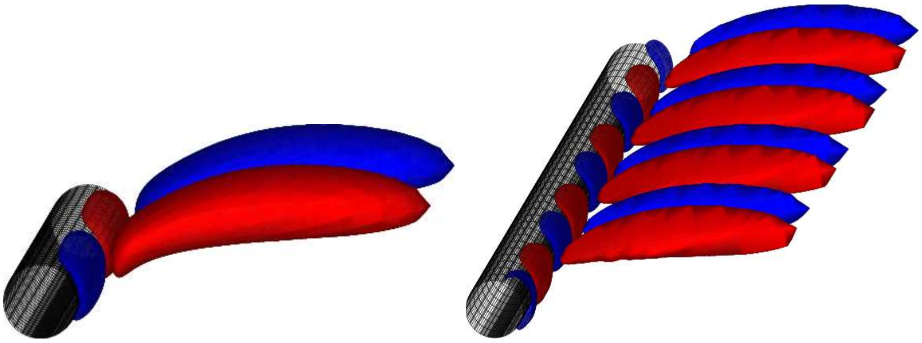

(a) $\alpha = 1$, $Re = 40$, $\lambda = 9D$.

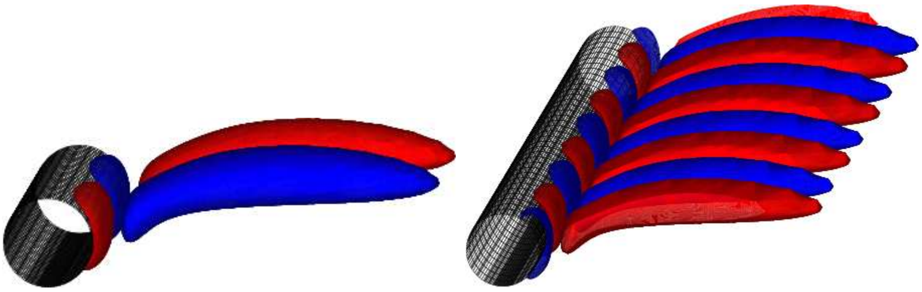

(b) $\alpha = 0$, $Re = 75$, $\lambda = 5D$.

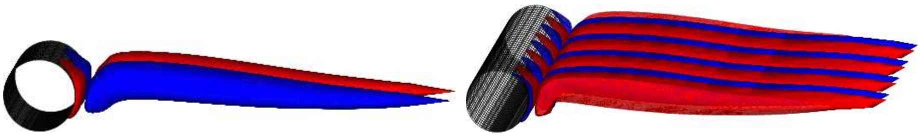

(c) $\alpha = -1$, $Re = 200$, $\lambda = 2.2D$.

FIGURE 5.7: Comparison between the predicted perturbation mode and the three-dimensional simulations. For clarity, surfaces of transverse vorticity (normal to the wall) are shown. Images on the left show the predicted perturbation mode and images to the right show the fully developed wake mode from the three-dimensional simulations, taken over a spanwise distance of 4λ.

dimensional simulations and projected in the spanwise direction. Figure 5.7 shows the resulting surface plots of the transverse vorticity, directed normal to the wall. The images on the left of figure 5.7 correspond to the perturbation modes of figure 5.4, but here, the transverse vorticity has been plotted for clarity and to provide additional information about the structure of the wake. These contours are again plotted at one quarter of the maximum/minimum levels and reflect the swirling motion of the fluid in a plane parallel to the moving wall. The three-dimensional simulations show a distance of 4λ in the spanwise direction. These results provide a qualitative comparison between the predicted and observed vortical structures in the wake and a very good agreement exists between the two. As the three-dimensional simulations are developed over time, the streamwise vortices develop in the near wake and steadily increase in length until the converged solution shown here is obtained.

5.3 The transition mechanism

The mechanism responsible for the transition to three-dimensional steady flow is not immediately apparent. Given that three-dimensional flow bears similarities to that reported behind the backward-facing step, this was used as a starting point for identifying the mechanism. The transition mechanism for the backward-facing step flow has still not been clearly explained but the evidence suggests some type of centrifugal instability. One explanation is put forward by Ghia *et al.* (1989) who propose that Taylor-Görtler vortices form as the result of the concave shear layer passing over the top of the step, between the upper and lower recirculation zones. Barkley *et al.* (2002) discount this theory stating that the they find the region of concave flow to remain linearly stable over a large range of Re and that the instability does not take the form of streamwise vortices in the main flow, as would be expected, but is linked to the primary recirculation zone behind the step.

A connection between the three-dimensional instability and the location of the lower recirculation zone is noted in the present study. Even for the case of figure 5.4(c), when the streamwise vortices are less flattened, the structures are confined to the regions of recirculating fluid. From their stability analysis of the backward-facing step, Barkley *et al.* (2002) believe the mechanism of transition to be centrifugal in nature and they associate it with the closed streamlines in primary recirculation zone. A similar method to that used by Barkley *et al.* (2002) has therefore been employed to analyse the steady two-dimensional recirculating flow for possible regions of instability.

At this point it is worth mentioning that the onset of the three-dimensional flow, as predicted by the stability analysis, occurs very close to the Reynolds number at which the lower recirculation zone, $R2$, is first observed in the two-dimensional simulations for $\alpha = 1$, 0.5 and 0. It is therefore possible that the formation of this recirculation zone plays a part in the onset of three-dimensional flow. For this reason, both of the recirculation zones, $R1$ and $R2$, are tested for regions of centrifugal instability.

The basic premise for centrifugal instability is Rayleigh's criterion (as outlined in

Drazin & Reid (1981)) and this was generalised by Bayly (1988) for the case of inviscid flow with convex closed streamlines. Bayly (1988) states that regions of possible centrifugal instability arise when the streamlines are closed (as in a zone of recirculating fluid) and that the circulation decreases outwards in some portion of the flow. This condition is satisfied in the flow behind a blockage or backward-facing step (Griffith *et al.* 2007; Barkley *et al.* 2002), when the presence of the stationary walls reduces the velocity of the nearby flow to such an extent that the overall circulation is reduced. For the backward-facing step, Barkley *et al.* (2002) found these conditions to be satisfied on the wall immediately downstream of the step and at the reattachment point of the limiting streamline representing the primary recirculation zone.

Given the above requirements for centrifugal instability, and the fact that the circulation, Γ, is defined as the integral of $\mathbf{u} \cdot d\mathbf{l}$ around one circuit of the streamline, it is possible within the numerical code to calculate a value of Γ for a series of streamlines within each recirculation zone. The above process was carried out for both recirculation zones at $\alpha = 1$, $Re = 50$, $\alpha = 0$, $Re = 75$ and $\alpha = -1$, $Re = 300$. For all these α-Re pairs, the flow is three-dimensional and both recirculation zones are fully formed However, no evidence of outwardly decreasing circulation was found in any of the above cases. This does not eliminate the possibility of a centrifugal instability in the flow but suggests that, if one is present, it does not originate within the highly elliptical recirculation zones. With consideration, the lack of a decrease in circulation can be clearly accounted for by the presence of the moving wall. In the present study, where the frame of reference is attached to the cylinder centre, there are no stationary boundaries (except for the cylinder surface when $\alpha = 0$) to cause a decrease in the velocity of the flow. Rather, the motion of the recirculating fluid in each case is accelerated by the moving boundaries, causing an increase in $\mathbf{u}$ and Γ.

In conclusion, the mechanism responsible for the transition to three-dimensional flow has not been clearly identified. Research has shown that it is unlikely to be due to a centrifugal instability arising within the recirculation zones. Further inspection of the three-dimensional structures and their placement inside the recirculation zones seems to eliminate the possibility of the three-dimensional flow arising due to a Görtler-type instability in the boundary layer. It is still possible that the three-dimensional modes arise due to a centrifugal instability, although this may be confined to the small region near the cylinder surface or the downstream wall.

5.4 Experimental results for the cylinder

As three-dimensional modes are predicted to exist before the onset of unsteady flow, it is likely that the structure of the unsteady modes in section 4.3 will be altered. As a means of qualitatively testing the accuracy of the two-dimensional, time-varying simulations, experimental flow visualisations were used for comparison. In the experimental setup, it was difficult to reduce to cylinder diameter below 9 mm and still be able to obtain clear images of the flow. This limits the maximum achievable length-to-diameter aspect ratio for the cylinder experiments to approximately 13.3. This is not large enough to discount the effects of the side walls once the flow had been allowed to develop over time.

After the experimental cylinder flow was allowed to develop, the effect of the side walls could be observed by placing a laser sheet in the vertical plane parallel to the cylinder in the near wake. The resulting three-dimensional flow took the form described by Williams & Baker (1997) for the flow behind a backward-facing step. Fluid jets originating at the boundaries penetrate the flow in the spanwise direction, until reaching the central symmetry plane. In order to minimise these wall effects, observations were made of the flow immediately after start-up of the cylinder motion. At this time, the flow was largely free of three-dimensional effects and a qualitative comparison could be made between the formation of vortices in the near wake and the two-dimensional numerical flows. All images were taken with the light sheet positioned in the vertical centre-plane of the cylinder span.

While both steady and unsteady flows were recorded in the experiments, steady flow could not be observed for $\alpha \geq 0$, due to the minimum achievable Re in the channel. At $Re \approx 80$, time varying flow persisted for $\alpha = 0$, 0.5 and 1. This was below the predicted onset of unsteady flow from the simulations (figure 4.15) and it is expected that three-dimensional perturbations in the experimental flow are likely to trigger the unsteady bifurcation at lower Re. An example of the steady flow for $\alpha = -1$ and $Re = 250$ is shown in figure 5.8. The results of the experimental dye visualisation are shown in green, with the dye present in the region between the upper and lower recirculation zones. The numerically predicted steamlines are plotted over the top in light grey. A good qualitative agreement exists for the positions of the two recirculation zones.

For the cases of $\alpha \geq 0$, the unsteady flow is more clearly observed at lower Re, when the reduced speed of the water channel allows the flow to remain laminar and

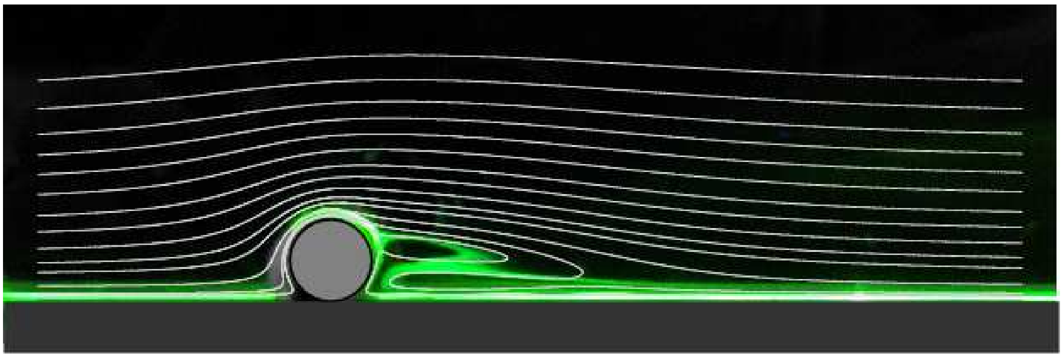

FIGURE 5.8: Comparison of experimental and numerical steady flow at $\alpha - 1$ and $Re = 250$. The experimental streaklines are shown by the green dye and overlaid in light grey are the numerically predicted streamlines.

two-dimensional for longer periods of time. A series of experimental images at $Re = 80$ is given in figure 5.9 for $\alpha = 0$, 0.5 and 1. As mentioned above, the numerically predicted flows at $Re = 80$ were steady for these rotation rates. The dye streaklines can be compared to the vorticity contours at $Re = 90$ for $\alpha = 1$, given in figure 5.9(d) and the similarities in the roll-up and placement of the structures can be seen when compared to figure 5.9(c). From this, it seems that the critical bifurcation curve is shifted to lower Re in the experimental investigation. The experimental formation length of the wake reduces as the rotation rate of the cylinder increases. This is most apparent in figure 5.9(c), where the roll-up of the shed vortex is occurring above and immediately behind the top of the cylinder.

As the rotation rate of the cylinder increases from 0 to 1, the position of the vortices is displaced further from the wall. This is a reflection of the increased vorticity detected in the simulations, which causes the vortex pair to propel further from the wall. In figure 5.9(a), the vortex originating in the wall shear layer is not clearly apparent, and the difficulty associated with the dye injection technique makes visualising the secondary vortex difficult. The forward rotation of the cylinder in figures 5.9(b) and 5.9(c) means that any dye introduced along the belt passes over the top of the cylinder without thoroughly infiltrating the region behind the cylinder and along the wall.

The vortices that are destabilised and form from the wall shear layer are more easily visualised for the cases where $\alpha < 0$, and an example of this is given in figure 5.10(a). For these rotation rates, the dye injected along the belt lifts up with the cylinder rotation and passes onto the cylinder surface. From this point, the dye is carried by the cylinder into the wake region and transferred onto the moving floor. Figure 6.15 shows

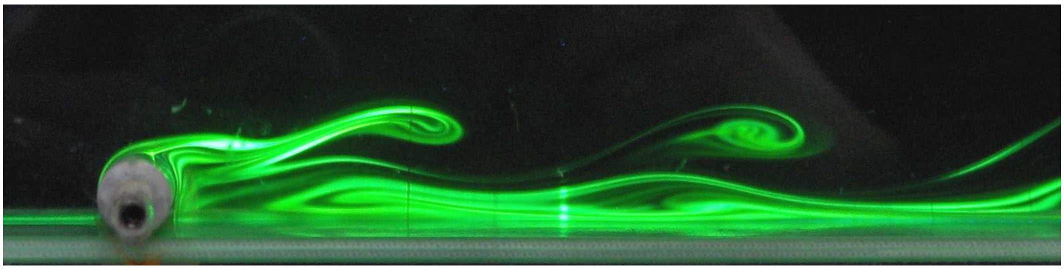

(a) $\alpha = 0$, $Re = 80$.

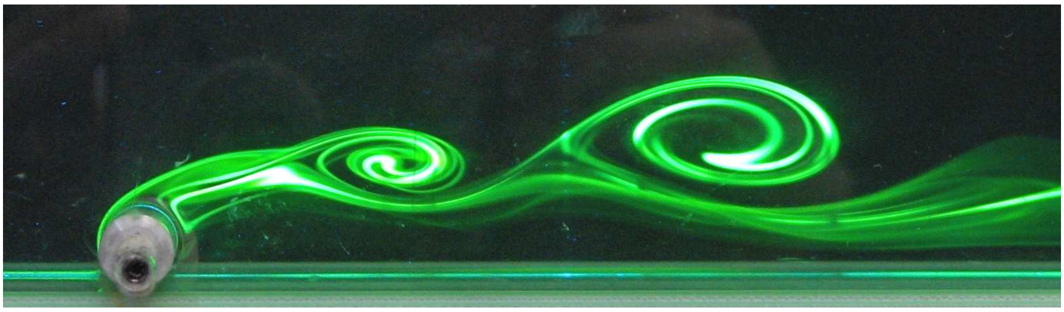

(b) $\alpha = 0.5$, $Re = 80$.

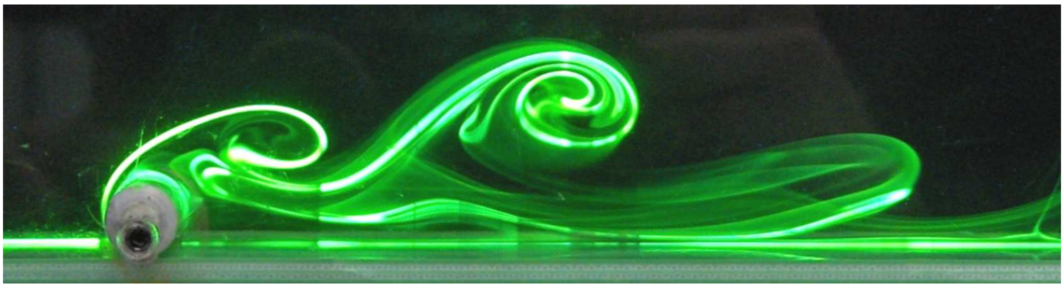

(c) $\alpha = 1$, $Re = 80$.

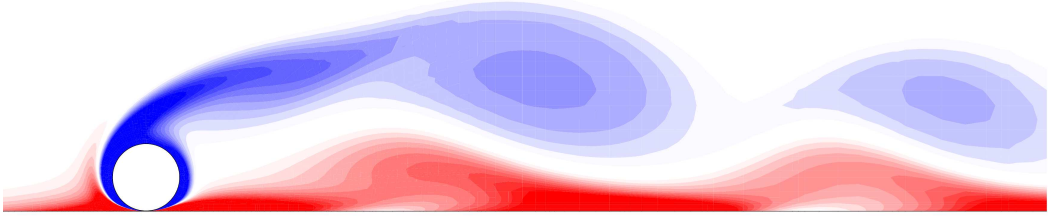

(d) Numerical vorticity contours for $\alpha = 1$, $Re = 90$.

FIGURE 5.9: Results for experimental flow around the cylinder at $Re = 80$ for different rotation rates, α. Also shown is a numerical comparison with $\alpha = 1$ and $Re = 90$. This Reynolds number was near the lower end of the range that was achievable in the water channel.

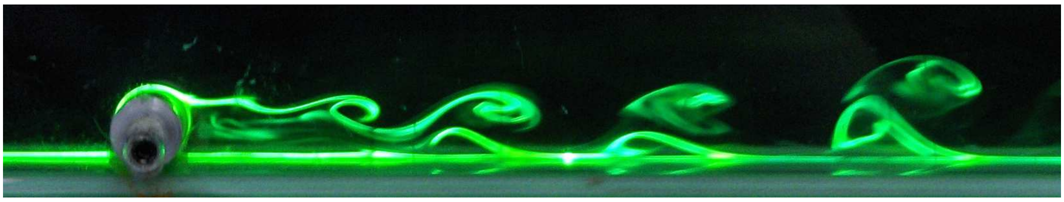

(a) $\alpha = -1$, $Re = 400$.

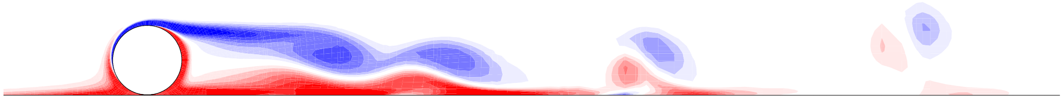

(b) $\alpha = -1$, $Re = 450$.

FIGURE 5.10: Comparison between the experimentally and numerically observed wakes at high Reynolds number with the cylinder undergoing reversed rolling.

the comparison at $\alpha = -1$ between the experimental and numerical unsteady flows. In both images, a series of vortex pairs are shown forming and lifting away from the surface as they are propelled towards the freestream. A net rotation of the vortex pair can also be seen about the upper vortex that is shed from the cylinder. Figure 5.10(a) is shown at $Re = 400$ while figure 5.10(b) is at $Re = 450$. This is due to the fact that the numerical simulations remain steady at $Re = 400$ and a shift in the bifurcation curve is experienced in the experiments, as mentioned previously.

While the experimental setup was found to be better suited to the sphere geometry, where end effects were not so prevalent, results for the flow around the rolling and sliding cylinder serve as a useful comparison with the numerical results. By restricting the results to the initial start up flow, in which three-dimensionality is not fully developed, it is possible to generate a series of images showing the two-dimensional experimental flow. A reasonable qualitative agreement exists in the structures observed in the wake, although the transition to unsteady flow occurs at Reynolds numbers below those predicted in the simulations. This is attributed to perturbations and three-dimensional effects in the flow from the side walls.

5.5 Chapter summary

From the linear stability analysis, it was discovered that the wake behind the rolling cylinder undergoes a transition to steady three-dimensional flow, prior to the onset of unsteady flow. This has similarities to the flow behind a backward-facing step and similarities also exist in the structure of the wake. The three-dimensional structure takes the form of flattened rolls within the recirculation zones of the two-dimensional base flow and the spanwise wavelength of this mode is strongly dependent on the rotation rate of the cylinder. The structure of this time invariant perturbation mode was also verified with the use of three dimensional simulations.

The growth rates of the three-dimensional mode was calculated for a range of wavelengths and the critical wavelength and Reynolds number was determined for each rotation rate. A point of interest is that, for several of the rotation rates studied, the three-dimensional mode first appears at the same Reynolds number as the lower recirculation zone in the two-dimensional simulations of chapter 4.

Extension of the stability analysis to a Floquet analysis of the unsteady base flow presents the possibility of complex, or quasi-periodic modes, that may develop at higher Reynolds numbers. This is a finding that encourages further analysis of the structure of the three-dimensional mode when the flow is time dependent.

It is considered likely that the three-dimensional mode develops as the result of a centrifugal instability in the flow. Towards this end, calculations were carried out on the closed streamlines of the upper and lower recirculation zones to determine if Rayleigh's criterion is satisfied. However, the circulation was found to be always outwardly increasing and the findings indicate that a centrifugal instability does not develop within the recirculation zones. This does not preclude the possibility of a local centrifugal instability, which is still possible in the region of flow characterised by open streamlines, either near the cylinder surface or adjacent to the lower wall.

A series of experiments were carried out in the water channel to verify the structure of the wake behind the cylinder. The relatively small aspect ratio of the cylinder presented some difficulties with the development of end effects. This problem was overcome by considering the initial start-up flow, before the three-dimensional end effects have time to saturate the flow. The result is a good qualitative agreement between the predicted two-dimensional flow and the experimental streaklines. This was particularly apparent with the placement of the two recirculation zones in the steady flow regime, and the vortex shedding in the unsteady regime. The cylinder shear layer was observed to roll up and destabilise the wall shear layer, resulting in the formation of a vortex pair, as predicted by the numerical simulations. These findings indicate that useful information may be obtained from the two-dimensional simulations about the large scale physical structures in the wake, even when the flow is known to be three-dimensional.

Chapter 6

The rolling sphere

Previous studies of sedimenting particles near a wall have reported that spherical bodies may experience fluid forces that exert a moment, causing them to rotate (Hu & Joseph 1999; Humphrey & Murata 1992; Goldman *et al.* 1967a). Experimental work by Liu *et al.* (1993) found that small spheres dropped down an inclined channel could be forced into a reversed rotation by the hydrodynamic forces acing on the body. Similarly, three-dimensional numerical simulations by Zeng *et al.* (2005) observed a net rotation of a particle when moving through a still fluid at various distances from a wall. In the latter study, a limited number of flow visualizations were presented, when the distance between the sphere and the wall was equal to $0.5D$, and both steady and unsteady modes were observed. In order to understand more fully the flow structures that form in this configuration, this chapter examines the wake of a sphere as it is undergoing various rates of rotation, while adjacent to a plane wall.

During this investigation, stable wake modes are observed, the structure of which is strongly dependent on the imposed rotation rate of the body. As the sphere undergoes forward rolling, a wake mode is observed which bears similarities to the flow behind an isolated sphere in a free stream. As the Reynolds number of the flow is increased, hairpin vortices form and are shed over the surface of the sphere. However, for cases with reversed rotation of the sphere, the wake takes the form of two distinct streamwise vortices that form around the sides of the body. As the Reynolds number increases, this wake undergoes a transition to a previously unreported unsteady mode that displays an antisymmetric structure.

The following chapter also presents results of simulations of the steady and unsteady sphere flows, predicted using the three-dimensional code described in section 2.1. The vortical structures occurring in the wake have been visualised using the method defined by Jeong & Hussain (1995). This method uses the eigenvalues of the tensor constructed from the symmetric and antisymmetric parts of the velocity gradient tensor. It has been shown by Jeong & Hussain (1995) to capture the positions of vortex cores in low Reynolds number flow. The advantage of this method is that it is capable of identifying the structure of the vortex cores when they are deforming and are not oriented along a single axis (as is the case during the shedding of hairpin vortices behind the sphere). From the simulations, much additional information is gained regarding the fine structures in the wake.

When investigating the unsteady flow regimes numerically, it can be useful to add white noise of magnitude 10^{-3} to the velocity field (normalised with respect to the freestream) to expedite the growth of the unsteady modes. Without this, it may be necessary to wait for the growth of numerical round-off errors to bring about the same transition, which can increase the computation time substantially. Throughout this chapter, the instances in which this technique have been used shall be clearly identified.

Experimental results are reported for the Reynolds number range $100 < Re < 350$, and the experimental setup is as described in section 3.1. The rotation rate of the sphere, α, is defined in the same way as for the cylinder.

6.1 Flow regimes and transitions

For the five rotation rates specified, the experimental study of the parameter space indicates the regions in which the different wake modes occur. This transition diagram is shown in figure 6.1, with the steady modes shown as open symbols. The transition to unsteady flow (closed symbols) is shown as Re increases. It is expected that the Re thresholds for instability experiences slight variations due to the presence of the supporting rod in the experiments and that the value of the transition Reynolds numbers will vary in the simulations. The solid lines of figure 6.1 represent the mode limits determined visually from recordings of the dye patterns and the dashed vertical line in figure 6.1 indicates a generalised boundary between the experimentally observed wake modes at $\alpha \leq 0$ and $\alpha > 0$. The reason for classifying the steady flow as two separate modes is related to the experimental observation of two distinct streamwise vortices that develop in the flow for $\alpha \leq 0$. Experimentally, these structures could not be observed for $\alpha > 0$. However, the numerical simulations undertaken at a later date indicate that these steady modes may be more closely connected than originally thought, and the transition between them is discussed in section 6.3.3.

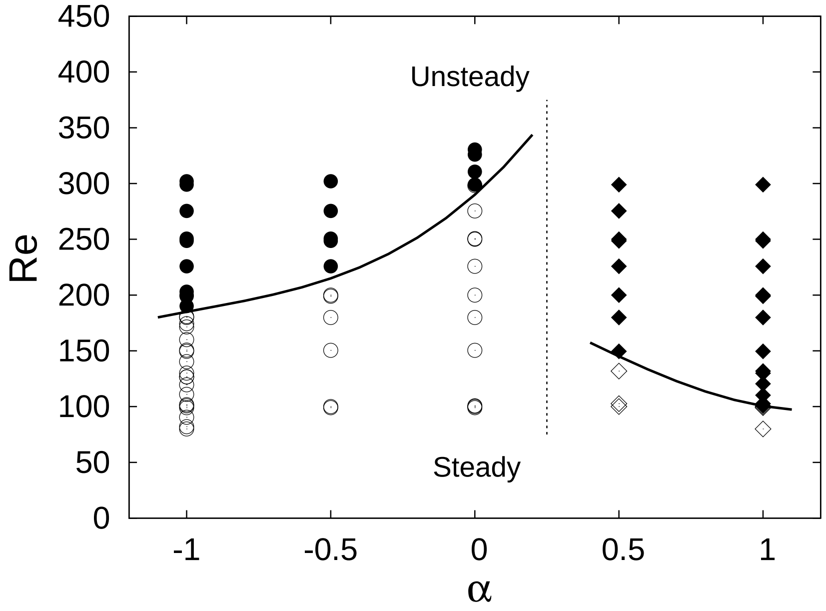

FIGURE 6.1: Transition map of the four different wake modes observed in experiments. Closed symbols indicate unsteady modes and open symbols denote steady modes. The steady wake mode for $\alpha > 0$, and the corresponding unsteady mode displaying the shedding of hairpin vortices, are given by ◊ and ♦, respectively. Alternatively, the steady mode for $\alpha \leq 0$, comprising of counter-rotating streamwise vortices and the associated antisymmetric mode are given by ∘ and •, respectively.

The mode occurring for $\alpha > 0$ is found to be the least stable, with a transition to unsteady flow occurring at $Re \approx 100$ for $\alpha = 1$. A change in the unsteady wake mode occurs for $0 < \alpha < 0.5$, and the antisymmetric wake becomes apparent. For the sliding sphere with $\alpha = 0$, the transition to unsteady flow is observed experimentally at Re above 300. This finding has some support from the work of Zeng *et al.* (2005), who found that steady flow occurs at $Re = 300$ for a wall distance of $0.25D$. In contrast, the sphere in a freestream flow undergoes a transition to unsteady flow at $Re \approx 270$ (Thompson *et al.* 2001a). For the larger magnitude, negative values of α, the transition Re reduces to $Re \approx 185$ for $\alpha = -1$. Throughout the remainder of this chapter each of the observed modes, and the transitions between them, shall be discussed in detail.

6.2 Steady flow

At the five values of α studied in the experiments, the steady wake appears to take two different forms, depending on the rotation rate of the sphere. Examples of these modes are shown in figure 6.2 and different structures in the wake can be explained in terms of the relative motion between the sphere and the freestream. For $\alpha = 1$ and 0.5, the motion of the upper half of the sphere opposes the direction of the freestream flow. This opposing motion creates high vorticity and a zone of recirculating fluid located over the top of the sphere. In addition, the fluid passing around the sides of the sphere moves into the low pressure region behind the body and into this recirculation zone. The resulting compact region of recirculating fluid is seen from above in figure 6.2(a) and the visible surface of the sphere is moving from right to left. The dye escapes this recirculation zone via a single 'tail', along the centreline of the body. It is expected that both positive and negative streamwise vorticity are present in this tail but are not clearly shown by the dye streaklines. The flow image shown in figure 6.2(a) bears similarities to the symmetry-breaking wake observed for the isolated sphere that occurs for $Re > 210$ (Johnson & Patel 1999; Ghidersa & Dušek 2000). However, during the experiments, the presence of the wall appears to suppress the double-tailed wake that is generally observed in unbounded flow.

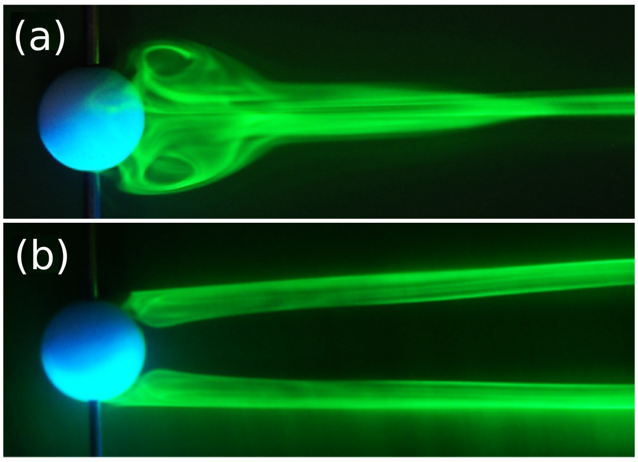

Figure 6.2: Steady wake flows at $Re = 100$ behind (a) the forward rolling sphere with $\alpha = 0.5$ and (b) reversed rotation with $\alpha = -0.5$.

For reversed rolling at $\alpha = -0.5$ and -1, the upper surface of the sphere is moving in the same direction as the freestream fluid (left to right) and no recirculation zone forms around the body. When one considers flow in the vertical centreplane of the sphere, the upstream fluid is free to move over the sphere surface and reattach to the moving floor in a relatively undisturbed fashion, thus preventing the formation of a recirculation zone. Instead, the reversed rotation wake shows a markedly different structure, in which the curvature of the sphere and the nearby moving wall cause the roll-up of fluid around the sides of the body, which forms a counter-rotating, streamwise vortex pair. For the wake shown in figure 6.2(b), the vorticity in the streamwise direction of the lower vortex is negative and that of the upper vortex is positive. This pair of vortices has an induced motion towards the wall (as described by Ersoy & Walker (1985)) and once there, the distance between the two vortices increases as they progress downstream.

When considering the steady flow for $\alpha > 0$, the simulations offer greater insight into the structure of the wake than is available from the experimental dye visualisations alone. Examples of the steady wake obtained using numerical simulations are given in figure 6.3 for $\alpha = 1$, and two different values of Re. From the numerical simulations it is clear that two low strength streamwise vortices are formed in the wake of the forward rolling sphere. This is reminiscent of the two-tailed wake forming behind the sphere in unbounded flow. This structure is not apparent in the experimental results of figure 6.2(a), where the streaklines of dye appear to merge into a single structure downstream of the recirculation zone.

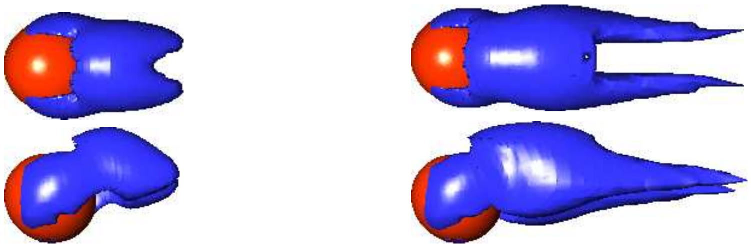

(a) $Re = 50$.

(b) $Re = 100$.

FIGURE 6.3: The structures in the wake of the forward rolling sphere as determined numerically. Surface contours of the eigenvalue proposed by Jeong & Hussain (1995) are shown from above (upper images) and from the side (lower images). The rotation rate is held fixed at $\alpha = 1$, and increasing the Reynolds number of the flow increases the strength of the streamwise vortices in the wake.

The two-tailed structure in figure 6.3 initially forms at low Re and early signs of this structure are apparent in the view from above in figure 6.3(a). As the Reynolds number of the flow increases, these streamwise vortices and the recirculation zone immediately behind the sphere increase in strength. The vorticity forms at the sides of the sphere surface at the same location for both Reynolds numbers shown. This vorticity is then contained in the near-wake region behind the forward rolling sphere. The motion of the sphere and surrounding fluid act to displace this region of vorticity away from the wall.

Almost identical structures to those of figure 6.3 were observed by Zeng *et al.* (2005) in their study of the translating sphere near a wall. With a gap ratio of $0.5D$ and no sphere rotation, they found the bifurcation to this mode to occur at $Re < 50$. Also observed in their study was an increase in the length of the vortices with increasing Re. By inspection, the two tailed mode observed by Zeng *et al.* (2005) and the one reported in the present study appear to be the same; however, the absence of rotation and a much larger gap ratio mean that their wake region is positioned closer to the wall and does not display the same degree of asymmetry as that in figure 6.3.

When the sphere is undergoing reversed rolling, the streamwise vortices that form in the wake are much stronger and more clearly defined than when $\alpha > 0$. This was shown by the dye visualisation in figure 6.2(b), and the corresponding steady wake from the numerical simulations is shown in figure 6.4. The two streamwise vortices are formed following the roll-up of vorticity generated at the front and sides of the sphere. There is no interaction of these two vortices behind the body and the wall-normal centreplane of the sphere shows a region of largely undisturbed flow. This is in very good agreement with the experimentally observed flow structures in figure 6.2(b).

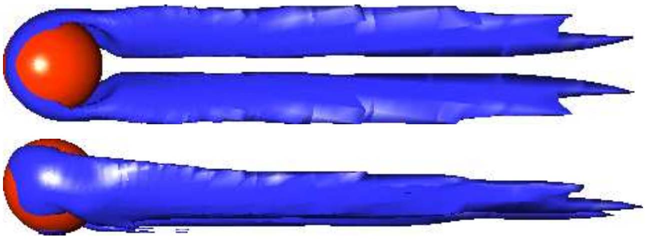

FIGURE 6.4: Numerical results for the sphere wake at $Re = 100$ and $\alpha = -1$. The iso-surfaces are as defined for figure 6.3. The structure in the wake shows that the formation of two streamwise vortices initially takes place at the front and sides of the sphere.

The structure present behind the sphere at $\alpha = 0$, both from experiments and numerical simulations, is shown in figure 6.5. In this case, the wake has similarities to both of the steady flow images shown in figure 6.2, with a recirculation region behind the body and two distinct streamwise vortices being present. The experimental dye visualisation of figure 6.5(a) was obtained by placing a laser sheet parallel to the floor at a distance of $0.5D$. At $Re = 200$, the flow around the stationary sphere forms a recirculation region immediately behind the body, leading to the appearance of two zones of recirculating fluid in the plane parallel to the moving wall and on either side of the sphere. This type of structure can be observed in figure 6.2(a) but not figure 6.2(b).

However, further downstream, this recirculation zone develops into a counter rotating streamwise vortex pair, as observed for $\alpha < 0$. The numerical results of figure 6.5(b) show a similar picture but in this instance, the structures are confined closer to the rear of the sphere, in the near wake. Although vorticity is generated over the entire sphere surface, this only rolls up at the back of the sphere, where it develops into a streamwise pair of vortices that separate slightly as they travel downstream, while remaining very close to the plane wall. As the magnitude of reversed rolling decreases towards zero, the formation of the streamwise vortices moves from the sides of the sphere (as in figure 6.4), towards the rear. This is in contrast to the dye streaklines of figure 6.5(a), which show a more widely spaced recirculation zone.

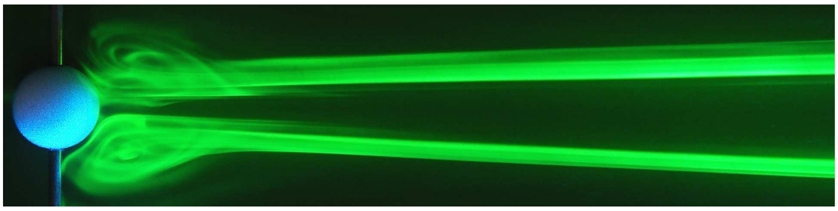

(a) Experimental dye visualisation.

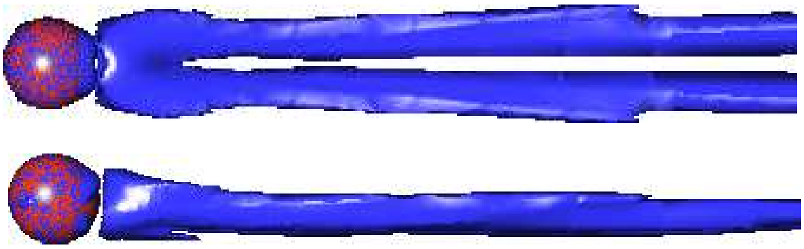

(b) Numerical simulations showing the steady wake from above and from the side.

FIGURE 6.5: The steady wake behind the non-rotating sphere at $Re = 200$, showing (a) experimental dye visualisations and (b) numerical surfaces of the eigenvalue proposed by Jeong & Hussain (1995). This wake has similarities to those occurring behind the sphere during both forward and reverse rolling.

The absence of sphere rotation in figure 6.5 means that the strength of the recirculation zone and the resulting streamwise structures are much weaker than for $\alpha \neq 0$ at a corresponding Reynolds number. At $Re = 200$, shown in figure 6.5, the vortices are regular and steady, and remain this way until much higher Re. During the numerical simulations for $\alpha = 0$, a streamwise vortex pair is present at $Re = 300$, which remains steady and symmetric, even following the introduction of a random perturbation to the flow. This is in contrast to the experiments, which show the first signs of an unsteady oscillation as Re increases above 300. The large Reynolds number range in which steady flow occurs for $\alpha = 0$ supports the experimental results shown in the transition diagram of figure 6.1; that the $\alpha = 0$ wake is the most stable. This is unlike the flow around the rolling cylinder, in which $\alpha = -1$ provides the most stable configuration.

6.3 Unsteady wake modes

As Re increases, the wake experiences a transition to unsteady flow. Again the structures in the wake are dependent on the rotation rate, and two distinct unsteady modes are observed. For the cases of $\alpha > 0$, the recirculation zone behind the sphere undergoes a transition with increasing Re and vortex shedding begins. This takes the form of hairpin vortices, as for the isolated sphere, and an example of the wake is shown in figure 6.6(a). Unlike for the sphere in an unbounded flow, the proximity of the moving wall fixes the orientation of the wake, with the hairpin vortices forming over the top of the sphere and tilting away from the wall as they move downstream. The sense of rotation of the hairpin vortices is the same as that described by Achenbach (1975) for the vortex shedding from an isolated sphere.

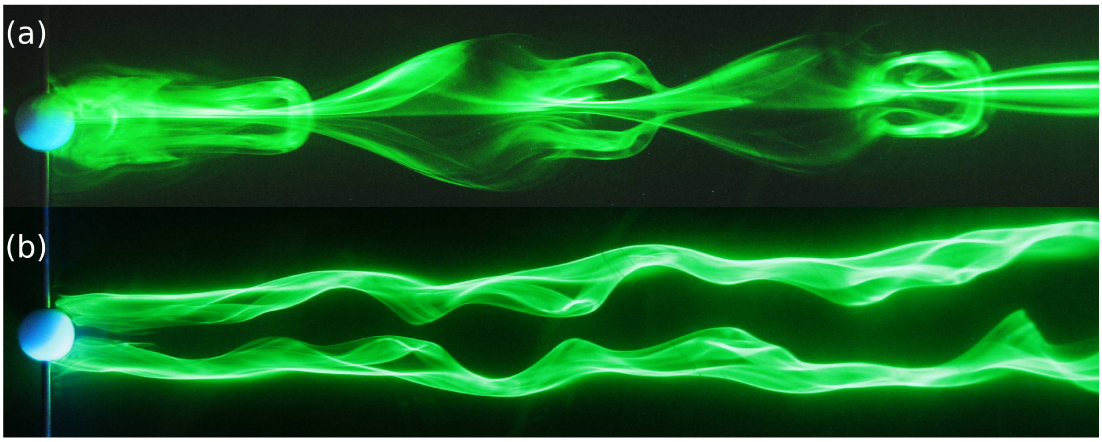

FIGURE 6.6: Unsteady wake flows at $Re = 200$ behind (a) the forward rolling sphere with $\alpha = 1$, showing the shedding of hairpin vortices, and (b) the reversed rolling sphere with $\alpha = -1$, in which a transverse motion of the streawise vortices is present.

For $\alpha \leq 0$, the wake experiences a very different transition, as shown in figure 6.6(b). Here, the counter-rotating streamwise vortices maintain the same sense of rotation as for the steady flow but as Re increases, the vortices increase in size and strength. At a critical Re, they begin to interact behind the body, causing an antisymmetric oscillation of the wake in the transverse direction. For $\alpha = 0$, the steady mode extends to much higher Re before the vortices begin to interact. Only at the upper range of Re considered in the experiments is an unsteadiness observed for $\alpha = 0$. This takes the form of a sinuous oscillation of the wake as it travels downstream and bears similarities to the initial onset of unsteady flow for $\alpha < 0$. Consequently, it is assumed that the same type of instability is observed for all $\alpha \leq 0$. This mode appears to be less sensitive to small perturbations in the experimental flow than when $\alpha > 0$, indicating that a different mechanism may be responsible for the transition to unsteady flow.

The mode occurring for $\alpha > 0$ maintains a plane of symmetry that passes through the sphere centre, perpendicular to the wall. This mode shall therefore be referred to as the symmetric wake mode. The wake mode for $\alpha \leq 0$ is very different in structure, and in figure 6.6 it is not clear what, if any, symmetry exists in the wake. This question is answered experimentally by placing a laser sheet in the plane parallel to the wall at a distance of $0.5D$. The result is given in figure 6.7 for the unsteady modes observed.

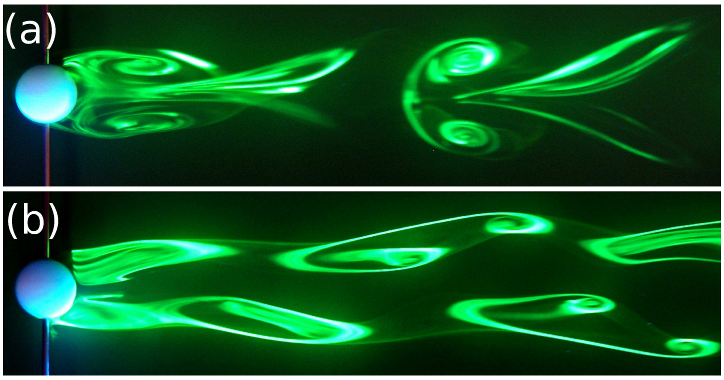

FIGURE 6.7: The symmetry modes obtained by cutting the wake with a laser sheet positioned parallel to the moving floor at a height of $0.5D$. Images are given at $Re = 200$ for (a) $\alpha = 1$ and (b) $\alpha = -1$.

The visualisations of figure 6.7 clearly show the planar symmetry present for the unsteady wake with $\alpha > 0$. Figure 6.7(a) shows sections through two of the hairpin vortices that have formed over the top of the sphere. These are distinguishable by the vortex pairs downstream of the sphere and in the near-wake. What is also shown in figure 6.7 is that the unsteady mode occurring for $\alpha \leq 0$ has a clearly organised antisymmetric form. The top half of the wake in figure 6.7(b) can be obtained by reflecting the bottom half of the wake along the centreline and introducing a phase shift of half a period. This mode will therefore be referred to as the antisymmetric mode from this point forward. Figure 6.7(b) also hints at the fully developed three-dimensional nature of the wake that shall be discussed later.

6.3.1 The symmetric mode

Images of the experimental wake show development of the unsteady mode for $\alpha = 1$ at $Re = 100$. This wake is shown from the side in figure 6.8 and is very near the critical Reynolds number at which the unsteady mode first develops. At this Reynolds number, the shedding appears intermittently, and near the Re threshold for instability, the wake is easily perturbed by any irregularities in the sphere motion or the channel flow.

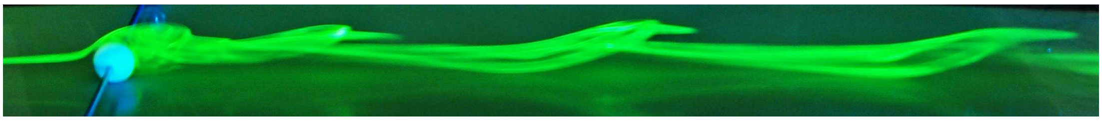

FIGURE 6.8: Initial onset of the unsteady wake flow at $Re = 100$ and $\alpha = 1$. Weak hairpin vortices are shed in the wake of the sphere and remain close to the wall as they are carried downstream.

The hairpin vortices being shed in figure 6.8 have a streamwise wavelength somewhat greater than that of the fully developed wake mode at higher Re. The strength of vorticity in the wake is also relatively weak and the hairpin vortices remain close to the wall as they travel downstream. As the Reynolds number of the flow increases, the strength of the vortices increases, and they orient themselves toward the wall-normal direction as they progress downstream. The fully developed wake mode obtained both experimentally and numerically at $Re = 200$ is shown in simultaneous views from the top and the side in figure 6.9. The orientation of the hairpin vortices in figure 6.9 is similar to that for the sphere in unbounded flow (Leweke *et al.* 1999; Achenbach 1975). In the study by Zeng *et al.* (2005) for the translating sphere with wall separations down to $0.25D$, the shedding of weak hairpin vortices is observed. As for the present study, they find that the presence of the wall fixes the orientation of the wake so that the symmetry plane is normal to the wall.

The unsteady symmetric wake of figure 6.9(b) develops when the numerical simulations are started impulsively from rest with no additional perturbation, and the structures in the wake show a good agreement with the experimental flow. Figure 6.10(a) and (b) shows the numerical results obtained by Johnson & Patel (1999) for the shedding behind a sphere in a freestream and the results of Zeng *et al.* (2005) for the sphere moving through a still fluid above a plane wall. By comparing the wake of figure 6.9(b) and that of Johnson & Patel (1999) in figure 6.10(a), similarities can be seen in the position and structure of vortex loops. Views from the side show that the

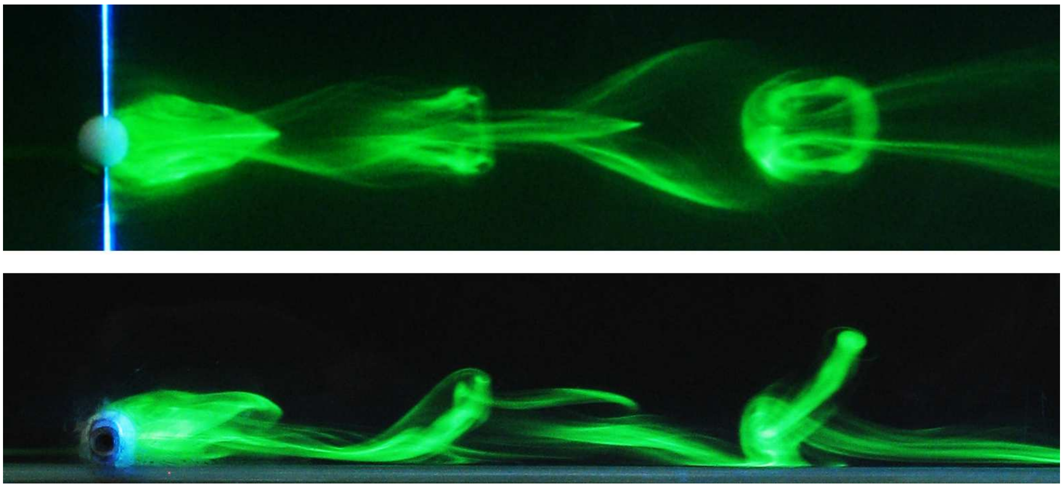

(a) Experimental dye visualisation.

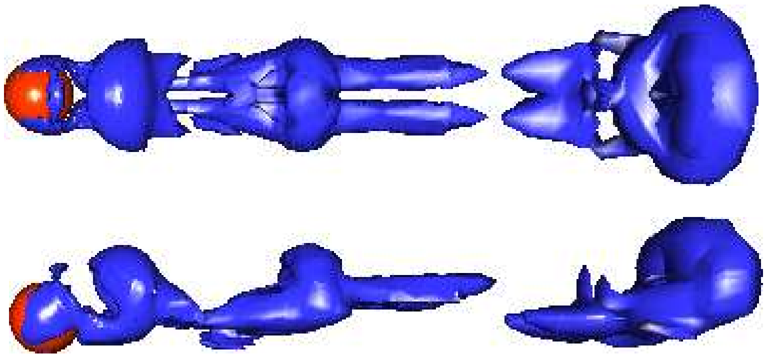

(b) Iso-surface of the eigenvalue proposed by Jeong & Hussain (1995).

FIGURE 6.9: Simultaneous wake images at $Re = 200$ with $\alpha = 1$. The views in each case are from above (top) and from the side (bottom).

presence of the wall suppresses the structures that would normally form on the lower side of the wake.

The wake image in figure 6.10(b) for the sphere near the wall is somewhat different to that of figures 6.9(b) and 6.10(a). The difference may be partly due to the method used to calculate the surfaces of vorticity. The study of Johnson & Patel (1999) used the method defined by Jeong & Hussain (1995) to calculate contours of vorticity (as in the present study), while the structures shown in figure 6.10(b) represent a swirling strength, as calculated from the imaginary part of the complex eigenvalue of the velocity gradient tensor. Figure 6.10(b) is similar to the wake in the present study as regards the placement of the wake along the wall. However, the strength of the hairpin vortices appears to be much weaker and the vortex loops are not fully formed.

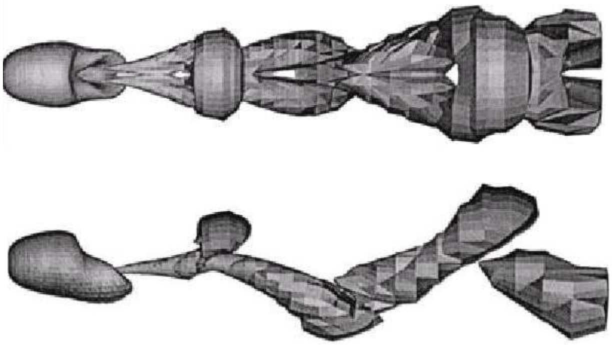

(a) Sphere in unbounded flow at $Re = 300$.

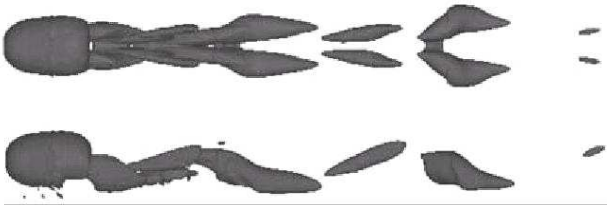

(b) Sphere moving $0.5D$ above the wall at $Re = 300$.

FIGURE 6.10: Wake comparison between (a) the non-rotating sphere in an unbounded flow, taken from Johnson & Patel (1999), and (b) the translating sphere at a distance of $0.5D$ from the wall, taken from Zeng *et al.* (2005).

Due to the similarities in the wake between the present case and the sphere in an unbounded flow, it is possible that the two configurations undergo Hopf bifurcations through the action of the same mechanism. However, the mechanism that brings about the transition in the unbounded flow has still not been clearly identified. When no wall is present, the steady asymmetric two-tailed wake appears prior to the onset of unsteady flow and several studies have reported that these tails begin to undulate prior to vortex shedding (Taneda 1956a; Magarvey & Bishop 1961a; Sakamoto & Haniu 1995; Ormières & Provansal 1999). Schouveiler & Provansal (2002) propose this as a possible transition mechanism. Conversely, Sakamoto & Haniu (1995) propose a mechanism whereby the region of fluid behind the sphere becomes unstable and causes the vortex forming over the top of the sphere to detach, resulting in the formation of a hairpin vortex. This offers a more feasible explanation for the bifurcation observed in the present study, where a periodic growth and collapse of the recirculation zone is observed.

Figure 6.11 shows the near-wake behind the sphere at $Re = 200$, rotating with $\alpha = 1$. The series of 10 images are taken 0.5 seconds apart. The formation and detachment of a hairpin vortex is seen from above. In images 1 and 2 of figure 6.11, the recirculation zone behind the sphere is growing in size. In image 3, the roll-up of the shear layer can be noticed and the recirculation zone becomes more compact. In images 4 to 5, the shear layer continues to roll up and form a vortex tube, which then detaches from the main recirculation zone. This hairpin vortex is carried downstream in images 6 to 10. The structure and the 'legs' of the hairpin vortex become clear as it separates fully from the near-wake recirculating flow. The near wake in image 9 closely resembles that in image 1, indicating that slightly more than one period has been covered by the sequence. This series of images shows the typical expansion and contraction of the recirculation zone during the vortex shedding process.

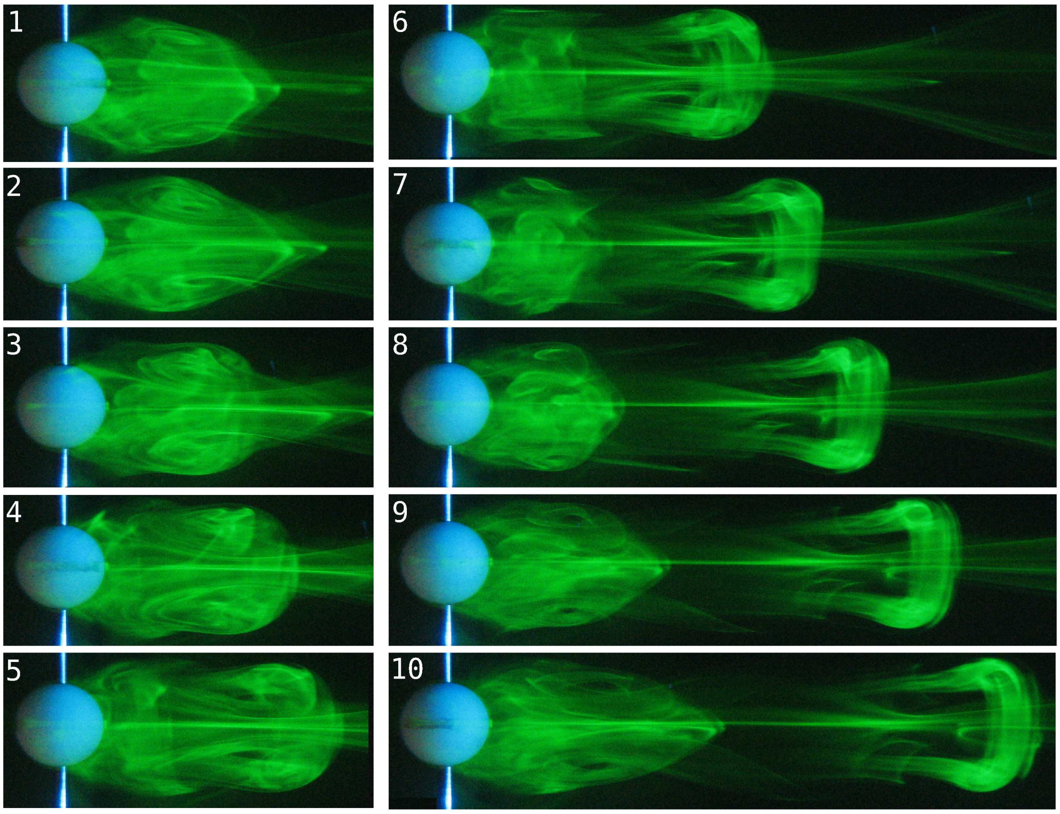

FIGURE 6.11: Steady wake flow at $Re = 200$ with $\alpha = 1$.

6.3.2 The antisymmetric mode

The antisymmetric wake mode for $\alpha < 0$ first appears as a transverse undulation in the wake, similar to that observed behind a freely falling sphere in an unbounded flow (Magarvey & Bishop 1961a). This is at Reynolds numbers just above the onset of unsteady flow and an example is shown in figure 6.12 for $\alpha = 0$ at $Re = 330$. Initially, this transverse oscillation appears to remain in a plane parallel to the moving floor, but as Re increases further beyond the transition, an out of plane component becomes visible. As mentioned earlier, the wake for $\alpha = 0$ remains steady over a large range of Re and it is only at the upper limit achievable in the water channel that unsteady flow, of the type shown in figure 6.12, is observed. Consequently, at $\alpha = 0$, it is not possible to obtain the regular three-dimensional wake that is observed for $\alpha = -0.5$ and -1.

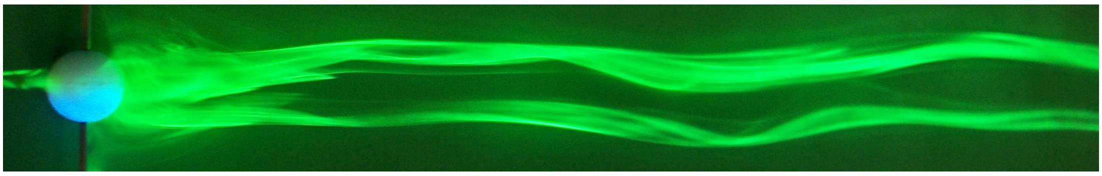

Figure 6.12: Undulating wake flow at $Re = 330$ with $\alpha = 0$. This motion in the wake is observed at Reynolds numbers just above the onset of unsteady flow for the antisymmetric mode.

During the numerical simulations at higher Re, the unsteady antisymmetric wake mode develops following the introduction of random noise to the solution. At lower Re, the introduction of random noise to the flow has no overall effect, and any perturbation in the flow decays rapidly to the steady solution. At higher Re, following this perturbation, the unsteady mode develops and converges to a regular periodic wake. Figure 6.13 shows the two wake modes obtained during simulations at $Re = 200$, both with and without this perturbation to the flow. When the simulations are allowed to develop naturally, the flow remains symmetric and steady, as shown in figure 6.13(a). This represents an unstable solution, and the addition of random noise to the velocity field results in the development of the unsteady mode given in figure 6.13(b). The introduction of random noise provides a solution that more closely approximates that observed in experiments, where low level background turbulence is unavoidable. The position of the vortical structures at the front and sides of the sphere does not change in the two images. It is only in the near wake that the disturbance of the vortices in the periodic wake becomes apparent.

While the wake of figure 6.13(b) has lost its symmetry, the deformation over time is still relatively small and the major motion of the streamwise vortices lies in a plane parallel to the wall. This is in agreement with the experimentally observed development of the antisymmetric mode shown in figure 6.12, at a Reynolds number just above the bifurcation. The simulations indicate that the sinuous motion of the wake results in a net transverse force on the sphere. The coefficient of this cross-stream forces is defined in the same manner as for the lift and drag forces, and shall be referred to henceforth

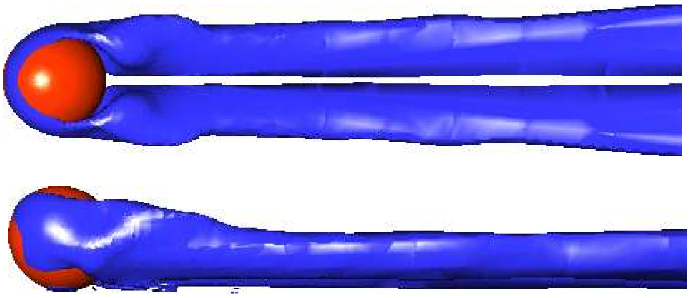

(a) Steady wake at $Re = 200$.

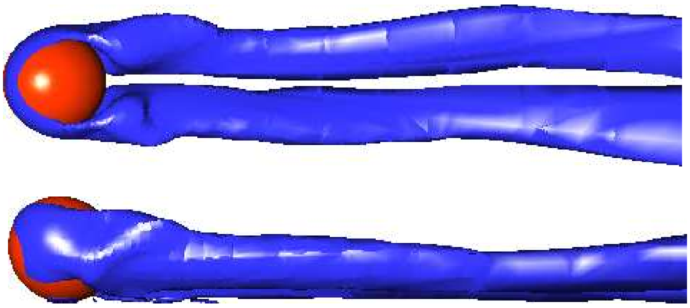

(b) Antisymmetric wake after a perturbation has been introduced.

FIGURE 6.13: The steady and sinuous wake modes observed at $\alpha = -1$ and $Re = 200$. The plotted iso-surface is as per figure 6.3.

as C_Z.

As the Reynolds number increases in the unsteady regime, the streamwise vortices on either side of the wake interact to a greater extent, and alternating sides of the wake lift away from the wall. This movement of the wake is observable at lower Re in the experiments than in the numerical simulations. At $Re = 200$, the experimental flow visualisation of figure 6.14 shows the increased irregularity of the wake when viewed simultaneously from above and from the side. As the streamwise vortex on one side of the wake is lifted away from the floor, a motion is induced in the opposite vortex, pulling it along the floor and toward the wake centreline. This motion produces an apparent narrowing of the wake (when viewed from above), that can be seen in the top image of figure 6.14. This corresponds to an increased vertical displacement between the two vortices. The peaks observable in the lower image of figure 6.14 correspond to alternating sides of the wake.

In the present study, the unsteadiness present in the antisymmetric mode develops in the near wake immediately behind the sphere. The interaction of the two streamwise vortices can be detected by positioning a vertical laser sheet several diameters behind

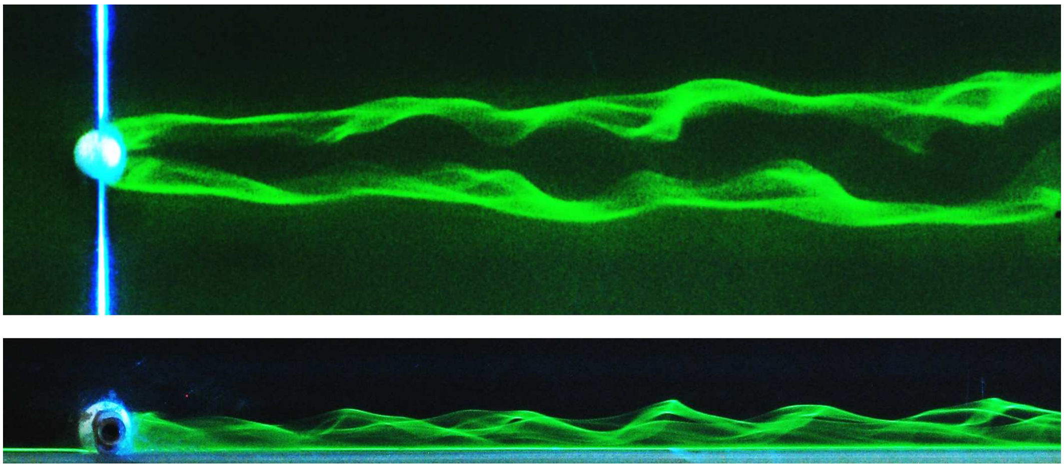

FIGURE 6.14: Simultaneous wake images of the antisymmetric mode at $Re = 200$ with $\alpha = -1$. View is from above (top) and from the side (bottom).

the sphere. Examples of this are given in figure 6.15 for both the steady and unsteady regimes at $\alpha = -1$. The laser sheet is oriented cross-stream and shows the cross-sectional view of the streamwise vortex cores. Figure 6.15(a) shows the time-invariant mode at $Re = 100$, which maintains a planar symmetry, with the vortex cores being near-circular. An instantaneous shot of the unsteady antisymmetric wake is shown in figure 6.15(b) and the planar symmetry has clearly been lost. The vortex on the left is displaced away from the wall and that on the right is moving towards the wall. This motion changes direction every half cycle.

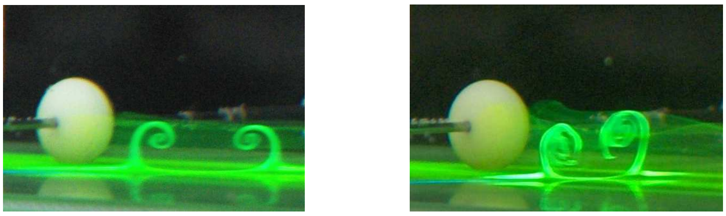

(a) $Re = 100$.

(b) $Re = 200$.

FIGURE 6.15: Dye visualisations through the cross section of the vortex cores during the (a) steady and (b) unsteady flow regimes for $\alpha = -1$. The instantaneous displacement of the vortices are shown in (b).

From potential flow theory the two streamwise vortices near a wall can be considered as part of a four vortex system. The two visible vortices have an induced motion from each other, as well as from the effect of their image vortices located on the wall. Such systems have been analysed in the wake of aircraft and have been found to lead to a range of possible instabilities with various wavelengths (Crouch 1997; Fabre *et al.* 2002;

Jacquin *et al.* 2003).

Following observations of the vortex motion in a plane perpendicular to the wall, it is concluded that the streamwise vortices do not remain oriented in a single, inclined plane. Rather, they appear to form a set of spiral vortices. This is illustrated more clearly by the section view of the wake given in figure 6.16. The dashed lines indicate the paths of the vortex cores when viewed from above and the antisymmetric, sinuous motion of the wake is clear from this angle. Note that the regions of the wake structures that lie in the plane illuminated with the laser sheet occur at the points of maximum lateral displacement for each of the vortices.

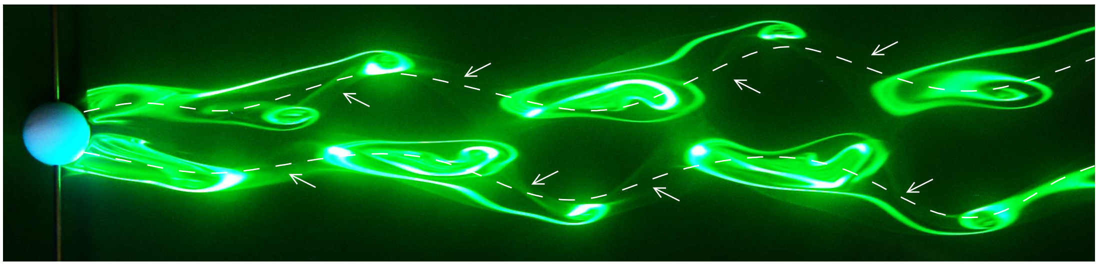

FIGURE 6.16: Visualisation of the wake symmetry at $\alpha = -1$ and $Re = 250$. The laser light sheet is placed parallel to the wall at a distance of $0.5D$. The dashed lined indicate the paths of the vortex cores as viewed from above and the arrows indicate regions of the vortices with the greatest out-of-plane component.

The laser sheet in figure 6.16 is positioned a distance of $0.5D$ from the wall, representing the approximate mid-plane of the wake. In this way, the regions of the wake with the greatest out-of-plane component will not be illuminated and show up as dark regions or 'gaps' in the image, which have been indicated with arrows. These regions of out-of-plane displacement occur near the mid-point between greatest lateral displacements, as is the case for a spiral. Furthermore, from observations of the vortex motion it is apparent that alternating sides of the wake lift away from the wall. This fact, in conjunction with the sinuous motion observed from above, leads to the conclusion that the wake is composed of two spiral vortices that wind in opposite directions and are out of phase by half a wavelength.

When the Reynolds number of the flow is increased during the numerical simulations for $\alpha = -1$, an interesting observation is made. The flow undergoes a bifurcation to an unstable solution branch which is not detected in the experiments. When allowed to develop in the absence of any noise, the reversed rolling wake develops into an unsteady symmetric mode. Even when this wake is fully developed, the introduction of a small

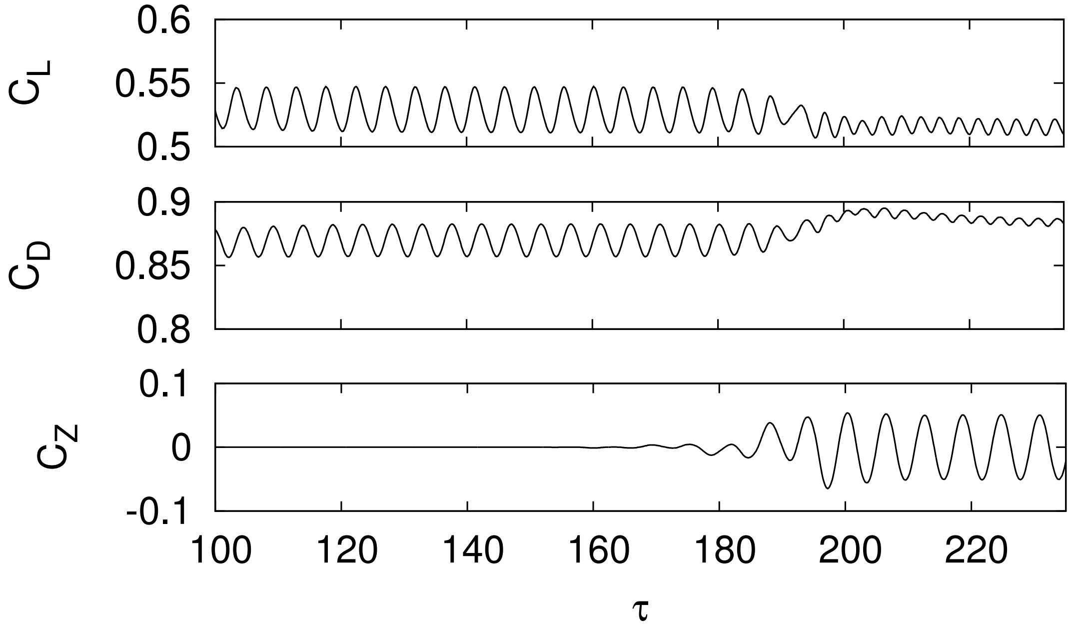

FIGURE 6.17: Lift, drag and transverse force-time histories for $\alpha = -1$, $Re = 300$.

perturbation is enough to cause the transition to the antisymmetric mode observed in experiments. An indication of the growth of this mode is given by the force-time histories in figure 6.17 for $Re = 300$. A small perturbation is added to the flow at the non-dimensional time of $\tau \approx 150$, causing the rapid development of an oscillatory cross-stream force. As the amplitude of C_Z grows, the amplitudes of the fluctuating lift and drag rapidly decrease. The frequencies of C_L and C_D also alter until they are twice that of C_Z when the antisymmetric mode is fully developed.

The structure of the two unsteady modes are shown in figure 6.18. The image of the unstable wake mode given in figure 6.18(a) corresponds to $\tau = 125$, and the stable antisymmetric mode of figure 6.18(b) is shown at the end of the force-time history in figure 6.17 ($\tau = 235$). Figure 6.18(a) shows a distinctive symmetric kinking in the wake while figure 6.18(b) displays the antisymmetric mode observed in experiments. Compared to the sinuous wake at $Re = 200$ (figure 6.13(b)), the antisymmetric wake at $Re = 300$ has developed a significant motion in the direction normal to the wall. The view of the wake from the side shows that alternating sides of the wake have lifted away from the wall, as is observed in experiments.

It is interesting to note that kinking of the wake similar to that in figure 6.18(a) has been repeatedly observed in the asymmetric wake behind a sphere in unbounded flow (Sakamoto & Haniu 1995; Ormières & Provansal 1999; Schouveiler & Provansal 2002) and has been described as the initial stages of the unsteady wake prior to the shedding

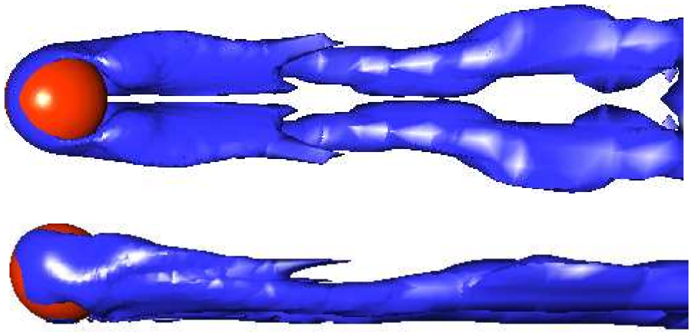

(a) Unstable symmetric wake mode at $\tau = 125$.

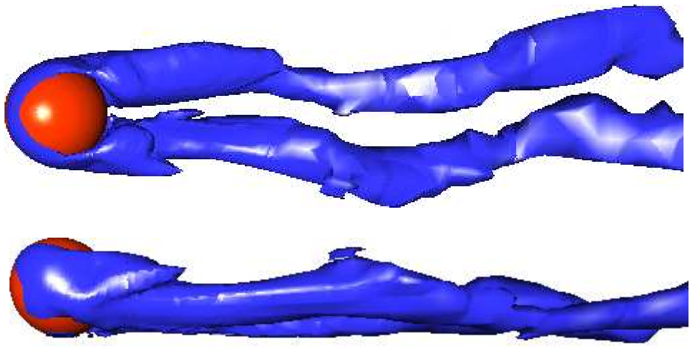

(b) Stable antisymmetric wake mode at $\tau = 235$.

FIGURE 6.18: Wake modes for $\alpha = -1$, $Re = 300$, showing the two possible unsteady modes that exist. The plotted iso-surface is as per figure 6.3.

of hairpin vortices. In this way, it is possible that the two wake modes in figure 6.18 may switch dominance, depending on the rotation rate of the sphere, leading to the shedding of hairpin vortices.

6.3.3 The transition between modes

One advantage of the use of numerical simulations is to clearly identify the effect on the wake of varying α at intermediate rotation rates. The parameter space explored experimentally indicates a general transition between the shedding of hairpin vortices and the antisymmetric wake mode, as given by the dashed vertical line located between $\alpha = 0$ and $\alpha = 0.5$ in figure 6.1. The method of dye visualisation used in experiments makes is difficult to accurately monitor the variations in the wake at intermediate rotation rates. Consequently, the range of α between 0 and 0.5 is now examined in more detail with the use of numerical simulations.

The wake structures of figure 6.19 show the effect of varying the rotation rate from $\alpha = 0.1$ to 0.5 at $Re = 200$. At $\alpha = 0.1$ (figure 6.19(a)), the wake is steady, with the

(a) $\alpha = 0.1$.

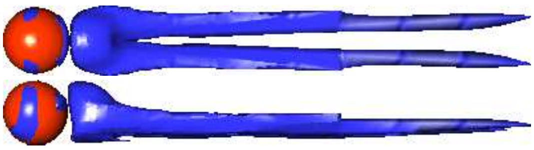

(b) $\alpha = 0.2$.

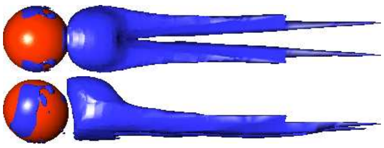

(c) $\alpha = 0.3$.

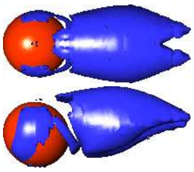

(d) $\alpha = 0.4$.

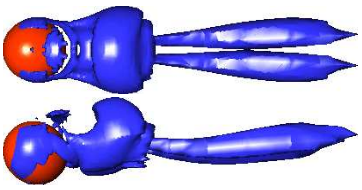

(e) $\alpha = 0.5$.

FIGURE 6.19: Series of wake images at $Re = 200$ for intermediate rotation rates.The plotted iso-surface is as per figure 6.3.

double tail forming in the recirculation zone at the rear of the sphere. As the rotation rate increases to $\alpha = 0.3$ (figure 6.19(c)) the strength of the twin vortex tails steadily decreases and the recirculation zone immediately behind the sphere (identified by the compact structure in the near wake) grows in size. In the side views of figure 6.19(a) to (c), the increased rotation has caused the region of vorticity behind the sphere to extend away from the wall and towards the top of the sphere.

When $\alpha = 0.4$ (figure 6.19(d)), the streamwise dimension of the wake has reduced to such an extent that the double tail has almost disappeared. In addition, the vortex structure is now positioned near the top of the sphere and is almost completely removed from the region near the wall. At this rotation rate and Reynolds number, the body rotation is on the verge of destabilising the wake. A further increase in α to 0.5 produces the unsteady wake shown in figure 6.19(e). This unsteady wake involves the shedding of low strength hairpin vortices that remain close to the wall as they move downstream. This wake is of a similar form to the onset of unsteady flow shown experimentally in figure 6.8.

To summarise the results shown in figure 6.19, increasing the magnitude of rotation from 0.1 to 0.5 has three main effects. These are: (1) to decrease the length of the streamwise vortices, (2) to increase the size of the dense region of vorticity immediately behind the sphere and (3) to increase the amount of vorticity rolling up at the sides of the sphere. These variations bring about a gradual change from the streamwise vortex pair, which has previously been shown to be susceptible to perturbations in the flow that result in the antisymmetric mode, to the compact recirculation zone positioned near the top of the sphere, which becomes unstable and results in the shedding of hairpin vortices.

6.3.4 The wake frequency

From movies taken of the unsteady wake modes, it is possible to calculate the frequency of the symmetric and antisymmetric wake modes as follows. Depending on the view of the wake that is recorded, a single line of pixels may be considered in each frame of the movie, which just captures the instability in the wake. This was found to be most easily obtained using a view of the wake from the side, such as that given in figure 6.20(a). After identification of the most suitable pixel line, a computer script was used to extract a single line of pixels from each successive frame in the movie. An example pixel line is shown in red in figure 6.20(a) and its placement just captures the peaks of the three-dimensional wake structures that have lifted away from the wall. The single line of pixels extracted from each frame in the sequence are then put together to create a space-time diagram of the instability mode. The space-time diagram for $Re = 250$ and $\alpha = -1$ is given in figure 6.20(b).

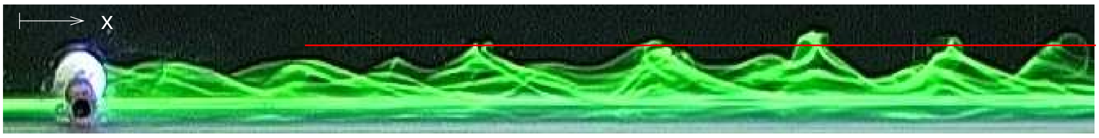

(a) Individual frame from the unsteady wake sequence. The red line indicates the pixels that were used to construct the space-time diagram below.

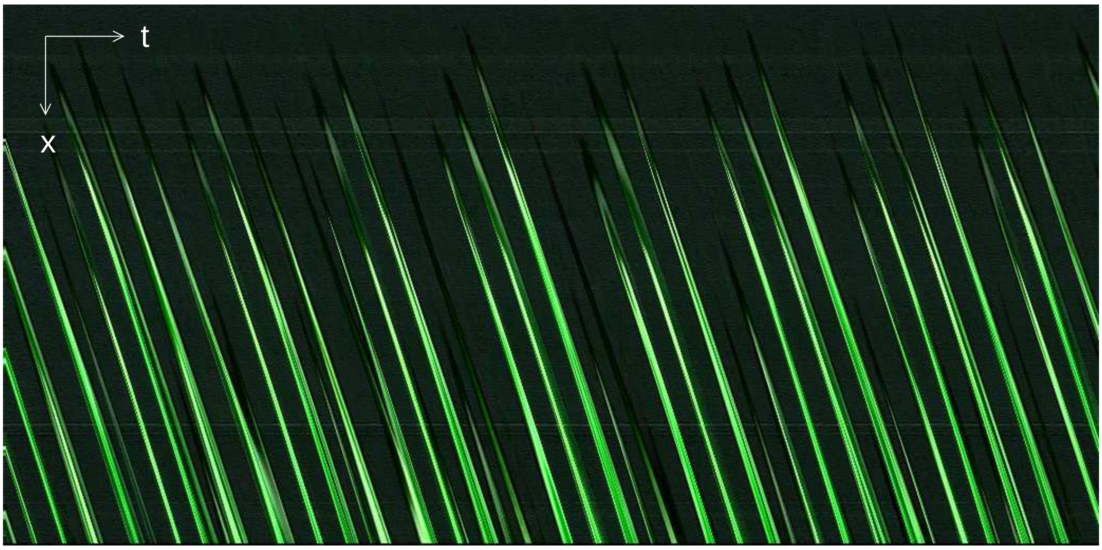

(b) Space-time diagram providing the frequency of the unsteady wake mode.

FIGURE 6.20: Method used to calculate the wake frequency at $Re = 250$, $\alpha = -1$.

From the space-time diagram of figure 6.20(b), and knowing the number of frames per second, the frequency of the instability can then be extracted. This may either be done directly, by inspection of the space-time diagram and pixel coordinates, or with the use of a Fast Fourier Transform along the t-axis. Both methods were used in the present study. Note that the frequency obtained from figure 6.20 will actually be twice that of the unsteady wake mode. This is due to the fact that the selected pixel line captures peaks from structures developing on alternating sides of the wake. Other views are possible, depending on the angle from which the movie is recorded, however, some care needs to be taken as to the most appropriate row of pixels that will clearly capture the unsteady mode. The space-time diagram for $\alpha > 0$ may be constructed in a way similar to that of figure 6.20, with a line of pixels specified to capture the top of the hairpin vortices when viewed from the side.

The wake frequencies obtained by the methods outlined above have been used to calculate St, and these values are plotted as a function of the Reynolds number for each α in figure 6.21. For positive α (figure 6.21(b)), the Strouhal number shows greater variation and the increasing linear trend for $\alpha = 1$ is shown by the solid line in figure 6.21(b).

A possible synchronization of the shedding frequency and the sphere rotation was observed for $\alpha = 0.5$. In this case, the values of the shedding frequency are close to the frequency of the sphere rotation. In such cases, it is known that small perturbations in the body motion can cause a synchronization of the wake to the body frequency (Williamson 2004). In figure 6.21(b), the value of St associated with the sphere motion is given by the dashed horizontal line. As Re increases, the frequency of vortex shedding experiences a sudden jump at $Re > 160$ to values much nearer this line, indicating that synchronization may have occurred. Such a discontinuity is not observed for any of the other rotation rates and the values of St in other cases differ significantly from the frequency of the sphere motion.

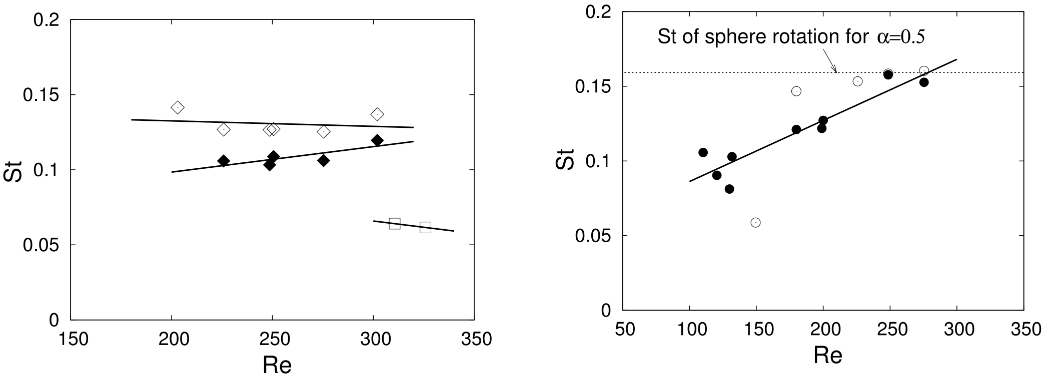

(a) St for $\alpha = 0$ (□), $\alpha = -0.5$ (◆) and $\alpha = -1$ (◇).

(b) St for $\alpha = 1$ (●) and $\alpha = 0.5$ (○).

FIGURE 6.21: Strouhal number variation of the experimental results with Re, for all five rotation rates. Solid lines indicate the linear trends for each α.

Although the investigation by Zeng *et al.* (2005) is focused on the non-rotating sphere, they find that the unsteady wake involves the shedding of hairpin vortices in the symmetric mode when a gap ratio of $0.5D$ is imposed. During this shedding process, they calculate a Strouhal number of approximately 0.15 at $Re = 270$. This is in reasonable agreement with the St values plotted in figure 6.21(b), but varies greatly to those for $\alpha = 0$ in 6.21(a), for which a different mode is observed. For $\alpha = 0, -0.5$ and -1, given in figure 6.21(a), the antisymmetric flow shows little variation in frequency with Re. Instead, St appears to depend only on the rotation rate of the sphere, and St decreases slightly as α is reduced.

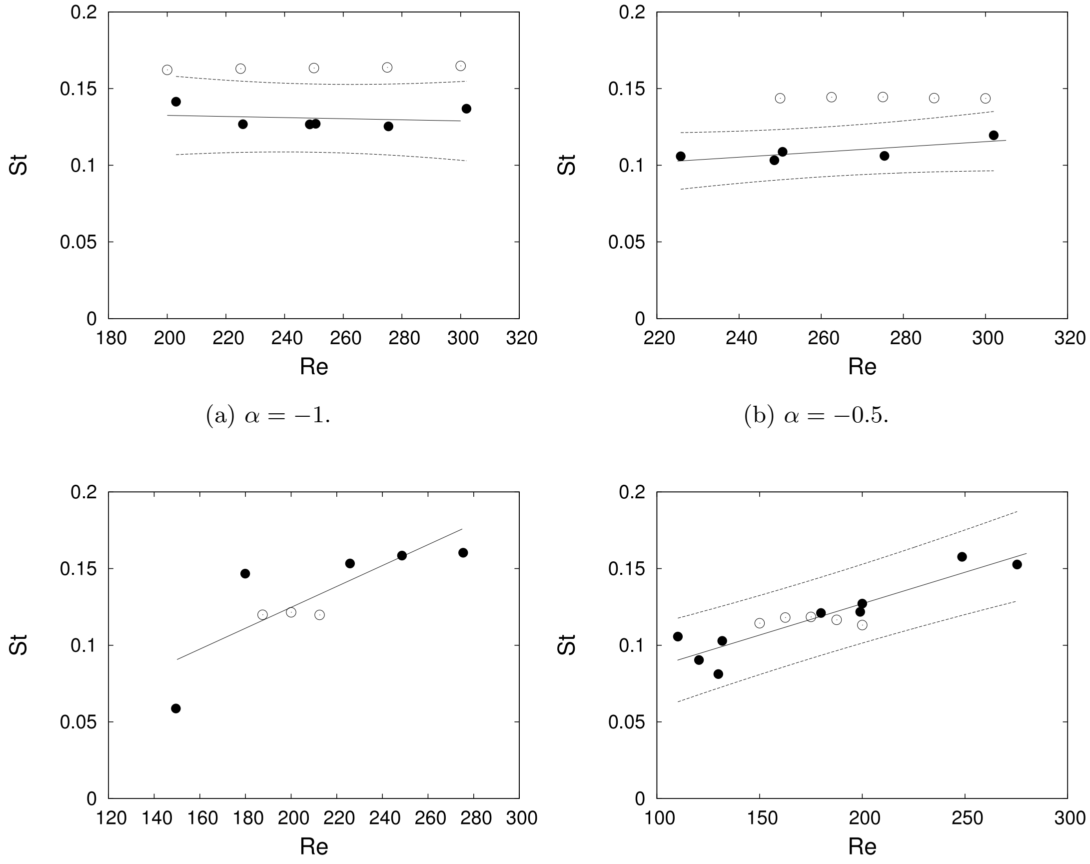

(a) $\alpha = -1$.

(b) $\alpha = -0.5$.

(c) $\alpha = 0.5$.

(d) $\alpha = 1$.

FIGURE 6.22: Comparisons of the experimental (●) and numerical (○) wake frequencies for the four non-zero rotation rates. The solid lines indicate the linear trend of the experimental data and the dashed lines represent the 95% prediction inverval calculated from the experimental results.

From the experimental Strouhal number data given above, the 95% prediction interval has been calculated for the cases of $\alpha = 1$, -0.5 and -1. Due to the large variation in the data, the prediction interval for $\alpha = 0.5$ is considered to be invalid and has been omitted. The prediction interval was considered a more appropriate measure of the error than the confidence interval, due to the small number of data points. This information is shown in figure 6.22, along with values of St obtained from the numerical simulations. Due to the lack of data available at $\alpha = 0$, these results have not been shown in figure 6.22. The prediction intervals and linear trends shown in figure 6.22 are calculated solely from the experimental data. As may be expected, the sudden jump in the values of St for $\alpha = 0.5$ is reflected in the much larger prediction interval of figure 6.22(c). The numerical values, obtained from the frequency of the transverse forcing on the sphere, are also shown for comparison and are plotted as empty circles.

For numerical simulations with $\alpha < 0$ (figures 6.22(a) and 6.22(b)), the general trend is maintained in which decreasing the magnitude of rotation decreases the wake frequency. However, the numerical data consistently overestimate those obtained from experiments. It is possible that this is due to differences in the gap ratio between the simulations and experiments, with a larger displacement being present in the latter case. The gap resolution study of section 2.1.5 indicates a decrease in St when small increases in the gap ratio are considered. Both the numerical and experimental values of St in figures 6.22(a) and 6.22(b) appear to be fairly independent of changes in Re. However, the critical Reynolds number of transition to unsteady flow differs, and at $Re = 225$ the numerical simulations provided a steady flow solution for $\alpha = -0.5$, even following the addition of noise to the solution, and transition to unsteady flow takes place at higher Re than in the experiments.

For $\alpha > 0$, the magnitude of St from the numerical simulations shows a reasonable agreement with the experiments and the numerical data fall within the experimental prediction intervals. However, the simulations indicate that the onset of unsteady flow again occurs at higher Re than in experiments. For $\alpha = 1$, this occurs at $125 < Re < 150$ and for $\alpha = 0.5$, the transition takes place when $175 < Re < 187.5$. Unlike the experimental data, which show an increasing trend with Re, the numerical simulations provide St values that are more constant and lie in the region of $St \approx 0.12$, independent of the rotation rate. This is somewhat lower than the values of 0.136 and 0.137 obtained by Tomboulides & Orszag (2000) and Johnson & Patel (1999) for the wake of a sphere in unbounded flow at $Re = 300$. Zeng *et al.* (2005) found that the Strouhal number increases as the sphere approaches the wall, however, no gap ratios below 25% of the diameter were considered in their study and no conclusions were reached as to how St may vary in the region very close to the wall.

In figure 6.22(d) with $\alpha = 1$, the wake remains clearly periodic, with a single distinct wake frequency in the transverse force over the range of Re considered. This is not true for all Re considered when $\alpha = 0.5$. The numerical data plotted in figure 6.22(c) show a single dominant wake frequency, but as Re increases beyond 210, a second low frequency component develops. This is illustrated with the two frequency spectra given in figure 6.23. At $\alpha = 0.5$ and $Re = 212.5$ (figure 6.23(a)), the wake is ordered and periodic, with a Strouhal number of 0.120. Increasing the Reynolds number causes a low frequency mode to grow in the wake, with $St \approx 0.045$. By $Re = 225$ (figure 6.23(b)), this has become the dominant wake frequency.

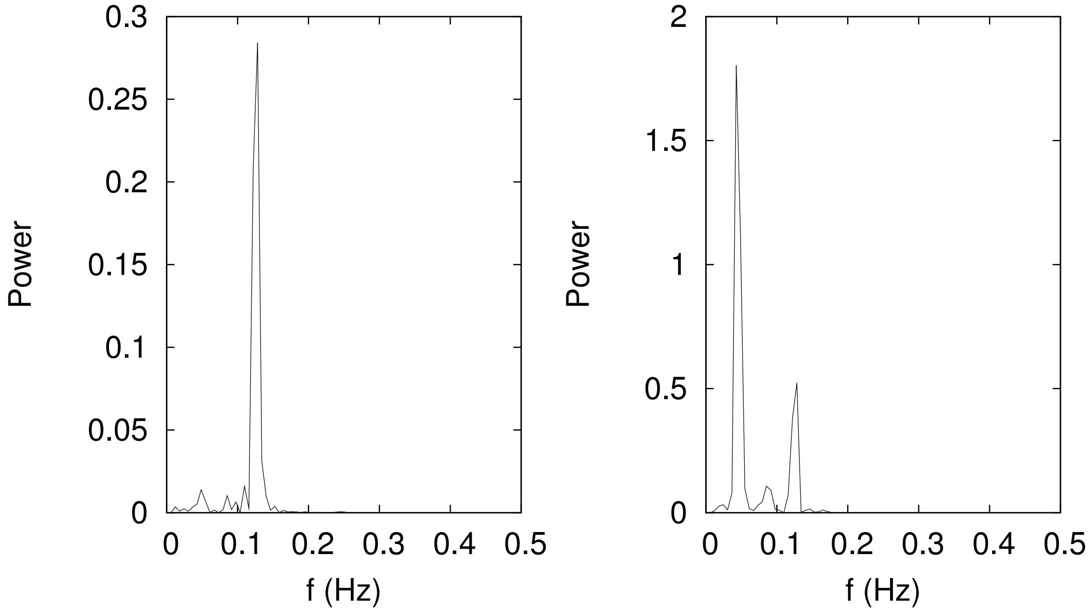

(a) Single dominant frequency at $Re = 212.5$.

(b) Dual spectral peaks at $Re = 225$.

FIGURE 6.23: Frequency power spectra for $\alpha = 0.5$ showing the development of a low frequency component as Reynolds number increases.

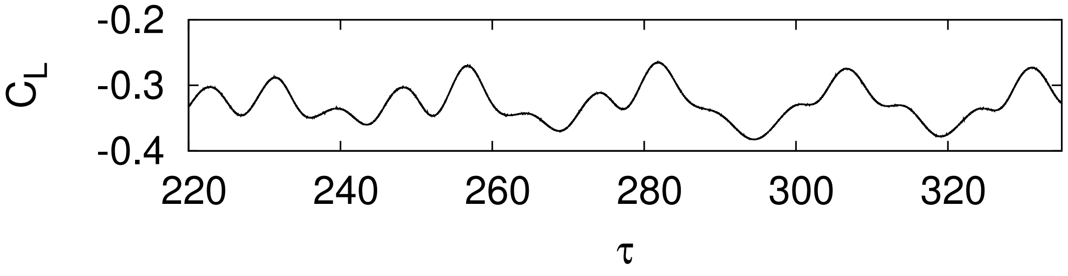

FIGURE 6.24: Lift-time history for the sphere at $\alpha = 0.5$ and $Re = 225$, showing the effect of multiple frequencies on the wake.

The two frequency components of figure 6.23(b) result in a low frequency modulation in the wake that affects the strength of the hairpin vortices that are shed from the

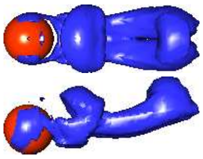

(a) $\tau = 300$.

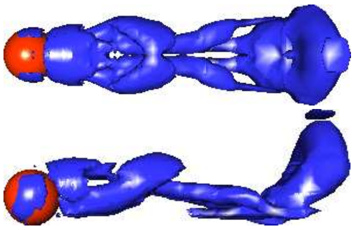

(b) $\tau = 305$.

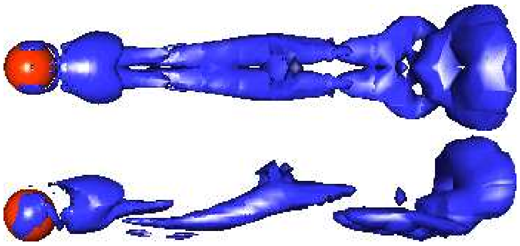

(c) $\tau = 310$.

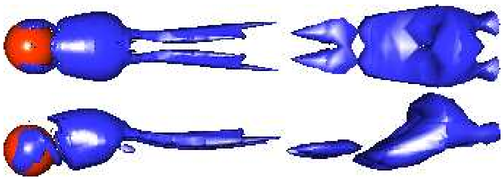

(d) $\tau = 315$.

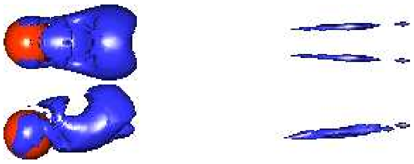

(e) $\tau = 320$.

FIGURE 6.25: Irregular shedding for $\alpha = 0.5$ and $Re = 225$. Images are taken at the non-dimensional times indicated. These correspond to the lift-time history shown in figure 6.24. The plotted iso-surface is as per figure 6.3.

sphere. This is shown by the time history of the wake-induced lift force on the sphere. Figure 6.24 shows the variation in lift force for $\alpha = 0.5$ and $Re = 225$ over several periods of the low frequency mode. The variation in the value of the local maximum lift indicates the shedding of hairpin vortices of varying strength.

In order to understand better the effect that this frequency modulation has on the structures in the wake, a series of images have been taken, corresponding to the non-dimensional times shown in figure 6.24 of $\tau = 300$, 305, 310, 315 and 320. These wake images are given in figure 6.25 and show the development of the wake over slightly less than one period of the low frequency mode. In figure 6.25(b), two closely spaced hairpin vortices are present in the wake. As they progress downstream, it becomes apparent that these vortices are not of equal strength, and the near-wake vortex is the weaker of the two. As the downstream-most vortex progresses, it forms a vortex ring oriented almost perpendicular to the wall. This is shown at the downstream-most point of the wake at $\tau = 310$. However, the near-wake vortex of figure 6.25(a) remains more parallel to the wall as it progresses downstream and at $\tau = 315$, this hairpin vortex has developed into a weak vortex ring, located at the right-hand side of the image. At $\tau = 320$, both of these vortices have moved out of frame, and only a single, newly formed hairpin vortex is present in the near wake. This mode of vortex shedding does not comprise a regular periodic wake.

6.4 Chapter summary

Good qualitative agreement has been found between the experimental and numerical wake formations behind the rolling sphere. The experimental investigation found four distinct wake modes to occur: two steady and two unsteady. These wake modes are strongly dependent on the rotation rate of the sphere. Furthermore, the steady modes observed maintain a planar symmetry that is fixed perpendicular to the wall and passes through the sphere centre.

Forward rolling of the sphere creates a compact zone of recirculating fluid that undergoes a transition to the shedding of hairpin vortices as the Reynolds number increases. When reversed rolling is imposed, the wake takes the form of a streamwise vortex pair that originates at the sides of the sphere for $\alpha < 0$, and at the rear of the body for $\alpha = 0$. These streamwise vortices undergo a transition to an antisymmetric wake mode as Re Increases.

The unsteady, antisymmetric wake mode occurring behind the sphere for $\alpha < 0$ is a new mode that has not previously been reported in the wake of a sphere. From observations and images of the flow it is concluded that the wake is composed of two spiral vortices that wind in opposite directions and are half a wavelength out of phase. This motion results in a sinuous motion of the vortex cores when viewed from above. The axes of these spirals are not quite parallel in the streamwise direction, as there is a slight divergence of the wake downstream.

Numerical simulations were used to provide additional information about the structure of these steady and unsteady wake modes. Visualisations of the vorticity for $\alpha > 0$ show that the wake has a structure that closely resembles the double tail, although on a reduced scale and displaced further from the wall. A numerical examination of intermediate rotation rates between 0.1 and 0.5 have indicated that the two steady modes observed experimentally undergo a smooth and continuous transition from one to the other and that the two elongated streamwise vortices are present in the wake for low magnitude positive α. In this respect, the 'two' steady modes may be better described as a single mode, the structure of which is strongly affected by the body rotation.

In addition to the wake modes described above, the numerical simulations have shown an unstable bifurcation in the solutions for the unsteady wake at $\alpha < 0$. When the flow develops with no background turbulence or external perturbation, a symmetric mode is possible. This unstable symmetric mode displays a kinking of the streamwise vortices in the wake. The introduction of a small perturbation to this flow brings about a transition to the antisymmetric wake mode observed in experiments. The symmetric kinking observed in the wake for $\alpha < 0$ may be an unstable extension of the solution branch that results in the shedding of hairpin vortices for $\alpha > 0$.

The numerical simulations provide values for the Strouhal number that are in reasonable agreement with the experiments when $\alpha > 0$. However, the numerical results consistently overestimate the experimental values when $\alpha < 0$. This may be the result of slight differences in the gap ratio between the two cases. The numerical simulations also indicate a higher value of Re for the transition to unsteady flow.

Chapter 7

Conclusions

A study of the flow around rolling and sliding cylinders and spheres has been conducted using a variety of numerical and experimental techniques. The main findings from this study are outlined below, along with some suggested topics of future work.

Two-dimensional simulations of the flow around the cylinder have revealed that when the cylinder has a positive rotation, two jets of fluid form at the nearest point between the cylinder and the wall. An inflow jet forms on the upstream side of the gap and an outflow jet is created on the downstream side. This flow creates a recirculation zone that encircles the cylinder surface. When the cylinder is undergoing reversed rotation, it is possible for the upstream flow to attach to the cylinder surface and to remain fully attached as it is entrained by the cylinder surface and carried away by the wall on the downstream side of the body.

As the Reynolds number of the flow increases, the steady flow behind the cylinder develops two recirculation zones, the locations of which are supported by experimental observation. The recirculation zone nearest the wall is not present when the cylinder and wall are fixed in space; and the existence of this region is due to the relative motion of the plane wall. The lengths of both of these recirculation zones increase linearly with Re until the predicted onset of unsteady flow.

At the lower Reynolds number limit of this study, the two-dimensional simulations show that the forces on the cylinder are dominated by the drag. Increasing Re reduces this effect, and for negative rotation rates the motion of the cylinder acts to accelerate the fluid over the top of the body and the lift force comes to dominate.

From the two-dimensional simulations, unsteady flow is first predicted to occur at Re above 90. This is approximately twice the critical Reynolds number reported for the transition to unsteady flow around a cylinder placed far from a solid boundary.

These results have shown that the presence of the wall acts to stabilise the flow, while increasing the rotation rate from -1 to 1 destabilises it. Negative rotation rates provide the most stable solutions and are capable of preventing flow separation and transition.

Vortex shedding takes place through the roll-up of the shear layer that forms over the top of the cylinder. This in turn destabilises the wall shear layer, which rolls up into a vortex of opposite sign. These vortices create a pair that lift away from the wall as they travel downstream. In the range of Reynolds number considered, the frequency of this vortex shedding is largely insensitive to changes in Re (except for the case of $\alpha = -1$). This is in agreement with findings for the unsteady wake of a cylinder held fixed near a stationary wall (Huang & Sung 2007; Lei *et al.* 1999, 2000; Arnal *et al.* 1991). The structure of the unsteady mode is supported by experimental observations, particularly regarding the position of the shed vortices and the lift-off of these vortex pairs from the wall.

Following a linear stability analysis of the steady two-dimensional base flow, the wake of the rolling cylinder is predicted to become three-dimensional well before the onset of unsteady flow. For all values of α studied, the three-dimensional mode takes the form of flattened streamwise vortices, similar to those detected behind the backward-facing step (Barkley *et al.* 2002). The spanwise wavelength of this mode is highly dependent on the rotation rate, as is the critical Reynolds number at which this flow develops. The onset of unsteady flow is delayed as the rotation rate varies from 1 to -1, again confirming that negative α provides the most stable solution. Three-dimensional simulations of the cylinder wake show a very good agreement with the structure of the three-dimensional flow, as predicted from the stability analysis.

It is speculated that the transition to three-dimensional flow may be due to the growth of a centrifugal instability in the wake. In order to test this theory, a centrifugal stability analysis was carried out according to the method described by Bayly (1988) on the closed streamlines of the two recirculation zones. The outwardly increasing circulation indicates that a centrifugal instability does not develop in these regions. It is still possible that a region of local centrifugal instability exists near the cylinder surface, or the downstream wall, which are shown to be regions of high perturbation vorticity. However, the findings on this matter are still inconclusive.

When considering the flow around the rolling and sliding sphere, the parameter space was investigated experimentally using the closed circuit water tunnel with a moving floor and boundary layer suction. In this way, four separate wake modes were identified: two steady modes and two unsteady modes that are dependent on the rotation rate of the body. Numerical simulations later showed that the ‘two’ steady wake modes are actually a single mode, and that the different structures observed experimentally are the result of a continuous evolution brought about by changes in the sphere rotation.

When the sphere is undergoing forward rolling, the steady wake is characterised by a compact recirculation zone behind the body that is displaced slightly away from the wall. Although not apparent in the experiments, the numerical simulations reveal the presence of two short tails of vorticity that extend into the wake. Decreasing the rotation rate causes these two tails to extend further downstream and to move closer to the wall. When the rotation rate becomes negative, the compact recirculation zone behind the sphere disappears and the vorticity rolls up around the sides of the body. This forms two counter-rotating vortices that persist for some distance downstream. All of these steady modes have a plane of symmetry that is fixed normal to the wall.

As the Reynolds number of the flow is increases, two distinct unsteady modes develop. The first of these is apparent for $\alpha > 0$ and resembles the wake behind a sphere in unbounded flow. This wake is symmetric and involves the shedding of hairpin vortices that form over the top of the sphere. This unsteady mode has also been detected behind the non-rotating sphere moving in the vicinity of a wall (Zeng *et al.* 2005).

For $\alpha < 0$, a different mode is observed in the sphere wake, in which the two streamwise vortices become unstable and begin to oscillate in a plane parallel to the wall. As the Reynolds number of the flow increases, the two vortices begin to lift away from the wall on alternating sides of the wake. This out-of-plane movement of the wake was observed in both experiments and numerical simulations and represents a spiral motion of the vortices. The two vortex spirals wind in opposite directions and are half a wavelength out of phase.

Experiments show the structure of this mode to be antisymmetric and the numerical simulations show the growth of the force in the transverse direction. Computationally, this mode only grows after the introduction of random noise to the system. A small perturbation is enough to trigger the transverse motion in the wake on a base flow that is otherwise steady and symmetric. In the case of the non-rotating sphere, the early signs of this antisymmetric mode are observed at the upper limits of the Re range achievable in the experiments. However, the numerical simulations at $Re = 300$ are stable and steady and do not develop this antisymmetry, even when perturbed.

The antisymmetric mode detected in experiments and computations has similarities to the short wavelength instability that develops in a pair of long streamwise vortices (Leweke & Williamson 1998a). This mode grows, following an interaction of the vortex cores in the region immediately behind the sphere. The reason for this transition is thought to be due to an elliptic instability that develops in the vortex cores.

For $\alpha = -1$ at higher Reynolds number, the numerical code has revealed the existence of a real unstable solution to the flow. The unsteady wake takes the form of symmetric kinking between the two streamwise vortices. This mode is unstable and, following a small perturbation to the flow, undergoes the transition to the antisymmetric mode observed in experiments. This transition, and the growth of the transverse force in the antisymmetric mode, indicate clearly the existence of at least two distinct unsteady regimes. The exact relationship between the unstable symmetric mode detected for $\alpha = -1$ and the stable shedding of hairpin vortices at $\alpha > 0$ is the subject of ongoing research.

In contrast to the flow around the cylinder, the most stable configuration for the sphere occurs at $\alpha = 0$. This indicates that, while the wall acts to stabilise the wake, rotation of the sphere in any direction acts to destabilise it.

7.1 Further work

From this thesis, several findings have been reported that present potential areas of further study. These include:

1. A more detailed study of the unsteady three-dimensional wake behind the rolling and sliding cylinder. From the present work, it is unclear how the initial transition to three-dimensional flow, which has been identified during the steady flow regime, will affect the transition to unsteady flow. Full three-dimensional simulations, or experiments with a much larger aspect ratio than those of the present experimental study, could also be used to identify the form of the dominant three-dimensional structures.

2. It is suggested in the present work that the mechanism responsible for the transition to three-dimensional flow in the wake of the cylinder is centrifugal in nature.

Attempts to identify this in the recirculation zones failed. Consequently, a detailed analysis of other regions of the flow, particularly near the cylinder and wall boundaries, could prove enlightening.

3. In the unsteady, antisymmetric wake behind the sphere, there exist similarities with the short wavelength instability. A further analysis of the near wake structure and positive identification of an elliptic instability as the cause of this mode would be useful.

4. An unstable bifurcation branch has been detected numerically in the wake of the sphere for $\alpha < 0$. A further analysis of intermediate rotation rates could be used to determine if there exists a connection between this unstable symmetric wake mode and the stable symmetric shedding of hairpin vortices observed for $\alpha > 0$.

The suggested topics of study listed above offer some shorter, detailed investigations into the flow. However, there is also the opportunity for several larger studies that relate to the flows or the geometry considered in this thesis. One of these is the extension of this work to much lower Reynolds number. The movement of a sphere, especially at $Re << 1$, has applications in biological flows with the movement of blood cells. This is an area of rapidly growing research and one that can benefit from a better understanding of the particle motions and forces involved.

Bibliography

Achenbach, E. 1975 Vortex shedding from spheres. *Journal of Fluid Mechanics* **62**, 209–221.

Ambari, A., Gauthier-Manuel, B. & Guyon, E. 1984 Wall effects on a sphere translating at constant velocity. *Journal of Fluid Mechanics* **149**, 235–253.

Armaly, B. F., Durst, F., Pereira, J. C. F. & Schönung, B. 1983 Experimental and theoretical investigation of backward-facing step flow. *Journal of Fluid Mechanics* **127**, 473–496.

Arnal, M. P., Goering, D. J. & Humphrey, J. A. C. 1991 Vortex shedding from a bluff body adjacent to a plane sliding wall. *Transactions of the ASME: Journal of Fluids Engineering* **113**, 384–398.

Ashmore, J., del Pino, C. & Mullin, T. 2005 Cavitation in a lubrication flow between a moving sphere and a boundary. *Physical Review Letters* **94**, 124501–1–4.

Badr, H. M. & Dennis, S. C. R. 1985 Time-dependent viscous flow past an impulsively started rotating and translating circular cylinder. *Journal of Fluid Mechanics* **158**, 447–488.

Badr, H. M., Dennis, S. C. R. & Young, P. J. S. 1989 Steady and unsteady flow past a rotating circular cylinder at low Reynolds numbers. *Computers and Fluids* **17** (4), 579–609.

Barkley, D., Gomes, M. G. M. & Henderson, R. D. 2002 Three-dimensional instability in flow over a backward-facing step. *Journal of Fluid Mechanics* **473**, 167–190.

Barkley, D. & Henderson, R. D. 1996 Three-dimensional Floquet stability analysis of the wake of a circular cylinder. *Journal of Fluid Mechanics* **322**, 215–241.

Barkley, D., Tuckerman, L. S. & Golubitsky, M. 2000 Bifurcation theory for three-dimensional flow in the wake of a circular cylinder. *Physical Review E* **61** (5), 5247–5252.

Barnes, F. H. 2000 Vortex shedding in the wake of a rotating circular cylinder at low Reynolds numbers. *Journal of Physics, D* **33**, L141–L144.

Bayly, B. J. 1988 Three-dimensional centrifugal-type instabilities in inviscid two-dimensional flows. *Physics of Fluids* **31** (1), 56–64.

Bearman, P. W. & Zdravkovich, M. M. 1978 Flow around a circular cylinder near a plane boundary. *Journal of Fluid Mechanics* **89**, 33–47.

Beaudoin, J.-F., Cadot, O., Aider, J.-L. & Wesfreid, J. E. 2004 Three-dimensional stationary flow over a backward-facing step. *European Journal of Mechanics, B/Fluids* **23**, 147–155.

Becker, L. E., McKinley, G. H. & Stone, H. A. 1996 Sedimentation of a sphere near a plane wall: weak non-Newtonian and inertial effects. *Journal of Non-Newtonian Fluid Mechanics* **63**, 201–233.

Bhattacharyya, S., Mahapatra, S. & Smith, F. T. 2004 Fluid flow due to a cylinder rolling along ground. *Journal of Fluids and Structures* **19**, 511–523.

Blackburn, H. M. & Lopez, J. M. 2003 On three-dimensional quasiperiodic Floquet instabilities of two-dimensional bluff body wakes. *Physics of Fluids* **15** (8), L57–L60.

Chen, Y.-M., Ou, Y.-R. & Pearlstein, A. J. 1993 Development of the wake behind a circular cylinder impulsively started into a rotatory and rectilinear motion. *Journal of Fluid Mechanics* **253**, 449–484.

Cheng, M. & Luo, L.-S. 2007 Characteristics of two-dimensional flow around a rotating circular cylinder near a plane wall. *Physics of Fluids* **19**, 063601–1–063601–17.

Cherukat, P. & McLaughlin, J. B. 1990 Wall-induced lift on a sphere. *International Journal of Multiphase Flow* **16** (5), 899–907.

Cherukat, P. & McLaughlin, J. B. 1994 The inertial lift on a rigid sphere in a linear shear flow field near a flat wall. *Journal of Fluid Mechanics* **263**, 1–18.

Chew, Y. T., Cheng, M. & Luo, S. C. 1995 A numerical study of flow past a rotating circular cylinder using a hybrid vortex scheme. *Journal of Fluid Mechanics* **299**, 35–71.

Collins, W. M. & Dennis, S. C. R. 1973 Flow past an impulsively started circular cylinder. *Journal of Fluid Mechanics* **60**, 105–127.

Coutanceau, M. & Ménard, C. 1985 Influence of rotation on the near-wake development behind an impulsively started circular cylinder. *Journal of Fluid Mechanics* **158**, 399–446.

Cox, R. G. & Hsu, S. K. 1977 The lateral migration of solid particles in a laminar flow near a plane. *International Journal of Multiphase Flow* **3**, 201–222.

Crouch, J. D. 1997 Instability and transient growth for two trailing-vortex pairs. *Journal of Fluid Mechanics* **350**, 311–330.

Dennis, S. C. R. & Chang, G.-Z. 1970 Numerical solutions for steady flow past a circular cylinder at Reynolds numbers up to 100. *Journal of Fluid Mechanics* **42**, 471–489.

Dennis, S. C. R. & Walker, J. D. A. 1971 Calculation of the steady flow past a sphere at low and moderate Reynolds numbers. *Journal of Fluid Mechanics* **48**, 771–789.

Díaz, F., Gavaldà, J., Kawakk, J. G., Keffer, J. F. & Giralt, F. 1983 Vortex shedding from a spinning cylinder. *Physics of Fluids* **26** (12), 3454–3460.

Dipankar, A. & Sengupta, T. K. 2005 Flow past a circular cylinder in the vicinity of a plane wall. *Journal of Fluids and Structures* **20** (3), 403–423.

Drazin, P. G. & Reid, W. H. 1981 *Hydrodynamic Stability*. New York: Cambridge University Press.

Ersoy, S. & Walker, J. D. A. 1985 Viscous flow induced by counter-rotating vortices. *Physics of Fluids* **28** (9), 2687–2698.

Fabre, D., Jacquin, L. & Loof, A. 2002 Optimal perturbations in a four-vortex aircraft wake in counter-rotating configuration. *Journal of Fluid Mechanics* **451**, 319–328.

Ferziger, J. H. & Perić, M. 2002 *Computational Methods for Fluid Dynamics*, 3rd edn. New York: Springer.

Ghia, K. N., Osswald, G. A. & Ghia, U. 1989 Analysis of incompressible massively separated viscous flows using unsteady Navier-Stokes equations. *International Journal for Numerical Methods in Fluids* **9**, 1025–1050.

Ghidersa, B. & Dušek, J. 2000 Breaking of axisymmetry and onset of unsteadiness in the wake of a sphere. *Journal of Fluid Mechanics* **423**, 33–69.

Goldman, A. J., Cox, R. G. & Brenner, H. 1967a Slow viscous motion of a sphere parallel to a plane wall- I. Motion through a quiescent fluid. *Chemical Engineering Science* **22**, 637–651.

Goldman, A. J., Cox, R. G. & Brenner, H. 1967b Slow viscous motion of a sphere parallel to a plane wall- II. Couette flow. *Chemical Engineering Science* **22**, 653–660.

Griffith, M. D., Thompson, M. C., Leweke, T., Hourigan, K. & Anderson, W. P. 2007 Wake behaviour and instability of flow through a partially blocked channel. *Journal of Fluid Mechanics* **582**, 319–340.

Hammache, M. & Gharib, M. 1991 An experimental study of the parallel and oblique vortex shedding from circular cylinders. *Journal of Fluid Mechanics* **232**, 567–590.

Henderson, R. D. 1997 Nonlinear dynamics and pattern formation in turbulent wake transition. *Journal of Fluid Mechanics* **352**, 65–112.

Hu, H. H. & Joseph, D. D. 1999 Lift on a sphere near a plane wall in a second-order fluid. *Journal of Non-Newtonian Fluid Mechanics* **88**, 173–184.

Huang, W.-X. & Sung, H. J. 2007 Vortex shedding from a circular cylinder near a moving wall. *Journal of Fluids and Structures* **23**, 1064–1076.

Humphrey, J. A. C. & Murata, H. 1992 On the motion of solid spheres falling through viscous fluids in vertical and inclined tubes. *Transactions of the ASME: Journal of Fluids Engineering* **114**, 2–11.

Ingham, D. B. 1983 Steady flow past a rotating cylinder. *Computers and Fluids* **11** (4), 351–366.

Ingham, D. B. & Tang, T. 1990 A numerical investigation into the steady flow past a rotating circular cylinder at low and intermediate Reynolds numbers. *Journal of Computational Physics* **87**, 91–107.

Jackson, C. P. 1987 A finite-element study of the onset of vortex shedding in the flow past variously shaped bodies. *Journal of Fluid Mechanics* **182**, 23–45.

Jacquin, L., Fabre, D., Sipp, D., Theofilis, V. & Vollmers, H. 2003 Instability and unsteadiness of aircraft wake vortices. *Aerospace Science and Technology* **7**, 577–593.

Jaminet, J. F. & Van Atta, C. W. 1969 Experiments on vortex shedding from rotating circular cylinders. *AIAA Journal* **7**, 1817–1819.

Jeong, J. & Hussain, F. 1995 On the identification of a vortex. *Journal of Fluid Mechanics* **285**, 69–94.

Johnson, T. A. & Patel, V. C. 1999 Flow past a sphere up to a Reynolds number of 300. *Journal of Fluid Mechanics* **378**, 19–70.

Kang, S., Choi, H. & Lee, S. 1999 Laminar flow past a rotating circular cylinder. *Physics of Fluids* **11** (11), 3312–3321.

KANO, I. & YAGITA, M. 2002 Flow around a rotating circular cylinder near a moving plane wall. *Japanese Society of Mechanical Engineers International Journal, Series B* **45** (2), 259–268.

KARNIADAKIS, G. E., ISRAELI, M. & ORSZAG, S. A. 1991 High-order splitting methods for the incompressible Navier-Stokes equations. *Journal of Computational Physics* **97**, 414–443.

KAWAGUTI, M. 1955 The critical Reynolds number for the flow past a sphere. *Journal of the Physical Society of Japan* **10** (8), 694–699.

KAWAGUTI, M. 1966 Numerical study of a viscous fluid flow past a circular cylinder. *Journal of the Physical Society of Japan* **21** (10), 2055–2062.

KOVASZNAY, L. S. G. 1949 The flow past circular cylinders at low speeds. *Proceedings of the Royal Society of London A* **198** (1053), 174–190.

KUROSE, R. & KOMORI, S. 1999 Drag and lift forces on a rotating sphere in a linear shear flow. *Journal of Fluid Mechanics* **384**, 183–206.

LABRAGA, L., BOURABAA, N. & BERKAH, T. 2002 Wall shear stress from a rotating cylinder in cross flow using the electrochemical technique. *Experiments in Fluids* **33**, 488–496.

LEI, C., CHENG, L., ARMFIELD, S. W. & KAVANAGH, K. 2000 Vortex shedding suppression for flow over a circular cylinder near a plane boundary. *Ocean Engineering* **27**, 1109–1127.

LEI, C., CHENG, L. & KAVANAGH, K. 1999 Re-examination of the effect of a plane boundary on force and vortex shedding of a circular cylinder. *Journal of Wind Engineering and Industrial Aerodynamics* **80**, 263–286.

LEONTINI, J. S., THOMPSON, M. C. & HOURIGAN, K. 2007 Three-dimensional transition in the wake of a transversely oscillating cylinder. *Journal of Fluid Mechanics* **577**, 79–104.

LEWEKE, T., PROVANSAL, M., ORMI‘ERES, D. & LEBESCOND, R. 1999 Vortex dynamics in the wake of a sphere. *Physics of Fluids* **11** (9), S12.

LEWEKE, T. & WILLIAMSON, C. H. K. 1998a Cooperative elliptic instability of a vortex pair. *Journal of Fluid Mechanics* **360**, 85–119.

LEWEKE, T. & WILLIAMSON, C. H. K. 1998b Three-dimensional instabilities in wake transition. *European Journal of Mechanics, B/Fluids* **17** (4), 571–586.

Lim, T. T., Sengupta, T. K. & Chattopadhyay, M. 2004 A visual study of vortex-induced subcritical instability on a flat plate boundary layer. *Experiments in Fluids* **37**, 47–55.

Liu, Y. J., Nelson, J., Feng, J. & Joseph, D. D. 1993 Anomalous rolling of spheres down an inclined plane. *Journal of Non-Newtonian Fluid Mechanics* **50**, 305–329.

Magarvey, R. H. & Bishop, R. L. 1961a Transition ranges for three-dimensional wakes. *Canadian Journal of Physics* **39**, 1418–1422.

Magarvey, R. H. & Bishop, R. L. 1961b Wakes in liquid-liquid systems. *Physics of Fluids* **4** (7), 800–805.

Magarvey, R. H. & MacLatchy, C. S. 1965 Vortices in sphere wakes. *Canadian Journal of Physics* **43**, 1649–1656.

Malysa, K. & van der Ven, T. G. M. 1986 Rotational and translational motion of a sphere parallel to a wall. *International Journal of Multiphase Flow* **12** (3), 459–468.

Masliyah, J. H. & Epstein, N. 1970 Numerical study of steady flow past spheriods. *Journal of Fluid Mechanics* **4**, 493–512.

Mittal, R. 1999 A Fourier-Chebyshev spectral collocation method for simulating flow past spheres and spheroids. *International Journal for Numerical Methods in Fluids* **30**, 921–937.

Mittal, R. & Balachandar, S. 1995 Generation of streamwise vortical structures in bluff body wakes. *Physical Review Letters* **75** (7), 1300–1303.

Mittal, R., Wilson, J. J. & Najjar, F. M. 2002 Symmetry properties of the transitional sphere wake. *AIAA Journal* **40** (3), 579–582.

Mittal, S. 2001 Flow past rotating cylinders: The effect of eccentricity. *Transactions of the ASME: Journal of Applied Mechanics* **68**, 543–552.

Mittal, S. 2004 Three-dimensional instabilities in flow past a rotating cylinder. *Journal of Applied Mechanics* **71**, 89–95.

Mittal, S. & Kumar, B. 2003 Flow past a rotating cylinder. *Journal of Fluid Mechanics* **476**, 303–334.

Nakagawa, M., Aritomi, M., Kumano, Y. & Mori, M. 2006 Investigation of zigzag rising bubble using spinning sphere model. *JSME International Journal, Series B* **49** (4), 1016–1021.

Natarajan, R. & Acrivos, A. 1993 The instability of the steady flow past spheres and disks. *Journal of Fluid Mechanics* **254**, 323–344.

NIAZMAND, H. & RENKSIZBULUT, M. 2003 Surface effects on transient three-dimensional flows around rotating spheres at moderate Reynolds numbers. *Computers and Fluids* **32**, 1405–1433.

NISHINO, T., ROBERTS, G. T. & ZHANG, X. 2007 Vortex shedding from a circular cylinder near a moving ground. *Physics of Fluids* **19**, 025103–1–025103–12.

NOACK, B. R. & ECKELMANN, H. 1994 A low-dimensional Galerkin method for the three-dimensional flow around a circular cylinder. *Physics of Fluids* **6** (1), 124–143.

NOACK, B. R., KÖNIG, M. & ECKELMANN, H. 1993 Three-dimensional stability analysis of the periodic flow around a circular cylinder. *Physics of Fluids A* **5** (6), 1279–1281.

OESTERLÉ, B. & DINH, T. B. 1998 Experiments on the lift of a spinning sphere in a range of intermediate Reynolds numbers. *Experiments in Fluids* **25**, 16–22.

ORMIÈRES, D. & PROVANSAL, M. 1999 Transition to turbulence in the wake of a sphere. *Physical Review Letters* **83** (1), 80–83.

PRANDTL, L. 1926 Application of the magnus effect to the wind propulsion of ships. *Tech. Rep.* 367. National Advisory Committee for Aeronautics.

PRANDTL, L. & TIETJENS, O. G. 1934 *Applied Hydro- and Aeromechanics*, 1st edn. McGraw-Hill.

PRICE, S. J., SUMNER, D., SMITH, J. G., LEONG, K. & PAÏDOUSSIS, M. P. 2002 Flow visualisation around a circular cylinder near to a plane wall. *Journal of Fluids and Structures* **16** (2), 175–191.

PROKUNIN, A. N. 2004 Microcavitation in the slow motion of a solid spherical particle along a wall in a fluid. *Fluid Dynamics* **39** (5), 771–778.

PROKUNIN, A. N. 2007 The effects of atmospheric pressure, air concentration in the fluid, and the surface roughness on the solid-sphere motion along a wall. *Physics of Fluids* **19**, 113601–1–113601–10.

PROVANSAL, M., MATHIS, C. & BOYER, L. 1987 Benard-von Kármán instability: Transient and forced regimes. *Journal of Fluid Mechanics* **182**, 1–22.

PROVANSAL, M., SCHOUVEILER, L. & LEWEKE, T. 2004 From the double vortex street behind a cylinder to the wake of a sphere. *European Journal of Mechanics B/Fluids* **23**, 65–80.

PRUPPACHER, H. R., LE CLAIR, B. P. & HAMIELEC, A. E. 1970 Some relations between drag and flow pattern of viscous flow past a sphere and a cylinder at low and intermediate Reynolds numbers. *Journal of Fluid Mechanics* **4**, 781–790.

Reichl, P., Hourigan, K. & Thompson, M. C. 2005 Flow past a cylinder close to a free surface. *Journal of Fluid Mechanics* **533**, 269–296.

Robichaux, J., Balachandar, S. & Vanka, S. P. 1999 Three-dimensional Floquet instability of the wake of square cylinder. *Physics of Fluids* **11** (3), 560–578.

Roshko, A. 1954 On the development of turbulent wakes from vortex streets. *Tech. Rep.* 1191. National Advisory Committee for Aeronautics.

Rubinow, S. I. & Keller, J. B. 1961 The transverse force on a spinning sphere moving in a viscous fluid. *Journal of Fluid Mechanics* **11**, 447–459.

Ryan, K., Thompson, M. C. & Hourigan, K. 2005 Three-dimensional transition in the wake of bluff elongated cylinders. *Journal of Fluid Mechanics* **538**, 1–29.

Sakamoto, H. & Haniu, H. 1990 A study on vortex shedding from spheres in a uniform flow. *Transactions of the ASME: Journal of Fluids Engineering* **112**, 386–392.

Sakamoto, H. & Haniu, H. 1995 The formation mechanism and shedding frequency of vortices from a sphere in uniform shear flow. *Journal of Fluid Mechanics* **287**, 151–171.

Salem, M. B. & Oesterle, B. 1998 A shear flow around a spinning sphere: Numerical study at moderate Reynolds numbers. *International Journal of Multiphase Flow* **24** (4), 563–585.

Saric, W. S. 1994 Görtler vortices. *Annual Review of Fluid Mechanics* **26**, 379–409.

Schouveiler, L. & Provansal, M. 2002 Self-sustained oscillations in the wake of a sphere. *Physics of Fluids* **14** (11), 3846–3854.

Seddon, J. R. T. & Mullin, T. 2006 Reverse rotation of a cylinder near a wall. *Physics of Fluids* **18**, 041703–1–4.

Seddon, J. R. T. & Mullin, T. 2008 Cavitation in anisotropic fluids. *Physics of Fluids* **20** (2), 023102–1–023102–5.

Sengupta, T. K., De, S. & Sarkar, S. 2003 Vortex-induced instability of an incompressible wall-bounded shear layer. *Journal of Fluid Mechanics* **493**, 277–286.

Sheard, G. J., Thompson, M. C. & Hourigan, K. 2003a A coupled Landau model describing the Strouhal-Reynolds number profile of a three-dimensional circular cylinder wake. *Physics of Fluids* **15** (9), L68–L71.

Sheard, G. J., Thompson, M. C. & Hourigan, K. 2003b From spheres to circular cylinders: The stability and flow structures of bluff ring wakes. *Journal of Fluid Mechanics* **492**, 147–180.

Sheard, G. J., Thompson, M. C., Hourigan, K. & Leweke, T. 2005 The evolution of a subharmonic mode in a vortex street. *Journal of Fluid Mechanics* **534**, 23–38.

Stokes, G. G. 1851 On the effect of the internal friction of fluids on the motion of pendulums. *Transactions of the Cambridge Philosophical Society* **9**, 8–106.

Takemura, F. & Magnaudet, J. 2003 The transverse force on clean and contaminated bubbles rising near a vertical wall at moderate Reynolds number. *Journal of Fluid Mechanics* **495**, 235–253.

Tamaki, H. & Keller, H. B. 1969 Steady two-dimensional viscous flowof an incompressible fluid past a circular cylinder. *Physics of Fluids Supplement II* **12** (12), II–51–II–56.

Taneda, S. 1956a Experimental investigation of the wake behind a sphere at low Reynolds numbers. *Physical Society of Japan* **11** (10), 1104–1108.

Taneda, S. 1956b Experimental investigation of the wakes behind cylinders and plates at low Reynolds numbers. *Physical Society of Japan* **11** (3), 302–307.

Taneda, S. 1965 Experimental investigation of vortex streets. *Journal of the Physical Society of Japan* **20** (9), 1714–1721.

Tang, T. & Ingham, D. B. 1991 On steady flow past a rotating circular cylinder at Reynolds numbers 60 and 100. *Computers and Fluids* **19** (2), 217–230.

Thom, A. 1933 The flow past circular cylinders at low speeds. *Proceedings of the Royal Society of London A* **141** (845), 651–669.

Thompson, M., Hourigan, K. & Sheridan, J. 1996 Three-dimensional instabilities in the wake of a circular cylinder. *Experimental Thermal and Fluid Science* **12**, 190–196.

Thompson, M. C., Hourigan, K., Cheung, A. & Leweke, T. 2006 Hydrodynamics of a particle impact on a wall. *Applied Mathematical Modelling* **30**, 1356–1369.

Thompson, M. C., Leweke, T. & Provansal, M. 2001a Kinematics and dynamics of sphere wake transition. *Journal of Fluids and Structures* **15**, 575–585.

Thompson, M. C., Leweke, T. & Williamson, C. H. 2001b The physical mechanism of transition in bluff body wakes. *Journal of Fluids and Structures* **15**, 607–616.

Tomboulides, A. G. & Orszag, S. A. 2000 Numerical investigation of transitional and weak turbulent flow past a sphere. *Journal of Fluid Mechanics* **416**, 45–73.

Van Atta, C. W. 1997 Comments on "Hopf bifurcation in wakes behind a rotating and translating circular cylinder". *Physics of Fluids* **9** (10), 3105–3106.

Van Dyke, M. 1982 *An Album of Fluid Motion*. Parabolic Press.

Vasseur, P. & Cox, R. G. 1977 The lateral migration of spherical particles sedimenting in a stagnant bounded fluid. *Journal of Fluid Mechanics* **80**, 561–591.

White, F. M. 1999 *Fluid Mechanics*, 4th edn. McGraw-Hill.

Williams, P. T. & Baker, A. J. 1997 Numerical simulations of laminar flow over a 3D backward-facing step. *International Journal for Numerical Methods in Fluids* **24**, 1159–1183.

Williamson, C. 1996a Three-dimensional wake transition. *Journal of Fluid Mechanics* **328**, 345–407.

Williamson, C. H. K. 1988a The existance of two stages in the transition to three-dimensionality of a cylinder wake. *Physics of Fluids* **31** (11), 3165–3168.

Williamson, C. H. K. 1988b The existence of two stages in the transition to three-dimensionality of a cylinder wake. *Physics of Fluids* **31** (11), 3165–3168.

Williamson, C. H. K. 1989 Oblique and parallel modes of vortex shedding in the wake of a circular cylinder at low Reynolds numbers. *Journal of Fluid Mechanics* **206**, 579–627.

Williamson, C. H. K. 1996b Vortex dynamics in the cylinder wake. *Annual Review of Fluid Mechanics* **28**, 477–539.

Williamson, C. H. K. 2004 Vortex-induced vibrations. *Annual Review of Fluid Mechanics* **36**, 413–455.

Williamson, C. H. K. & Roshko, A. 1988 Vortex formation in the wake of an oscillating cylinder. *Journal of Fluids and Structures* **2** (4), 355–381.

Zdravkovich, M. M. 1985a Forces on a circular cylinder near a plane wall. *Applied Ocean Research* **7** (4), 197–201.

Zdravkovich, M. M. 1985b Observation of vortex shedding behind a towed circular cylinder near a wall. In *Flow Visualization III- Proceedings of the 3rd International Symposium on Flow Visualization* (ed. W. J. Yang), pp. 423–427. Hemisphere.

Zeng, L., Balachandar, S. & Fischer, P. 2005 Wall-induced forces on a rigid sphere at finite Reynolds number. *Journal of Fluid Mechanics* **536**, 1–25.

Zhang, H., Fey, U., Noack, B. R., Koenig, M. & Eckelmann, H. 1995 On the transition of the cylinder wake. *Physics of Fluids* **7** (4), 779–794.